

ELASTIC ROCK PROPERTIES OF TIGHT GAS SANDSTONES
FOR RESERVOIR CHARACTERIZATION
AT RULISON FIELD, COLORADO

by
Eugenia Rojas

ABSTRACT

This thesis research integrates multicomponent seismic and well log data analysis with lab-based rock physics for elastic rock properties sensitivity to pressure, fluid, and lithology changes on tight gas sandstones. The rock physics of tight gas sandstones (low permeability and low porosity) has been relatively neglected. Today tight gas is a vast resource, especially in the Rockies, and new production technologies are being developed to exploit this natural resource. The Williams Fork Formation in Rulison Field is thick and contains up to 135 Bcf gas per section, but sands are lenticular and discontinuous, so the drainage area is limited. Technology improvements are needed to successfully produce low permeability gas reservoirs. My study links rock physics to well log and seismic data for prediction of better areas to develop, based on integrated reservoir characterization.

Several researchers have reported methods for prediction of overpressured zones from elastic measurements in high porosity sandstone reservoirs. However, very little work has been done in tight gas sandstones. In this work, rock physics measurements on tight gas sandstone cores are conducted. I also have analyzed cross-dipole sonic log data to understand the relations between elastic properties (V_p/V_s , P- and S-impedance) and petrophysical properties (porosity and lithology). Finally, I quantify V_p/V_s variations due to changes in reservoir properties of tight gas sandstones with the potential to apply this

information to interpret V_p/V_s extracted from AVO analysis or multicomponent reflection data.

The results of my analysis show that lithology has a significant influence on V_p/V_s . Fluid effects on V_p/V_s are significant but less than lithology effects. V_p/V_s changes due to primary depletion (pore pressure decreases) are difficult to observe in unfractured tight gas sandstones. However, V_p/V_s is very sensitive to pore pressure increases and could be used as an overpressure indicator.

Tight gas sandstones will typically have a V_p/V_s lower than 1.7, while shales will have V_p/V_s higher than 1.7. Thus, we expect a decrease in V_p/V_s from shales to reservoir sandstones. Typically, the presence of gas-saturated sandstones lowers the V_p/V_s even further (V_p/V_s of 1.6 or lower) and overpressure conditions can lower V_p/V_s even more (<1.5). These results can be used to interpret seismic data in tight gas sandstones.

TABLE OF CONTENTS

ABSTRACT.....	iii
LIST OF FIGURES	ix
LIST OF TABLES.....	xv
ACKNOWLEDGMENTS	xvi
Chapter 1 INTRODUCTION.....	1
1.1 Objective.....	3
1.2 Motivation and context of research.....	4
1.3 Field description.....	7
1.3.1 Geological setting	7
1.3.2 Rock, reservoir and fluid properties.....	9
1.3.3 Production history	13
1.3.4 4D 9C-seismic data and cross-dipole sonic logs.....	15
1.3.5 U.S. DOE’s multiwell experiment site description.....	17
1.4 Method and approach.....	19
Chapter 2 LABORATORY EXPERIMENTS ON CORE SAMPLES.....	22
2.1 Introduction.....	22
2.2 Sample selection and preparation	23
2.3 Sample characterization	26
2.3.1 Petrophysical description.....	27

2.3.1.1	Permeability measurements	27
2.3.1.2	Porosity measurements	32
2.3.2	Mineralogical description	43
2.3.3	Scanning electron microscopy (SEM)	44
2.4	Ultrasonic velocity measurements	49
2.4.1	Anisotropy test at room-conditions.....	49
2.4.2	Ultrasonic P- and S-wave velocity measurements at varying confining pressure.....	52
2.4.2.1	Experimental setup.....	52
2.4.2.2	Ultrasonic velocity and error calculations	55
2.4.2.3	Dry rock ultrasonic measurements.....	57
2.4.3	Discussion of results	67
2.4.4	Assumption of experimental work.....	68
Chapter 3	ISOTROPIC NUMERICAL MODELING OF ELASTIC ROCK PROPERTIES	69
3.1	Introduction.....	69
3.2	Gassmann's fluid substitution.....	69
3.2.1	Input variables for Gassmann's equation.....	72
3.2.1.1	Mineral modulus, K_M and μ_M	73
3.2.1.2	Fluid modulus, K_f	74
3.2.1.3	Dry modulus, K_{DRY}	82

3.2.1.4 Porosity, ϕ	83
3.2.2 Results of Gassmann’s fluid substitution.....	83
3.3 Discussion of results	94
3.3.1 Overpressure and fluid effects on velocities.....	94
3.3.2 Assumptions of experimental and modeling study	97
Chapter 4 RELATIONS BETWEEN ELASTIC AND PETROPHYSICAL PROPERTIES FROM CROSS-DIPOLE SONIC LOGS.....	98
4.1 Introduction.....	98
4.2 Quality control of the data	99
4.3 Relations between porosity, lithology, fluids, and elastic properties obtained from cross-dipole sonic logs	101
4.3.1 Elastic properties and fluid-lithology discrimination	104
4.3.2 Elastic properties and porosity.....	106
4.3.3 Elastic properties and fluid saturation.....	107
4.4 Discussion of results	109
4.4.1 Lithology and fluid effects on velocities	109
4.4.2 Quantifying V_p/V_s variations	110
4.4.3 Assumptions of log analysis	110
Chapter 5 ELASTIC ROCK PROPERTIES FROM SEISMIC DATA AND APPLICATIONS	111
5.1 Introduction.....	111

5.2 Multicomponent seismic interpretation	112
5.2.1 Well ties to seismic	115
5.2.2 Interval V_p/V_s estimation from multicomponent travel time data ..	117
5.3 Applications of rock physics to multicomponent seismic data.....	121
5.4 Discussion of results	131
Chapter 6 CONCLUSIONS AND RECOMMENDATIONS FOR FUTURE RESEARCH.....	133
6.1 Conclusions.....	133
6.2 Recommendations for future research	135
REFERENCES	140

LIST OF FIGURES

Figure 1-1 Map of Piceance Basin showing location of gas fields producing from Williams Fork basin-centered gas reservoirs. Structure contours (ft) on top of Rollins Sandstone. Adapted from Williams Company.....	9
Figure 1-2 Generalized Mesaverde section, Piceance Basin. Courtesy of Williams Company.....	10
Figure 1-3 Cross section of Williams Fork Formation, Piceance Basin.....	11
Figure 1-4 Comparison of gas composition based on carbon dioxide and ethane contents of gas samples desorbed from Cameo coal cutting and produced from Cameo coalbeds and from sandstones above the Cameo.....	14
Figure 1-5 Pore pressure gradient measurements as function of depth at the U.S. DOE's MWX-site	15
Figure 1-6 Location of RCP's 4D 9C survey area, DOE's P-wave survey (green line), U.S. Multiwell experiment site, two cross-dipole sonic logs, FMI's location.....	16
Figure 2-1 The Mesaverde Formation at MWX Site	25
Figure 2-2 Diagram of permeability measurement on a core sample.....	27
Figure 2-3 Klinkenberg "b" factor as a function of Klinkenberg-corrected permeability using two empirical correlations, Penn State correlation (1950) and Tight Gas Sand correlation (1979).....	31
Figure 2-4 Klinkenberg-corrected permeability as a function of nitrogen permeability ...	32
Figure 2-5 Klinkenberg corrected permeability versus fractional porosity	36
Figure 2-6 Measured plug porosity as a function of grain density	38
Figure 2-7 Measured plug permeability as a function of grain density	39
Figure 2-8 Measured plug permeability as a function of plug porosity measurements.....	40

Figure 2-9 Porosity-permeability relationships for vertical and horizontal plugs	41
Figure 2-10 Measured plug permeability anisotropy (k_v/k_h) versus depth.....	42
Figure 2-11 Scanning Electron Microscope diagram (Museum of Science, Boston).....	45
Figure 2-12 Thin section of a reservoir tight gas sandstone sample (R-6451.5V)	46
Figure 2-13 Thin section of a reservoir tight gas shaley sandstone sample (R-5566.2H) .	47
Figure 2-14 SEM pictures of sample R-6451.5 at different magnification (50x, 100x, 500x, 1000x)	48
Figure 2-15 Anisotropy test setup at room-conditions. S-wave transducers (St_1 and St_2), are perpendicular to each other while rotating the sample	49
Figure 2-16 Schematic showing azimuthal dependence of shear wave propagation in a core sample. Adapted from Sondergeld and Rai (1986).....	50
Figure 2-17. Compressional and shear (fast and slow) wave propagation through sample R-6451.5H.....	51
Figure 2-18 Schematic diagram of the pulse transmission technique for a core sample for varying confining and pore pressure (Batzle and Prasad, 2004) at the Center for Rock Abuse at the Colorado School of Mines	52
Figure 2-19 Picture of equipment for ultrasonic measurements under confining and pore pressure at the Center for Rock Abuse at the Colorado School of Mines	53
Figure 2-20 Sample setup for ultrasonic measurements	54
Figure 2-21 P-wave signal through sample R-5719V at different confining pressures.....	58
Figure 2-22 S-wave signal through sample R-5719V at different confining pressures.....	59
Figure 2-23 Effect of differential pressure on elastic properties of sample R-5719V ($\phi=10\%$ and $k=0.042$ mD)	62
Figure 2-24 Effect of differential pressure on elastic properties and elastic ratios on sample R-5719V	63

Figure 2-25 Crossplot of elastic properties of sample R-5719V at increasing (up) and decreasing (down) pressures	64
Figure 2-26 Effect of differential pressure on elastic properties of sample R-5727.1V ($\phi=7.74\%$, $k=0.006\text{mD}$)	65
Figure 2-27 Effect of differential pressure on elastic properties and elastic ratios on sample R-5727.1V	66
Figure 2-28 Crossplot of elastic properties of sample R-5727.1V at increasing (up) differential pressures	67
Figure 3-1 Bulk modulus of brine as a function of pore pressure, at reservoir temperature (80°C) and salinity (25,000 ppm NaCl) [FLAG 4]	77
Figure 3-2 Density of brine as a function of pore pressure, at reservoir temperature (80°C) and salinity (25,000 ppm NaCl) [FLAG 4]	78
Figure 3-3 Bulk modulus of Rulison gas (85% methane, 10% nitrogen, and 5% ethane) and 100% methane as a function of pore pressure at reservoir temperature (80°C) [FLAG 4]	79
Figure 3-4 Density of Rulison gas (85% methane, 10% nitrogen, and 5% ethane) and 100% methane as a function of pore pressure at reservoir temperature (80°C) [FLAG 4]	79
Figure 3-5 Bulk modulus of reservoir fluids as a function of pore pressure and saturations ($T=80^{\circ}\text{C}$)	81
Figure 3-6 Density of reservoir fluids as a function of pore pressure and saturations ($T=80^{\circ}\text{C}$)	82
Figure 3-7 P-wave velocity versus confining pressure after Gassmann's fluid substitution at constant pore pressure ($P_p=3000$ psi) on sample R-5719V using different mineral bulk modulus	83
Figure 3-8 P-wave velocity versus confining pressure after Gassmann's fluid substitution at a constant pore pressure ($P_p=3000$ psi) on sample R-5719V using different fluids	84

Figure 3-9 S-wave velocity versus confining pressure after Gassmann's fluid substitution at a constant pore pressure ($P_p=3000$ psi) on sample R-5719V using different fluids	85
Figure 3-10 P-wave velocity changes with pore pressure and pore fluid (brine and Rulison gas) at a constant confining pressure for sample R-5719V after Gassmann's fluid substitution	86
Figure 3-11 P-wave velocity changes with differential pressure and pore fluid (brine and Rulison gas) at a constant confining pressure for sample R-5719V after Gassmann's fluid substitution	88
Figure 3-12 P-wave velocity changes with differential pressure and different pore fluid saturation at a constant confining pressure for sample R-5719V after Gassmann's fluid substitution	89
Figure 3-13 S-wave velocity changes with differential pressure and pore fluid (brine and Rulison gas) at a constant confining pressure for sample R-5719V after Gassmann's fluid substitution	90
Figure 3-14 S-wave velocity changes with pore pressure and pore fluid (brine and Rulison gas) at a constant confining pressure for sample R-5719V after Gassmann's fluid substitution	90
Figure 3-15 S-wave velocity changes with differential pressure and different pore fluid saturation at a constant confining pressure for sample R-5719V after Gassmann's fluid substitution	91
Figure 3-16 V_p/V_s versus differential pressure for a saturated sample (brine and gas) calculated with Gassmann's equation. Also dry measurements are plotted	92
Figure 3-17 V_p/V_s changes with pore pressure and pore fluid (brine and Rulison gas) at a constant confining pressure for sample R-5719V after Gassmann's fluid substitution.....	93
Figure 3-18 V_p/V_s changes with differential pressure and different pore fluid saturation at a constant confining pressure for sample R-5719V after Gassmann's fluid substitution.....	93
Figure 3-19 V_p/V_s versus differential pressure in a dry tight sandstone ($\phi=10\%$ and $k=42$ μD , depth=5719 ft)	95

Figure 3-20 V_p/V_s versus differential pressure for a saturated sample (tight gas sandstone, $\phi=10\%$, $k=42\ \mu\text{D}$, depth= 5719 ft). Fluid substitution using Gassmann's equation was done for 100% water saturation (salinity 25000 ppm), butane, methane and a mixture of gases (85% methane, 10% nitrogen and 5 % ethane.) which represents Rulison Field gas.....	96
Figure 4-1 V_p/V_s calculated from P-wave slowness, S_1 slowness and S_2 slowness data from cross-dipole sonic log in well RWF 332-21.....	102
Figure 4-2 P-impedance, V_p/V_{s1} , V_p/V_{s2} and shear anisotropy magnitude calculated using the cross-dipole sonic acquired in RWF 332-21.....	103
Figure 4-3 Anisotropy vs. gamma ray plot showing higher anisotropy values in sands .	103
Figure 4-4 V_p/V_s versus P-wave impedance calculated from two dipole sonic logs (RWF 332-21 and RWF 542-20) in Rulison Field tight sands and shales.....	105
Figure 4-5 V_p/V_s versus S-wave impedance calculated from two dipole sonic logs (RWF 332-21 and RWF 542-20) in Rulison Field tight sands and shales.....	105
Figure 4-6 Crossplot of P-wave velocity versus density porosity of Williams Fork Formation (4500-6500 ft) colored by gamma ray measurements.....	106
Figure 4-7 Crossplot of S-wave velocity versus density porosity of Williams Fork Formation (4500-6500 ft) colored by gamma ray measurements.....	106
Figure 4-8 V_p/V_s versus porosity colored by gamma ray measurements	107
Figure 4-9 V_p/V_s versus P-wave impedance colored by estimated S_w	108
Figure 5-1 P-wave data tie to well control.....	116
Figure 5-2 PS-wave data tie to well control.....	117
Figure 5-3 Migrated sections from RCP 2003 multicomponet survey (Inline 48).....	118
Figure 5-4 Interval V_p/V_s map from the top of UMV shale to the top of Cameo coal, computed using P- and PS-wave data.....	120
Figure 5-5 RCP survey area represented by the external polygon and sub-area of the survey used for the seismic inversion is represented by the smaller polygon	124

Figure 5-6 Seismic line A (x-line 72) from Rulison Field showing the P-impedance inversion from post-stack data in P-time	125
Figure 5-7 Seismic line B (in-line 85) from Rulison Field showing the P-impedance inversion from post-stack data in P-time	126
Figure 5-8 Histogram of P-impedance numerical values in the thick heterogeneous reservoir area.....	127
Figure 5-9 Crossplot of P-wave velocity versus P-impedance from log data colored by gamma ray measurements.....	128
Figure 5-10 P-impedance extracted at 1000 ms in P-time and the corresponding P-wave velocity calculated using Equation 5-3	129
Figure 5-11 Crossplot of S-wave velocity versus S-impedance from log data colored by gamma ray measurements.....	130
Figure 6-1 Possible future integrated workflow for dynamic-anisotropic reservoir characterization of fractured tight gas sandstones at Rulison Field.....	139

LIST OF TABLES

Table 2-1 Depositional environment and depth intervals of core samples chosen at MWX-1 well.....	24
Table 2-2 Sample ID, depth and lithology for each core sample.....	26
Table 2-3 Measured plug porosity, Klinkenberg corrected nitrogen permeability, and grain density for samples used in this study	37
Table 2-4 Whole rock mineralogy from results of XRD measurements (weight percentage).....	43
Table 2-5 Relative abundance (percentage) of phyllosilicate mineralogy from XRD measurements.....	44
Table 2-6 Results of XRD measurements.....	44
Table 2-7 Description of Williams Fork Formation samples	62
Table 3-1 Effective K_M and μ_M using Hill-Voight-Reuss average and mineralogical composition of sample R-5719V	75
Table 3-2 Effective K_M and μ_M using Hill-Voight-Reuss average, mineralogical composition of sample R-5719V, and using averaged elastic modulus for clays	75
Table 3-3 Effective K_M and μ_M assuming sample R-5719V is 100% Quartz.....	75
Table 3-4 Results of compositional and isotopic analysis of gases at Rulison Field, MWX-1 well.....	76

ACKNOWLEDGEMENTS

This research was sponsored by the Reservoir Characterization Project (RCP) with collaboration of the Center for Rock Abuse and the Center for Petrophysics (CENPET) at the Colorado School of Mines. I am grateful for their support and for the opportunity of learning from each of these groups. I thank Dr. Tom Davis for his support, guidance and challenging discussions. A special thanks goes to Dr. Mike Batzle and Dr. Manika Prasad, who guided me in the laboratory and taught me about rock physics and experimental work. I appreciate the guidance and challenging discussions with Reinaldo Michelena (iReservoir.com, Inc.), who taught me about the practical aspects of seismic inversion and multicomponent interpretation, and encouraged me to publish my work.

I would also like to acknowledge Dr. Jennifer Miskimins and Dr. Ramona Graves for teaching me important aspects of Petroleum Engineering. Special thanks goes to Ronny Hofmann and Ludmila Adam for their help and guidance during the experimental work, and also to Matt Silbernagel for helping me to collect ultrasonic data. I feel privileged to have worked and interacted with many fellow students, including Gaby Briceño, Xiaoxia Xu, Jyoti Behura, Shannon Higgins, Cristian Malaver, Kjetil Jansen, and Lauri Burke. Their stimulating conversations and help in learning are appreciated. I would also like to acknowledge Steve Cumella, Doug Ostby and Lesley Evans from Williams Oil Company for providing important data and information necessary for this research, and for helping me to understand many aspects of Rulison Field.

Chapter 1

INTRODUCTION

This research is sponsored by the Reservoir Characterization Project (RCP) with collaboration of the Rock Physics Lab and the Center for Petrophysics, all of them industry-sponsored research consortia at the Colorado School of Mines. The main goal of RCP is to incorporate high-resolution multicomponent seismic data into dynamic reservoir characterization. Phase X involves the time-lapse and multicomponent seismic analysis of Rulison Field, Piceance Basin, Colorado.

Rulison Field is located in the Piceance Basin, Colorado. Gas production is primarily from the non-marine Late Cretaceous Williams Fork Formation. Gas is trapped in a 1700-2400 ft interval of stacked, very low permeability, highly discontinuous fluvial sandstones, where the lower two-thirds of the Williams Fork is continuously gas-saturated down dip of water-bearing sandstones (Cumella and Ostby, 2003). A thin shale interval in the upper part of the Williams Fork is a strong seismic reflector and is possibly acting as a seal that influences the overpressuring of this basin-centered gas accumulation.

Many geological production challenges are present in this field: very low permeability (1-60 μ D) and low porosity (1-10%) sandstones, presence of natural fractures, overpressured areas, uncertainty in gas/water contact and very high

heterogeneity. Seismic interpretation is complicated due to the lateral changes in Williams Fork stratigraphy.

The proposed study area includes a 10-acre spacing pilot. Even with this well density, observed connectivity between individual channel sandstones rarely occurs. Conventional P-wave seismic data is not able to locate the channels. The subtle fracture networks that control gas production and typically correspond to good well performance are also un-resolvable with conventional P-wave volumes.

An aggressive drilling campaign by the Williams Production Company, the field operator, is underway in this area. RCP acquired high-resolution 4D multicomponent seismic data to improve reservoir imaging, to obtain reservoir properties as V_p/V_s and Poisson's ratios, to understand subtle-fracture networks through anisotropy, and to conduct subsequent seismic monitoring at timely intervals coordinated with the drilling. The benefit of high-resolution reservoir characterization is to help determine the drainage area and depletion zones in these densely drilled patterns. Understanding the dynamics of the reservoir will be critical to planning future development wells to optimize production while lessening economic and environmental risk.

Rock physics theory is the link between the seismic data and the reservoir processes. The purpose of this work is to understand and qualitatively compare V_p/V_s estimations using different data sets to reduce uncertainty in pore pressure and fluid-lithology prediction in tight gas sands reservoirs. First, laboratory experiments (permeability, porosity and ultrasonic measurements) are conducted to model velocity

changes under differential pressure. Second, cross-dipole sonic log data are analyzed and rock elastic properties are calculated (V_p/V_s , P- and S-impedance) with the purpose of developing rock physics based charts that can reduce uncertainty during the interpretation of elastic rock properties obtained from multicomponent seismic data. Third, elastic rock properties (P- and S-wave impedance, V_p/V_s) are obtained from seismic data using a post-stack amplitude inversion method (model based inversion, Hampson-Russell Software Services, Ltd.). Rock physics trends obtained from laboratory measurements and log data can be used to interpret multicomponent seismic in terms of pore pressure, pore fluid and lithology.

1.1 Objective

Seismic data are now being used to obtain rock properties and to identify pore fluids. With high-resolution multicomponent seismic, direct measurement of P- and S-wave reduce ambiguity when predicting pore fluids, lithology and overpressure areas. Understanding velocity changes detected in seismic data requires a thorough understanding of relationships between elastic properties (e.g., V_p/V_s , P- and S-impedance) and rock and fluid properties.

The purpose of this thesis is to understand V_p/V_s sensitivity to pore pressure changes, lithology and fluid content, and the implications of those relationships on seismic interpretation. This research has an immediate application in Rulison Field for

identification of “sweet spots”. Active drilling is in progress at Rulison Field; therefore, ideas and concepts can be directly tested.

1.2 Motivation and context of research

In the United States, natural gas found in tight gas sands and shales has become a significant source of energy supply. This source of gas has been increasing in importance thanks to new technologies and higher gas prices. The U.S. Geological Survey estimates tight-gas sands and shales may contain up to 460 trillion cubic feet (Tcf) of gas in the U.S., almost three times the amount of currently proved gas reserves. Tight gas sands now account for about 19% of U.S. natural gas production, but the U.S. Energy Information Administration estimates that tight-gas sands could account for up to 35% of the country’s recoverable gas resources.

Unconventional gas plays, represent large volumes of resources that are difficult to produce. Technology improvements are needed to better understand tight gas resource characteristics and develop solid engineering and geosciences approaches for significant production increases from this low permeability resource. For these reasons, it is very important to improve seismic reservoir characterization in tight gas sandstones. More contemporary basin-center gas models invoke a “sweet spot” concept to highlight the need to identify areas of improved reservoir quality to increase the probability of economically successful results. More recent studies of basin-center gas plays reveal that the primary trap controls are better described as conventional, although subtle,

stratigraphic, structural and capillary traps (Camp et al., 2003). This study focus on the development of rock physics trends that are applied for “sweet spot” identification from seismic data.

The rock physics of tight gas sandstones has been relatively neglected. In low permeability and porosity sandstones, many grain-contact rock physics models are not valid, mainly due to the presence of cracks in the rocks. Fluids effects are not apparent, so fluid monitoring from seismic is very difficult. There are a number of geologically dependent problems related to the complex depositional systems that cause high heterogeneity in the reservoir.

Obtaining information about rock properties (porosity, fluid content, lithology, and perhaps even permeability) from seismic data would greatly aid the effort to identify and produce gas reservoirs. The present research is specifically aimed at measuring and understanding V_p/V_s in tight gas sandstones reservoir relevant for hydrocarbon production.

Through the analysis of multicomponent seismic data, important rock properties such as V_p/V_s or Poisson's ratio can be extracted. This elastic parameter can improve predictions about porosity, reservoir fluid type and lithology (Pickett, 1963; Tatham, 1982; Miller and Stewart, 1990). Compressional seismic velocity alone is not a good lithology indicator because of the overlap in V_p for various rock types. The additional information provided by V_s can reduce uncertainty involved in interpretation.

Using core measurements, Pickett (1963) demonstrated the potential of V_p/V_s as a lithology indicator. Subsequent research has generally confirmed these values and has also indicated that V_p/V_s in mixed lithologies varies linearly between the V_p/V_s values of the end members (Eastwood and Castagna, 1983; Rafavich et al., 1984; Castagna et al., 1985). V_p/V_s is sensitive to gas in most clastic reservoirs and will often show a marked decrease due to its presence (Kithas, 1976; Gregory, 1977; Tatham, 1982; Eastwood and Castagna, 1983; Ensley, 1984; McCormack et al., 1985).

Seismic velocities are affected by many factors including porosity, pore geometry, pore-fluid, effective stress, depth of burial, degree and orientation of fracturing (McCormack et al., 1985). In order to understand how rock properties influence velocity in a specific geological environment, it is important to integrate observations from a variety of approaches such as core analysis, seismic and well log interpretation, and numerical modeling. This thesis research provides an unique opportunity to understand V_p/V_s estimated from core samples, well logs data and multicomponent seismic volumes and reduce the uncertainty in the lithology and pore fluid prediction in tight gas sandstones. S-wave information is obtained from: pure S-wave and PS-wave (converted wave) volumes acquired directly in the field.

Coupling P-wave and PS-wave or S-wave seismic analysis increases confidence in interpretation, provides additional measurements for imaging the subsurface and gives rock property estimates. Historically, it has been difficult to interpret P and PS seismic volumes consistently. These difficulties are related to the different event times and

frequencies on the PS data, together with differences in P-wave and PS-wave reflectivities. Due to the difference in frequency, velocity, wavelength and reflectivity, PS seismic sections may exhibit geologically significant changes in amplitude or character of events, which are not apparent on conventional P-wave sections. Improved images can be obtained with converted and pure shear wave data when the presence of gas originates poor seismic data areas in the P-wave sections. Therefore, it maybe helpful to have multicomponent seismic sections to work with in areas where the P-wave data quality is poor. Multicomponent seismic can help with imaging through gas clouds, and provide lithology and fluid identification.

1.3 Field description

A review of the geology, rock, reservoir and fluid properties, production history and data available for this study at Rulsion Field is presented in this section.

1.3.1 Geological setting

Rulison Field is a basin-centered gas accumulation located in the Piceance Basin, Colorado (Figure 1-1). Gas production is primarily from the non-marine Late Cretaceous Williams Fork Formation. Gas is trapped in a 1700-2400 ft interval of stacked, very low permeability, highly discontinuous fluvial sandstones, where the lower two-thirds of the Williams Fork is continuously gas-saturated down dip of water-bearing sandstones (Cumella and Ostby, 2003). A thin shale interval in the upper part of the Williams Fork

Formation is a strong seismic reflector and is possibly acting as a seal that influences the overpressuring of the basin-centered gas accumulation.

The Cretaceous Mesaverde Group is comprised of the Iles and Williams Fork Formations (Figure 1-2). The Iles Formation overlies the marine Mancos shale, and includes three regressive marine sandstones: the Corcoran, the Cozzette, and the Rollins member. These sandstones are laterally continuous and can be correlated across much of the southern and eastern Piceance Basin (Cumella and Ostby, 2003). The non-marine sandstones, shales and coals of the Williams Fork Formation were deposited on a broad coastal plain. The Cameo coal zone of the Williams Fork Formation overlies the Rollins and was deposited in paludal environments of the lower coastal plain. The sandstones that are present within the Cameo coal zone appear to have been deposited as point-bar deposits of meandering systems (Cumella and Ostby, 2003).

In the lower and middle part of the Williams Fork, the depositional style of the sandstones in this fluvial interval appears to have been meandering streams. There is a highly discontinuous nature of most of the sandstones in the producing interval. A strong seismic reflector is present in the upper part of the Mesaverde, this shale marker can be confidently correlated in much of the southern Piceance Basin (Cumella and Ostby, 2003). Wells spaced as close as 1100 ft (28 acres per well) show little to no pay correlation from well to well.

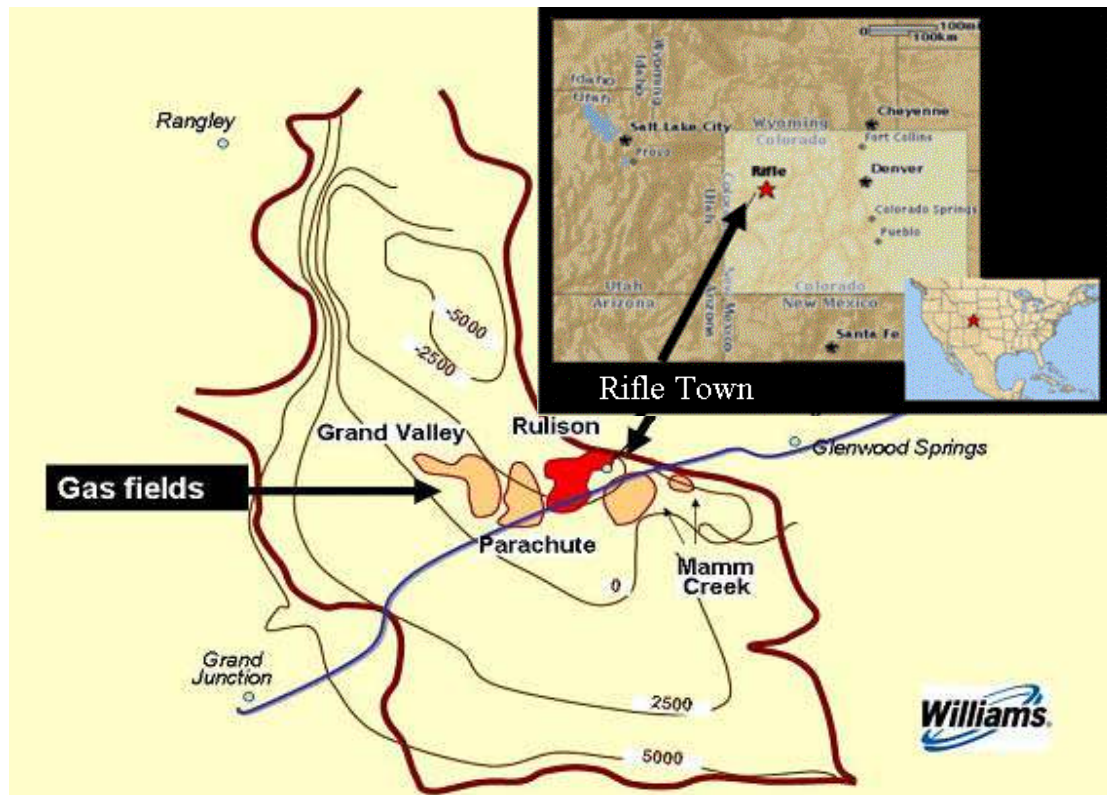


Figure 1-1 Map of Piceance Basin showing location of gas fields producing from Williams Fork basin-centered gas reservoirs. Structure contours (ft) on top of Rollins Sandstone. Adapted from Williams Company.

1.3.2 Rock, reservoir and fluid properties

Most of the understanding of the local reservoir matrix properties comes from research done during the U.S. DOE's Multiwell Experiment (MWX), a field laboratory aimed at improved characterization and gas production from low-permeability reservoirs.

Laboratory measurements of rock and reservoir properties were performed on numerous samples from approximately 4200 ft (1280 m) of Mesaverde core. Most of the properties (e.g., porosity and permeability) were measured at restored state, in-situ

conditions, and they are representative of the matrix-rock parameters (Lorenz et al., 1989). Some properties, such as permeability, are strongly controlled by natural fractures, therefore whole-reservoir permeabilities made during well tests vary significantly from the laboratory measurements.

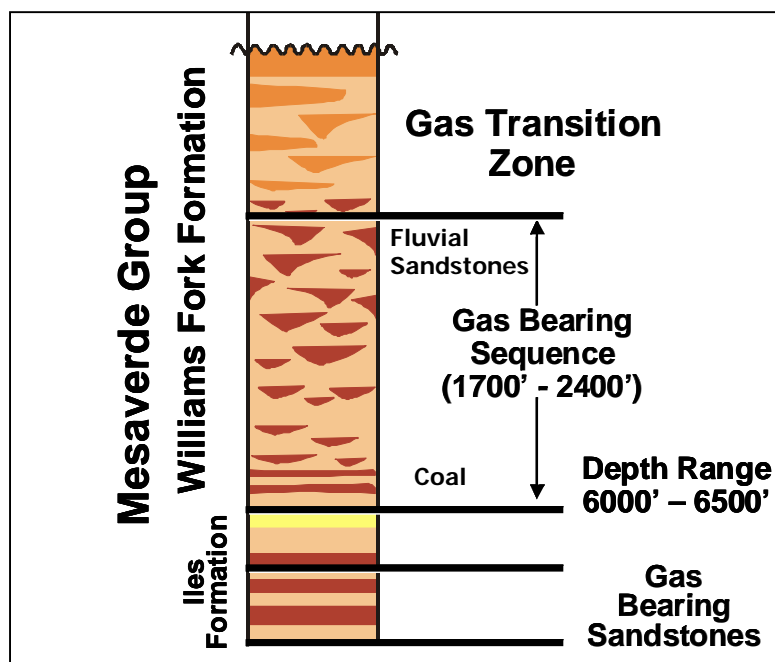


Figure 1-2 Generalized Mesaverde section, Piceance Basin. Courtesy of Williams Company.

Productive Williams Fork sandstone porosities range from 1-10%. Permeabilities (at dry conditions and 500 psi) range from 1-60 μD , and irreducible water saturations range from 40 to 65%. High irreducible water saturations are due in large part to the presence of authigenic clay that is common in most of the sandstones (Cumella and Ostby, 2003).

Porosities measured from density logs are about 10% to 12%, but measured porosities are lower as mentioned before. The upper one-third of the Williams Fork Formation is considered to have low reserve potential, due to high water saturation within the reservoir. Gas-water transition zones such as this are typical of low permeability basin-center gas accumulations (Figure 1-3).

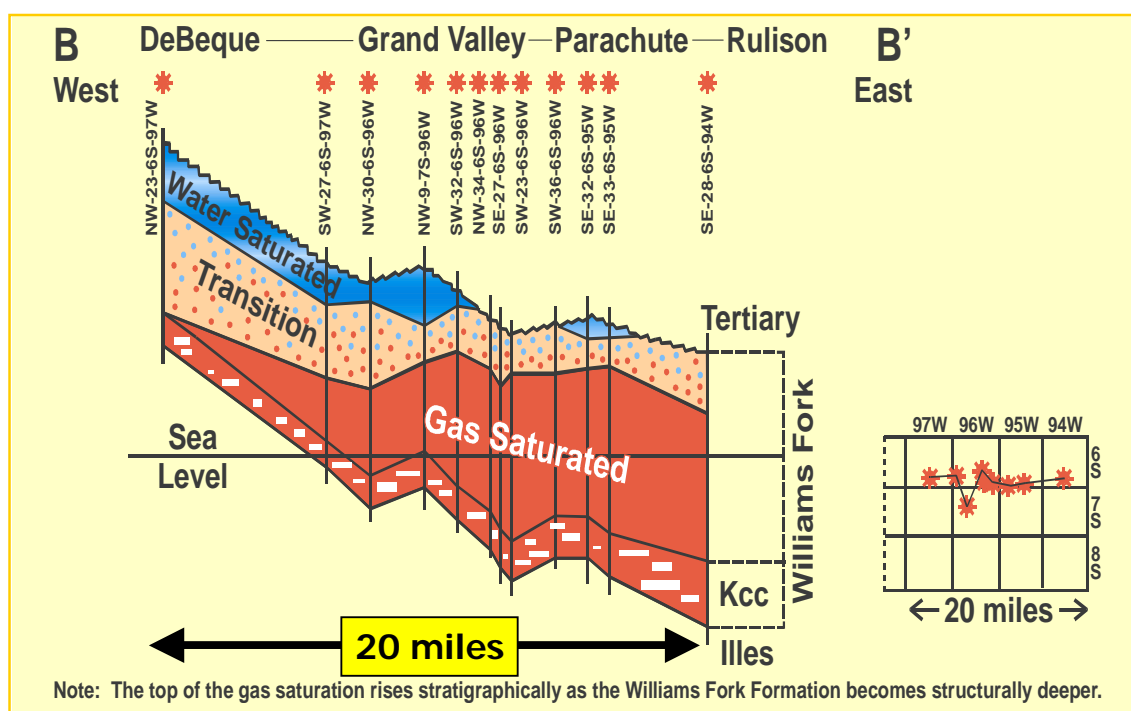


Figure 1-3 Cross section of Williams Fork Formation, Piceance Basin. Adapted from Reinecke et al. (1991).

Some authors (e.g., Shanley et al., 2004; Camp et al., 2003) recently have suggested the hypothesis of low permeability reservoirs not being part of a continuous-type gas accumulation or basin-center gas system in which productivity is dependent on the development of sweet spots associated with higher permeability due to natural

fractures. Instead, they suggest gas fields in this basin occur in low permeability, poor quality reservoir rocks in conventional traps. They suggest that low-permeability gas systems should be evaluated in a manner similar and consistent with conventional hydrocarbon systems. They argue that this kind of play reveals that the primary trap controls are better described as conventional although subtle, stratigraphic, structural and capillary traps (Camp et al., 2003).

Previous work has attempted to identify overpressure areas using resistivity and sonic logs. For example, at Jonah field, Green River Basin, Wyoming, the top of the overpressure (determined by continuous gas flaring during drilling) correlates within a few hundred feet to a drop in shale resistivity and increase in shale transit time. Coincidentally, the top of the anomalous velocity and resistivity profiles corresponds to the top of the overpressured gas in this field. Cluff and Cluff (2004), pointed out that regional examination of the logs demonstrates that the anomalies extend beyond the fields limits and persist at roughly the same stratigraphic position, clearly demonstrating that the anomaly is decoupled from present-day pressure conditions. They also suggested that Jonah Field represents a high remnant of the former regional top of overpressure instead of a leakage chimney from a deeper overpressured generation cell. They proposed that if this model is correct, exploration methods should focus on the seal conditions that prevent leakage instead of fracture models that promote leakage.

Tight gas sandstone reservoirs are very complex, and different geological scenarios could be possible. There is poor understanding in the petroleum system of these

unconventional plays. This research tends to help the understanding of petroleum systems associated with tight gas sandstones through the understanding of V_p/V_s anomalies in Rulison Field. In this thesis, the geological thinking of tight gas sandstone plays is open to different scenarios, where instead of consider valid or wrong previous geological models (e.g., basin-centered gas systems) a combination of different factors are considered possible (overpressured areas, natural fractures, different traps mechanisms, better quality rock).

The gas composition and generation in the Piceance Basin are important factors to understand to better characterize Rulison Field. Regarding the gas composition in Rulison Field, Reinecke et al. (1991), noted that gases from low-volatile bituminous coals in the Cameo zone and from sandstone reservoirs above the Cameo zone generally can be distinguished by their chemical composition. Coal gases are chemically drier (90% to 93% methane, 1% to 3% ethane, and 3% to 6% carbon dioxide) compared to gases from sandstones, which are chemically wetter (89% to 92% methane, 3% to 6% ethane, and 1% to 4% carbon dioxide). In this study, the chemical composition of the Williams Fork fluids is necessary in order to calculate their acoustic properties for fluid substitution purposes (Figure 1-4).

1.3.3 Production history

Although gas production in the Williams Fork at Rulison Field began in the 1960s, commercial production occurred in the mid-1980s, primarily through the use of

hydraulic-fracturing technology. Within the basin-centered accumulation, dry holes are rare, but uneconomic wells, due to insufficient permeability in areas of little natural fracturing, can occur. The discontinuous nature and very low permeability of these sandstones require well spacing of 20-acres or less to adequately drain the reservoir (Cumella and Ostby, 2003).

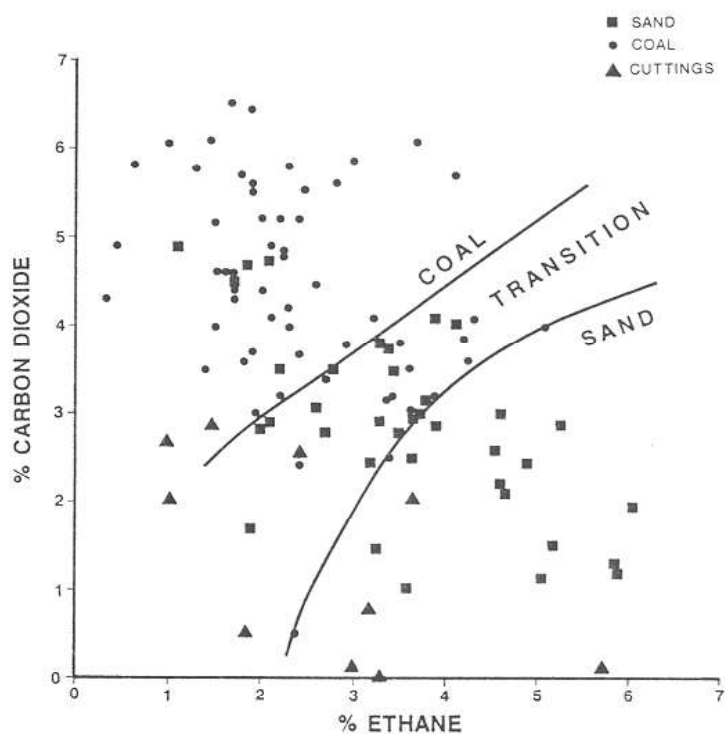


Figure 1-4 Comparison of gas composition based on carbon dioxide and ethane contents of gas samples desorbed from Cameo coal cuttings and produced from Cameo coalbeds and from sandstones above the Cameo (Reinecke et al., 1991).

The reservoir pressure varies from 2250 psi at normal hydrostatic gradient (0.433 psi per foot) at 5200 ft to 4500 psi at higher gradients (0.68 psi per foot) at 6500 ft in overpressured areas (Figure 1-5). Pore pressure increases with depth to progressively

overpressured gradients. During primary depletion processes reservoir pressure decreases, however, areas not connected to drained zones, due to high heterogeneity in the reservoir, stay at higher pore pressures.

The pore pressure data were obtained from well tests (Nelson, 2002). The red line shown in Figure 1-5 joins the measured pore pressure points.

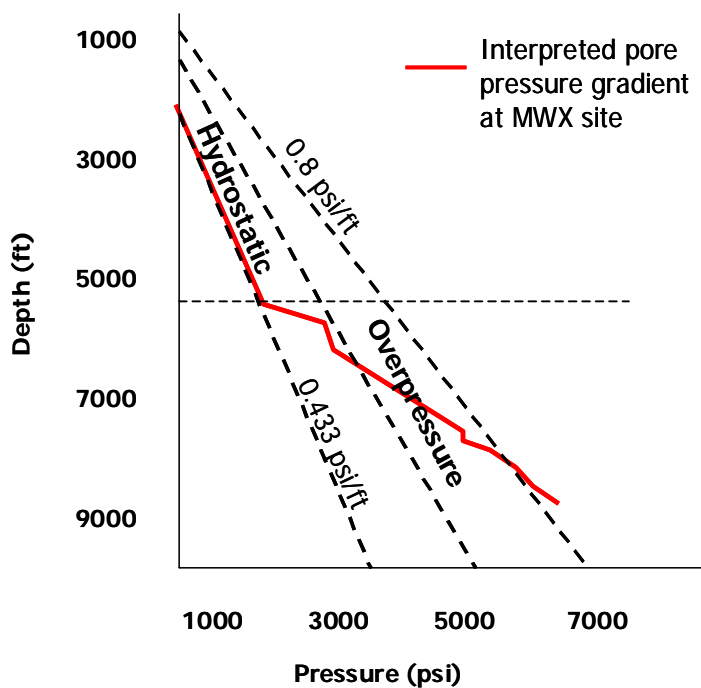


Figure 1-5 Pore pressure gradient measurements as function of depth at the U.S. DOE's MWX-site. Modified from Spencer (1989). Pore pressure increases with depth to progressively higher gradients. Top of reservoir approximately at 5100 ft of depth (dashed line).

1.3.4 4D 9C-seismic data and cross-dipole sonic logs

During October 2003, RCP (Reservoir Characterization Project at Colorado School of Mines) acquired a 9C multicomponent seismic survey of a rectangular

configuration of 7.2 ft (2.2 km) by 8.2 ft (2.5 km), for a total area of 59 ft² (5.5 km²) (Figure 1-6). One year later, during October 2004 a monitor multicomponent survey was acquired with similar acquisition parameters that guarantees seismic repeatability. Two cross-dipole sonic logs were acquired inside the RCP survey area during the last two years. There is a P-wave survey acquired by DOE in 1996. Figure 1-6 shows the location of the different data sets available at Rulison Field. This study focuses in the 2003 multicomponent seismic data, the two dipole sonic logs and the information available from the MWX-site, especially the core analysis (Figure 1-6).

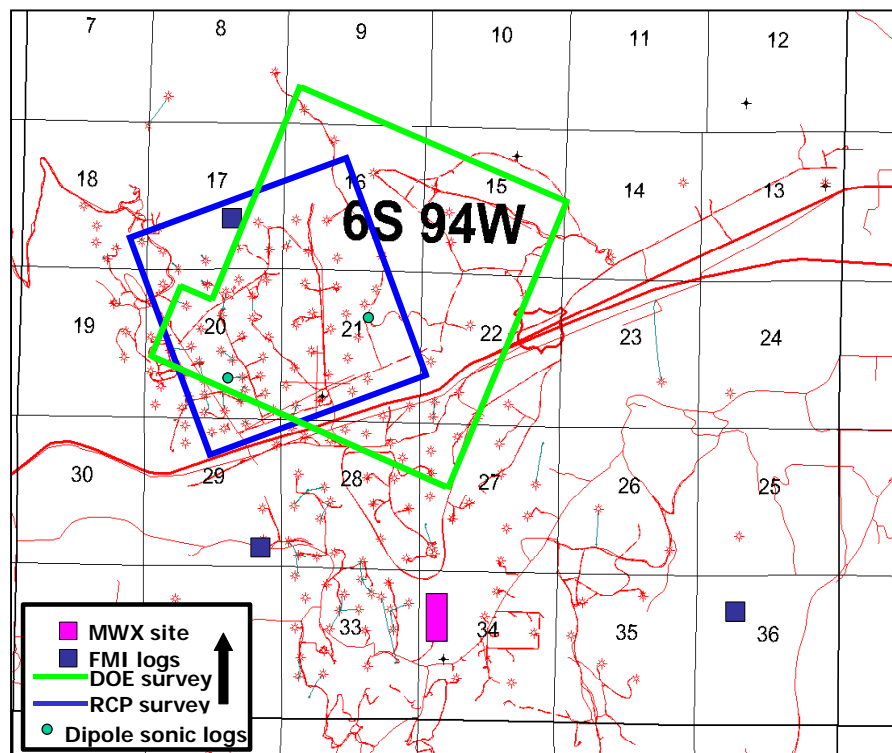


Figure 1-6 Location of RCP's 4D 9C survey area (blue line), DOE's P-wave survey (green line), U.S. Multiwell experiment site (purple rectangle), two cross-dipole sonic logs (green dots), FMI's location (blue squares).

1.3.5 U.S DOE's multiwell experiment site description

U.S. DOE's Multiwell Experiment (MWX) was a research-oriented field experiment, during 1981-1988, aimed at improved characterization and gas production from low-permeability reservoirs typified by the Mesaverde Group in western Colorado. The MWX site is located in the Rulison Field in the east-central portion of the Piceance basin (Figure 1-6). Different activities were conducted during eight years of research. The results from this research project yielded contributions to the understanding of tight gas sandstones.

Results obtained during this research project are reviewed in this thesis as background information that refers to reservoir parameters related to different depositional environments at the MWX-site and that are directly applicable to Rulison Field. Furthermore, ultrasonic measurements conducted in this thesis research complement the core measurements done during the MWX research project.

The principal objective of the MWX project was to obtain geological information of tight gas sandstones to unlock these resources. Detailed core analysis, log and well test data was collected for detailed reservoir characterization from three wells closely spaced (<225 ft) and at depths ranging from 7550 to 8350 ft (MWX-1, MWX-2 and MWX-3).

More than 4100 ft of core were analyzed. Routine and special core analysis was conducted. The routine core analysis included determination of water saturation and porosity. Porosities of sands were usually 5–10%. Water saturations averaged approximately 65% at the top of the Mesaverde Formation and 30–35% in some of the

productive sands. Porosities were measured under confining stress and little changes in porosity were observed with confining pressure (Sattler, 1989).

Special core analysis included measurements of dry, restored pressure-state permeabilities, pressure core, capillary pressures, electrical properties, and permeabilities of naturally fractured core. Dry Klinkenberg permeability measurements were performed to determine the variation of permeability over sandstones. Results show the dependence of permeability on confining pressure (Jones and Owens, 1980). Effects of water saturation can reduce dry-core gas permeabilities by an order of magnitude or more (Wei, 1986). For example, water saturations at 15, 30, 40, and 50% reduced the gas permeabilities of a fluvial core sample by multipliers of 0.53, 0.24, 0.11, and 0.02, respectively, at confining pressure of 3000 psi.

Some relevant observations from the MWX-core analysis (Sattler, 1989) are pointed out here:

- Dry Klinkenberg permeability measurements range from microdarcies to tens of microdarcies.
- The permeability of a tight sandstone core plug depends more on the effective stress (confining stress minus pore pressures) than on the individual values of either the confining pressures or the pore pressures.
- Temperature has very minimal effect on permeability (Wei, 1986).

- Porosities are 5 to 10%, and no higher than 15%. Porosities change little with confining pressure. Changes in porosity are less than 2% for 1000 psi confining pressure change.
- Water saturations averaged around 65% at the top of the Mesaverde and 30 to 35% in some of the productive sands.
- Permeability depends strongly upon water saturation. Effects of water saturation can reduce dry-core permeabilities an order of magnitude or more. Generally, the less permeable the core, the more dependent the permeability is on water saturation.
- The permeability of the core with natural fractures is much greater than that from the matrix rock alone at zero percent water saturation. On the average, the dry permeability of the fractured-core plugs along fractures were significantly higher than those from the unfractured plugs, sometimes by over an order of magnitude (Lorenz et al., 1989).

1.4 Method and approach

The following phases describe the scope of the work presented in this thesis. The strategy for this thesis is to develop rock physics based charts that relate rock elastic properties, petrophysical properties, and reservoir conditions from core and log data, and then applied these trends to P- and S-impedance inverted seismic to identify areas of interest in the field.

Phase 1- Laboratory studies and numerical modeling: This phase includes: (1) Selecting and preparing the rock samples (15 samples); (2) Characterizing the rock samples using optical and scanning electron microscope images, X-ray & point count mineralogy, nitrogen permeability and porosity measurements; (3) Measuring the seismic velocities (P- and S-wave) of two core samples over ultrasonic frequencies under changing confining pressure conditions; (4) Calculating velocities at in-situ saturation conditions from dry-rock velocity using Gassmann's fluid substitution equation; and (5) Analyzing experimental results and quantifying instrumental errors.

Phase 2- Cross-dipole sonic log analysis: This phase includes: (1) Log data organization and quality control; (2) Derivation of elastic rock properties of formations from P- and S-wave travel time and density information (P-wave velocity, S-wave velocity, V_p/V_s , I_p , I_s); (3) Identification of relations between elastic rock properties, especially V_p/V_s and impedance, and petrophysical properties; and (4) Development of rock physics based charts for tight sandstone reservoir to assess seismic detectability on different pore pressure, fluid and lithology scenarios.

Phase 3- V_p/V_s from multicomponent seismic data: This phase includes: (1) well ties to multicomponent seismic using dipole sonic logs; (2) Multicomponent traveltime interpretation of seismic reflectors after events correlation in P-, S- and PS-

wave volumes for interval V_p/V_s estimation; (3) P- and S-impedance seismic inversion using P- and pure S-wave data acquired in Rulison Field.

Phase 4- Analysis and integration of results: Because of the wide variety of data and results that are produced from this project, a serious effort was required to integrate results. For example, V_p/V_s obtained from laboratory measurements, cross-dipole sonic and multicomponent seismic data was qualitatively compared and integrated to better define rock physics models and reduce uncertainty in fluid-lithology predictions in the reservoir. This phase focuses in the application of the rock physics based charts (developed in previous phases) to P- and S-impedance inverted seismic data in order to identify areas of interest in the field (overpressure areas, better quality rock, fluid content).

Chapter 2

LABORATORY EXPERIMENTS ON CORE SAMPLES

2.1 Introduction

Laboratory measurements are necessary to understand the elastic response of rocks. The purpose of laboratory work and numerical modeling in this study is to establish an experimental basis for identifying velocities variations due to different lithology, fluid type and fluid pressure changes at Rulison Field. Understanding the effects of gas saturation on the acoustic properties of porous media will be fundamental for using amplitude versus offset (AVO) technique and 4D seismic data in this field.

There is very limited data on acoustic properties of tight gas sandstones and poor understanding of relations between those properties and reservoir properties. Most of the empirical correlations between ultrasonic V_p and V_s with porosity, clay content and effective pressures on shaley sandstones (Eberhart-Phillips et al., 1989) are valid for medium and high permeability rocks, but poor correlations are obtained when applied to tight gas sandstones (Tutuncu et al., 1994).

I collected ultrasonic data on tight gas core samples and present the effect of pressures, lithology and pore fluids on V_p/V_s . Relations between elastic rock properties (e.g., V_p/V_s , P- and S-impedance) and reservoir properties (e.g., pore pressures and pore fluid). Finally, I quantified V_p/V_s variations due to reservoir properties changes in tight

gas sandstones with the potential to apply this information to interpret V_p/V_s extracted from AVO analysis or multicomponent reflection data.

The results from these laboratory experiments are necessary for determining the pressure dependence of rock's elastic properties. In this Chapter, I will describe different aspects of the setup and procedures for the experimental work and analysis of experimental results.

2.2 Sample selection and preparation

The core samples selected for this study are from the U.S. Department of Energy's Multiwell Experiment (MWX) research project. Over 4100 ft of Mesaverde Formation core were taken during the drilling of the three MWX wells. The USGS Core Research Center stores the core samples from three wells (MWX-1, MWX-2, MWX-3).

Sample selection is an important part of this study. A review of logs (e.g., gamma-ray, deep-resistivity, density and neutron porosity) and production histories of the three wells was done. MWX-1 was selected as the best well to study due to all the data available, especially, logs and cores. MWX-1 was the best productive well of the three of them (EUR between 2-2.5 billion cubic feet) and was cored continuously from 4170 ft depth to 6830 ft.

During the core analysis done at the USGS Core Research Center, I correlated log and core data with the purpose selecting cores from producing intervals and representative lithologies of the field (clean sandstones, shaley sandstones and shales).

Areas of interest were identified using log information, for example, the use of neutron and density logs for gas indication.

Four main areas of study were selected, most of them from the fluvial zone of the Mesaverde Fm. which contain heterogeneous strata including lenticular sandstone. Table 2-1 shows the depths and depositional environments of the intervals from where core samples were chosen.

Depth Interval (ft)	Depositional Environment
5530-5570	Fluvial
5720-5740	Fluvial
5820-5840	Fluvial
6415-6435	Coastal

Table 2-1 Depositional environment and depth intervals of core samples chosen at MWX-1 well.

Nine cores were selected from the four zones indicated in Table 2-1. a total of sixteen core plugs were drilled from the core samples selected. The core plugs were taken in vertical and horizontal orientation.

David Northrop and Karl-Heinz Frohne (1990) described the fluvial and coastal intervals from the MWX site. The fluvial interval (4400-6000 ft of depth) consists of irregularly shaped, multistory, composite sandstones that were deposited by broad

meandering-stream systems. The coastal interval (6000-6600 ft) is characterized by distributary channel sandstones that were deposited in an upper delta-plain environment.

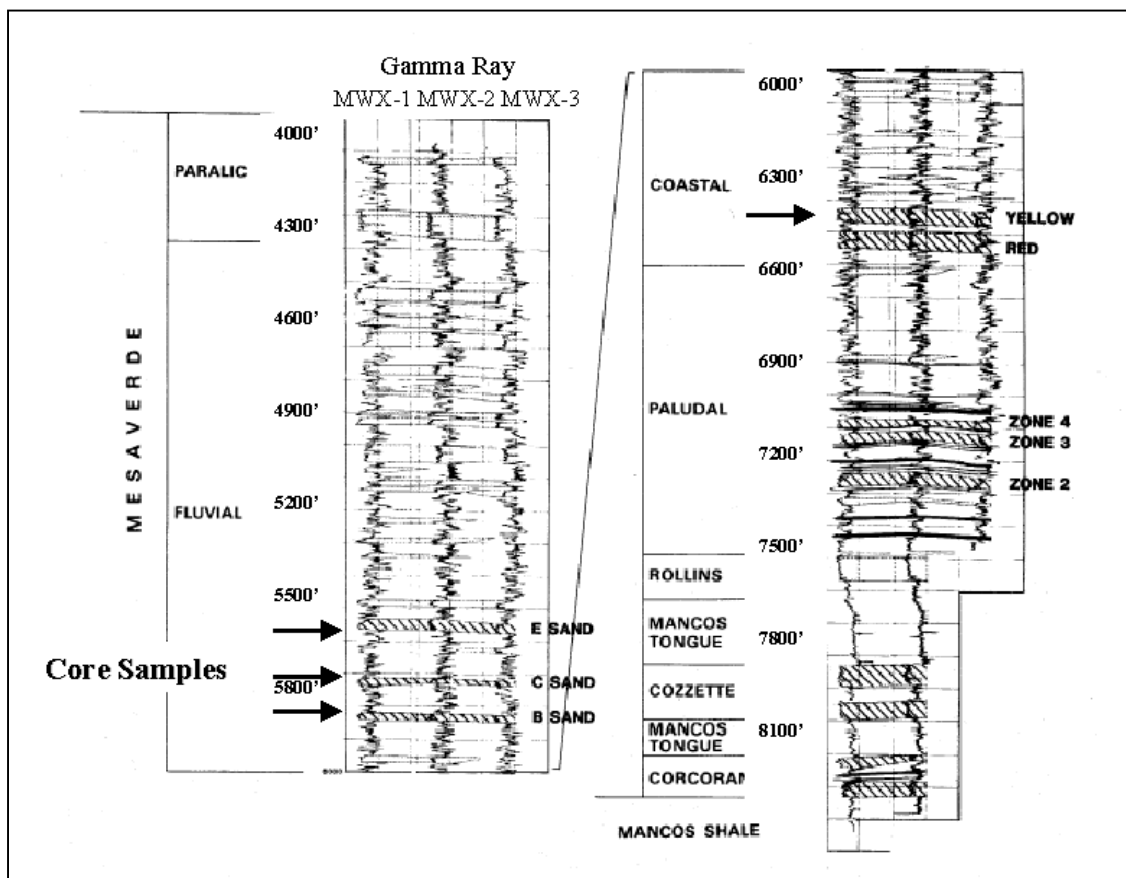


Figure 2-1 The Mesaverde Formation at MWX Site. The black arrows indicate the intervals from which core samples were selected (Sattler, 1989).

The laboratory measurements were made on core plugs. The core samples were drilled to obtain plugs of 1.5 inch of diameter. The sides were parallel and the top and bottom surfaces of these plugs were polished with sandpaper until they were flat and smooth.

ID	Depth (ft)	Orientation	Lithology
R-5557H	5557.0	Horizontal	Very fine to fine sands
R-5557V		Vertical	
R-5566.2H	5566.2	Horizontal	Siltstone, very fine grained, consolidated
R-5566.2H		Vertical	
R-5702H	5702.0	Horizontal	Shale
R-5702V		Vertical	
R-5719H	5719.0	Horizontal	Coarse grained sands
R-5719V		Vertical	
R-5727.1H	5727.1	Horizontal	Coarse grained sands
R-5727.1V		Vertical	
R-5837V	5837.0	Vertical	Coarse grained sands
R-6436V	6436.0	Horizontal	Coarse grained sands
R-6436V		Vertical	
R-6451.5V	6451.5	Horizontal	Siltstone, very fine grained, consolidated
R-6451.1V		Vertical	

Table 2-2 Sample ID, depth and lithology for each core sample.

2.3 Sample characterization

It is very important to know exactly what kind of material are we measuring in the laboratory. For this purpose porosity, grain density, and permeability were measured. Mineralogical description was done, using X-ray diffraction methods. Scanning electron microscope (SEM) pictures were taken to have a qualitative measure of the mineral and pore structures.

2.3.1 Petrophysical description

Porosity and permeability measurements were performed at the Center for Rock Abuse at the Colorado School of Mines.

2.3.1.1 Permeability measurements

Klinkenberg corrected permeability measurements were performed to obtain information of the variation of permeability over the samples selected and to study permeability anisotropy between vertical and horizontal plugs. The method to measure permeability was a steady state nitrogen permeability performed at a confining pressure of 500 psi. The sample is held in a pressure vessel where confining pressure is applied, and gas is passed through it. By knowing the dimensions of the sample, the pressure differentials and flow rate, pressure flow parameters of the gas (nitrogen), the permeability is calculated. The permeability measurements were performed using dry industrial nitrogen gas. Nitrogen Permeability is calculated by using Darcy's law (Equation 2-1), and these measurements are later corrected by Klinkenberg effect.

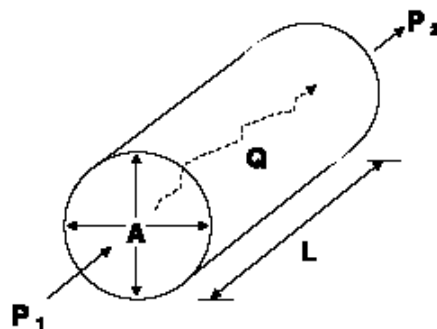


Figure 2-2 Diagram of permeability measurement on a core sample.

$$k = \frac{Q\mu L}{A(P_1 - P_2)} \quad (2-1)$$

where: Q is the flow rate,

A is the area,

L is the length of the sample,

μ is the viscosity of the nitrogen, and

$P_d = P_1 - P_2$ is the pressure differential.

Permeability error calculation

$$\Delta k = \frac{\partial k}{\partial L} \Delta L + \frac{\partial k}{\partial A} \Delta A + \frac{\partial k}{\partial P_d} \Delta P_d + \frac{\partial k}{\partial Q} \Delta Q \quad (2-2)$$

$$k_{error} = \frac{Q\mu}{AP_d} \Delta L + \frac{Q\mu L}{A^2 P_d} \Delta A + \frac{Q\mu L}{AP_d^2} \Delta P_d + \frac{\mu L}{AP_d} \Delta Q \quad (2-3)$$

where, k_{error} is the relative permeability error.

ΔL is the error in sample length measurements, $\Delta L=0.01\text{mm}$,

ΔA is the error in area calculations due to errors in diameter measurements,

$\Delta A=0.06 \text{ cm}^2$,

ΔP_d is the error in pressure measurements, $\Delta P=0.2 \text{ psi}$ and,

ΔQ is the error in flow rate measurements, $\Delta Q=0.003 \text{ cm}^3/\text{s}$.

The relative errors in the nitrogen permeability errors, estimated as $\pm 1 \mu\text{D}$, were mainly due to errors in area and length measurements, and flow rate measurements. The lower the permeabilities the larger the relative error in the measurement.

When measuring gas permeability it is important to correct the measurements for gas slippage phenomena. In general, it is known that with highly permeable media, the differences between liquid and gas permeabilities are very small, whereas these differences are considerable for media of low permeability (Klinkenberg, 1941). The permeability to a gas is a function of the mean free path of the gas molecules, and thus depends on factors, which influence the mean free path, such as the pressure, temperature, and the nature of the gas.

The gas slippage or Klinkenberg effect is large in tight gas sands. Different correlations have been proposed in the past to correct the Klinkenberg effect in routine laboratory measurements.

In this study, the nitrogen permeabilities measurements range from approximately 5 to 94 microdarcies. The relation between the apparent and the true permeability of an idealized porous system to gas is expressed in Equation 2-4.

As indicated by Equation 2-4, the “*b*” factor is an index of the magnitude of the gas slippage effect. It is often regarded as the fractional increase in apparent permeability, which would be observed when measuring permeability with gas at atmospheric pressure. Jones and Owens (1979) shows permeability measurements in more than 100 tight gas sand samples, and found that his tight gas and data was scattered closely about a straight

line not greatly different from an extrapolation of the best fit straight line thought the higher permeability 1950 Penn State data.

$$k_g = k_L \left(1 + \frac{b}{P}\right) \quad (2-4)$$

where, k_g is the gas (nitrogen) permeability, also called apparent permeability,

k_L is the liquid permeability that can be approximated by the Klinkenberg correction,

b is the Klinkenberg factor, and

P is the average pressure.

Nitrogen permeability data measured in this study is at a constant confining pressure of 500 psi. The liquid permeability can be approximated by the Klinkenberg correction (measuring gas permeability at two or more pore pressures and extrapolating to infinite pressure, i.e., the reciprocal of pressure equals zero). Since permeability measurements were done at a constant pore pressure, it was necessary to use empirical correlations for Klinkenberg correction published in the literature. Two correlations were used to calculate Klinkenberg's "b" factor. The 1950 Penn State correlation (Equation 2-5) and the 1979 Jones and Owens tight gas sand correlation (Equation 2-6) are shown.

$$b = 0.777 k_L^{-0.39} \quad (2-5)$$

$$b = 0.86 k_L^{-0.33} \quad (2-6)$$

Figure 2-3 shows the Klinkenberg “*b*” factor calculated using both correlations as a function of Klinkenberg permeability. The tight gas sandstone correlation (Equation 2-6), yields values of “*b*” factor sufficiently accurate for this data set.

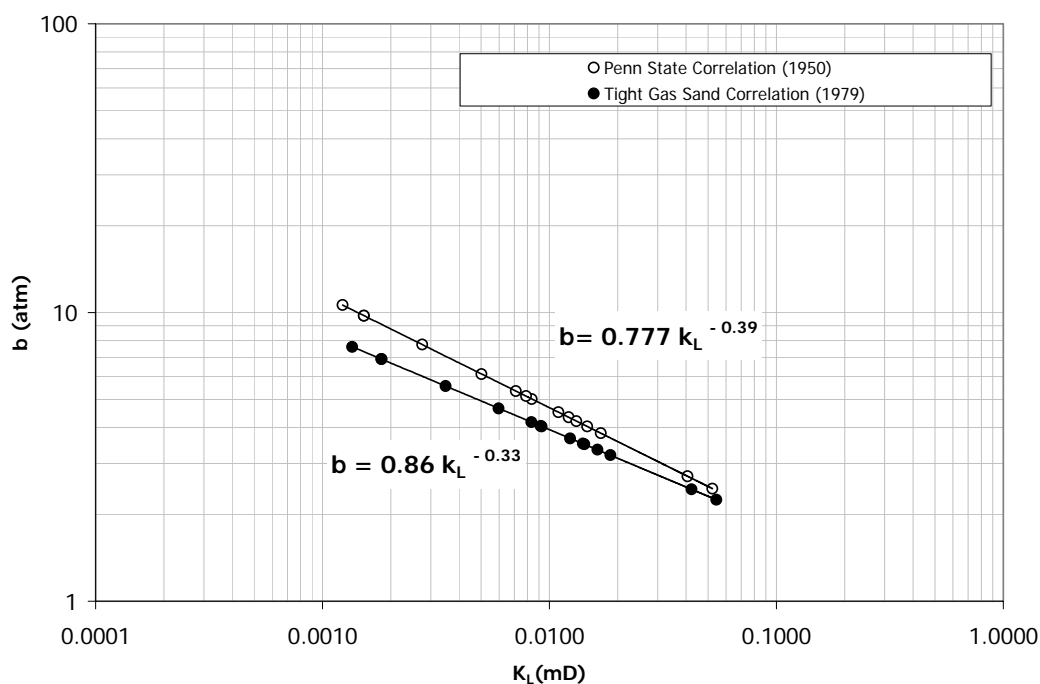


Figure 2-3 Klinkenberg “*b*” factor as a function of Klinkenberg-corrected permeability using two empirical correlations, Penn State correlation (1950) and Tight Gas Sand correlation (1979).

Klinkenberg-corrected permeability range from 1 to 54 microdarcies (Figure 2-4).

Figure 2-4 shows that the differences between Klinkenberg-corrected (approximation of permeability to a liquid) and nitrogen permeabilities are considerable for media of low permeability.

From Figure 2-4 it is possible to observe that the variations between the nitrogen and Klinkenberg corrected permeabilities are larger at low permeabilities. Therefore, it is very important to correct permeabilities measured in the laboratory for gas slippage effect.

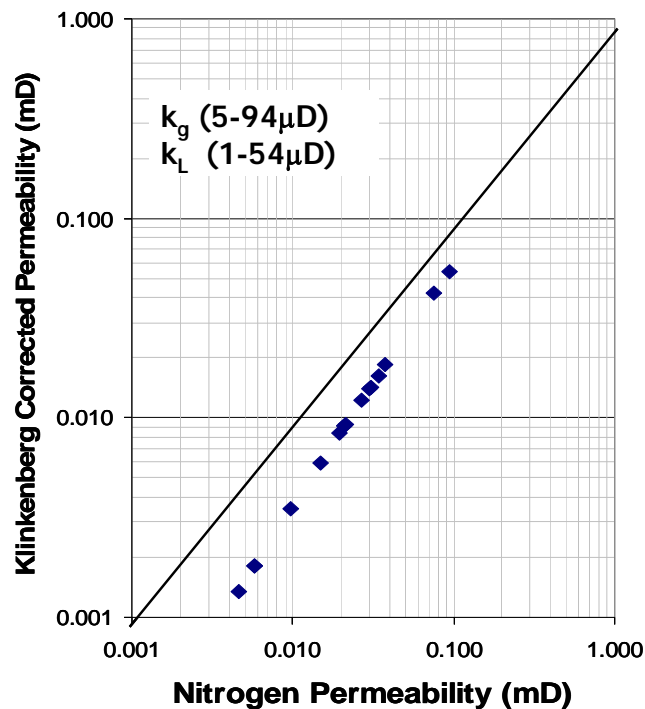


Figure 2-4 Klinkenberg-corrected permeability as a function of nitrogen permeability.

2.3.1.2 Porosity measurements

The porosity was measured by saturation with a liquid, such as water. In this method, based in the Archimedes's principle, the core is carefully extracted of oil, water, and salt, then dried and weighed (W_{dry}). The core is saturated completely with a known-density liquid (ρ_f), all surface liquid is removed carefully, and the core is weighted (W_{sat}) to determine the pore volume (V_p). The core is weighted again while submerged (W_{sus}) in

the same liquid to determine the bulk volume (V_b). This method is tedious, and requires careful technique, however is very accurate for consolidated rocks, such as tight gas sandstones.

Bulk volume

$$V_b = \frac{W_{sus}}{\rho_f} \quad (2-7)$$

where: V_b is bulk volume,

ρ_f is the density of the fluid, and

W_{sus} is the weight (mass) of the plug suspended in the liquid.

Pore volume

$$W_f = W_{sat} - W_{dry} \quad (2-8)$$

$$V_\phi = \frac{W_f}{\rho_f} \quad (2-9)$$

where: V_ϕ is the pore volume,

W_f is the weight or mass of the pore fluid,

W_{sat} is the weight of the core saturated with a density-know liquid, and

W_{dry} is the weight of the dry core sample.

Fractional porosity

$$\phi = \frac{V_{\phi}}{V_b} \quad (2-10)$$

where: ϕ is fractional porosity.

Bulk density

$$\rho_b = \frac{W_{dry}}{V_b} \quad (2-11)$$

where: ρ_b is bulk density.

Grain (mineral) volume

$$V_g = V_b - V_{\phi} \quad (2-12)$$

where: V_g is the grain volume.

Grain (mineral) density

$$\rho_g = \frac{W_b}{V_g} \quad (2-13)$$

where: ρ_b is bulk density.

Porosity error calculation

Porosity can be re-written as Equation (2-14), where W_{sat} , W_{dry} , W_{sus} were measured in the laboratory and the error for each measurement is known.

$$\phi = \frac{W_f}{W_{sus}} = \frac{W_{sat} - W_{dry}}{W_{sus}} \quad (2-14)$$

$$\Delta\phi = \frac{\partial\phi}{\partial W_{sat}} \Delta W_{sat} + \frac{\partial\phi}{\partial W_{dry}} \Delta W_{dry} + \frac{\partial\phi}{\partial W_{sus}} \Delta W_{sus} \quad (2-15)$$

$$\phi_{error} = \frac{1}{W_{sus}} \Delta W_{sat} + \frac{1}{W_{sus}} \Delta W_{dry} + \frac{W_{sat} - W_{dry}}{W_{sus}^2} \Delta W_{sus} \quad (2-16)$$

where, ϕ_{error} is the relative porosity error,

ΔW_{sat} is the error in saturated sample weight measurements,

ΔW_{dry} is the error in dry core sample weight measurements, and

ΔW_{sus} is the error in suspended core sample weight measurements.

The relative errors in the porosity measurements, estimated within ± 0.005 porosity units, or $\pm 0.5\%$ if porosity is in percentage, were mainly due to errors in the weight measurements (instrumental error $\Delta W = \pm 0.1\text{g}$). Tight gas sandstones have very low porosity and the lower the porosity the higher the error in the measurements.

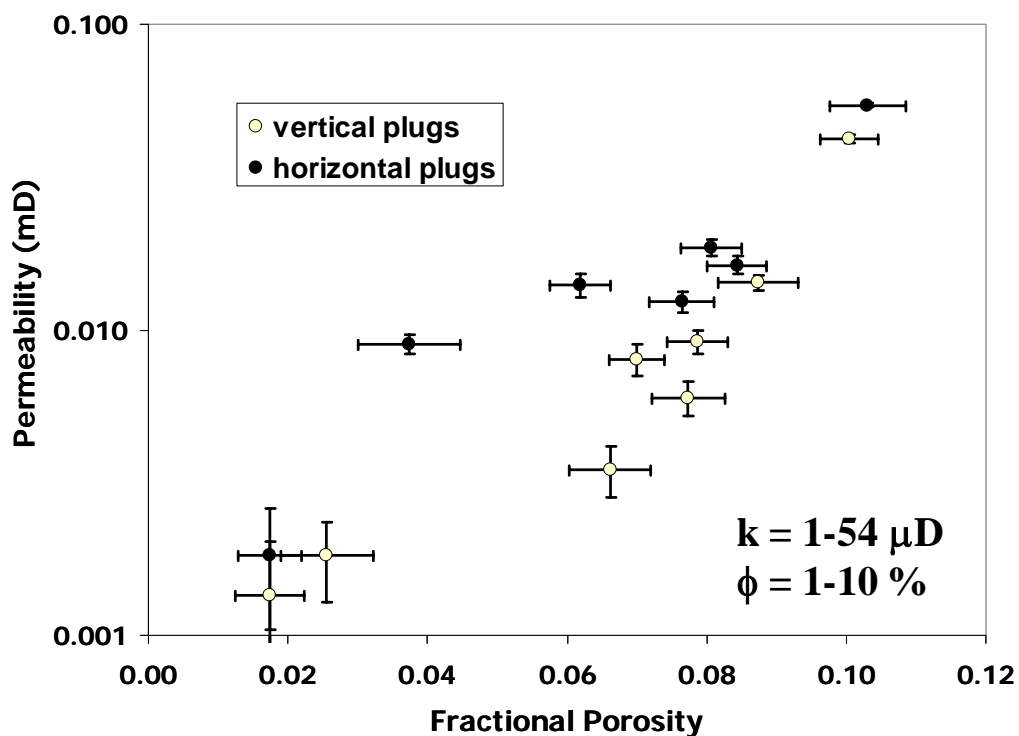


Figure 2-5 Klinkenberg corrected permeability versus fractional porosity.

In Table 2-3, the petrophysical values are shown for all the samples used in this study. The measured grain density is a good indication for the mineral composition of the samples. Pure quartz has a density of 2.65 g/cc and the comparison with the obtained values indicates that most of the samples are sandstones with different clay content.

Sample	Depth (ft)	Orientation	Fractional Porosity	Permeability (mD)	Grain Density (g/cm ³)
R-5557H	5557.0	Horizontal	0.062	0.014	2.62
R-5557V		Vertical	0.070	0.008	2.63
R-5566.2H	5566.2	Horizontal	0.037	0.009	2.71
R-5566.2H		Vertical	0.026	0.002	2.66
R-5702H	5702.0	Horizontal	0.017	0.002	2.68
R-5702V		Vertical	0.017	0.001	2.69
R-5719H	5719.0	Horizontal	0.103	0.054	2.63
R-5719V		Vertical	0.100	0.042	2.62
R-5727.1H	5727.1	Horizontal	0.076	0.012	2.65
R-5727.1V		Vertical	0.077	0.006	2.65
R-5837V	5837.0	Vertical	0.066	0.003	2.68
R-6436V	6436.0	Horizontal	0.084	0.016	2.64
R-6436V		Vertical	0.087	0.014	2.65
R-6451.5V	6451.5	Horizontal	0.081	0.019	2.65
R-6451.5V		Vertical	0.079	0.009	2.65

Table 2-3 Measured plug porosity, Klinkenberg corrected nitrogen permeability, and grain density for samples used in this study (mD=0.987x10⁻¹¹cm²)

Figure 2-6, 2-7 and 2-8 show permeability, porosity and grain density for all samples plotted. Samples show a very limited range of grain density, close to the grain density of quartz, the variations are due to different clay content. If incomplete saturation occurs (ineffective porosity), mineral densities would fall below 2.65 g/cc. Porosities are very low (0.01-0.12) as well as permeabilities (0.001-0.054 mD). Figure 2-6 shows

scatter data, however, it is possible to observe that lower grain density samples have a higher porosity. Lower grain density samples are related to sandstones.

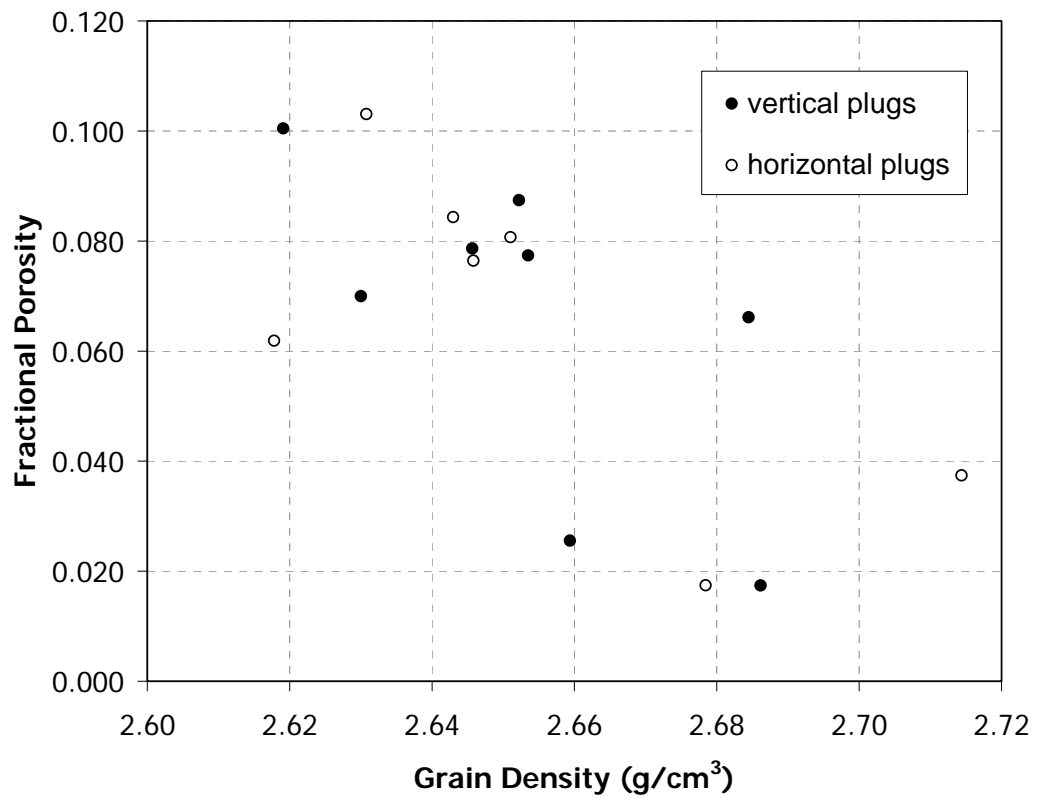


Figure 2-6 Measured plug porosity as a function of grain density.

Figure 2-7 shows scatter data, however it is possible to observe a linear trend where lower grain density samples have a higher permeability. Lower grain density samples are related to sandstones with higher permeability and porosity values.

Figure 2-8 show a crossplot with measured porosity and permeability. It is possible to distinguish to groups from the plot: (1) Low porosity and permeability

samples that represent shales, siltstones, and shaley sandstones; and (2) a group of higher porosity and permeability samples related with very fine to fine grained sandstones.

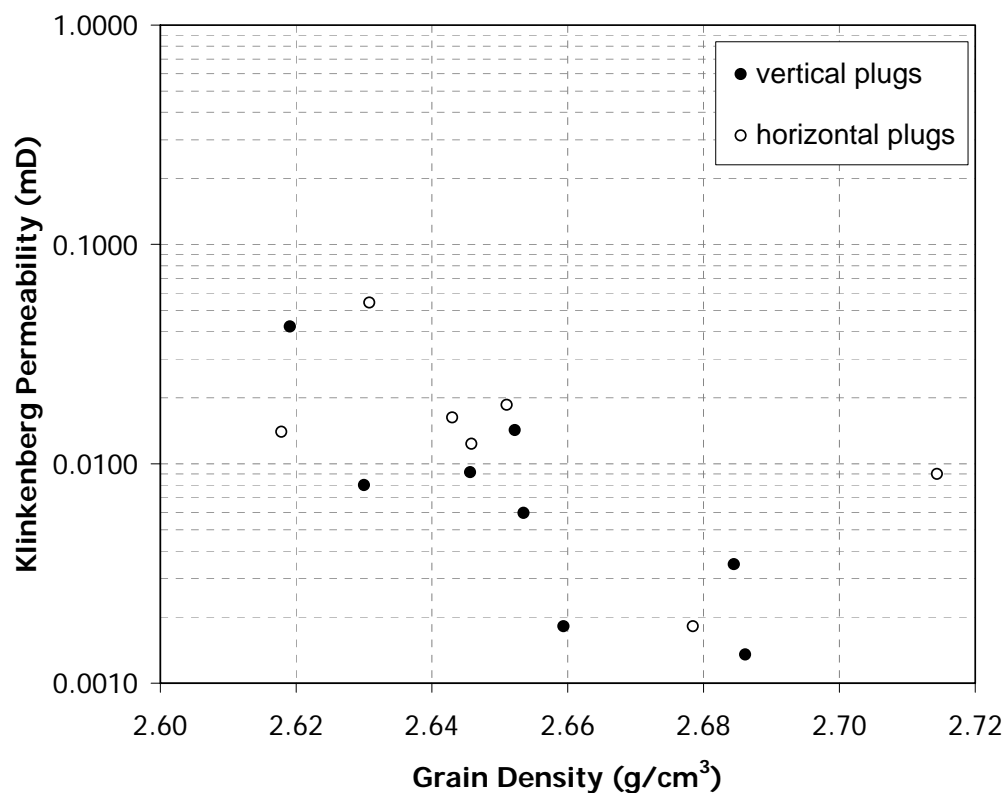


Figure 2-7 Measured plug permeability as a function of grain density.

Figure 2-9 shows a crossplot of measured permeability as a function of measured porosity. Data obtained from horizontal and vertical plugs are plotted to study permeability anisotropy. From figure it is possible to observe higher permeability values for horizontal plugs. Two linear trends are defined, one for vertical plugs and the other for the horizontal plugs.

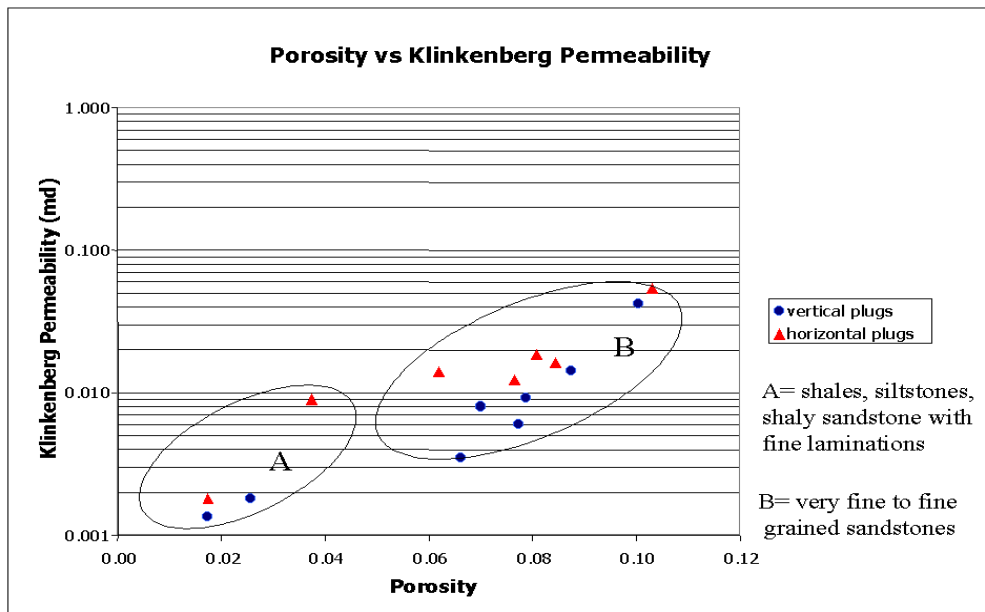


Figure 2-8 Measured plug permeability as a function of plug porosity measurements.

Permeability is a measure of the flow of fluids through a rock; this parameter can be anisotropic as a function of direction of flow. Permeability has been identified as one of the most important parameters controlling reservoir performance.

This parameter changes with rock type and grain size. Permeabilities measured at the same rock in horizontal and vertical direction may differ. In other words, measuring permeability parallel to layers of sedimentary rocks may give a different value to a perpendicular measurement. This directional dependency is related with layering heterogeneity. The anisotropy nature of permeability has been observed at core scale and also at reservoir scale. Layering of rock on a scale smaller than the scale of the measurement will cause high permeability anisotropy, each small layer will have a

different value of permeability but all contribute to the measurement. Crossbedding (alternative layering of sands of different grain size) and thin layers of shale can block most of the vertical flow, making horizontal permeability much higher than the vertical permeability and therefore increasing permeability anisotropy.

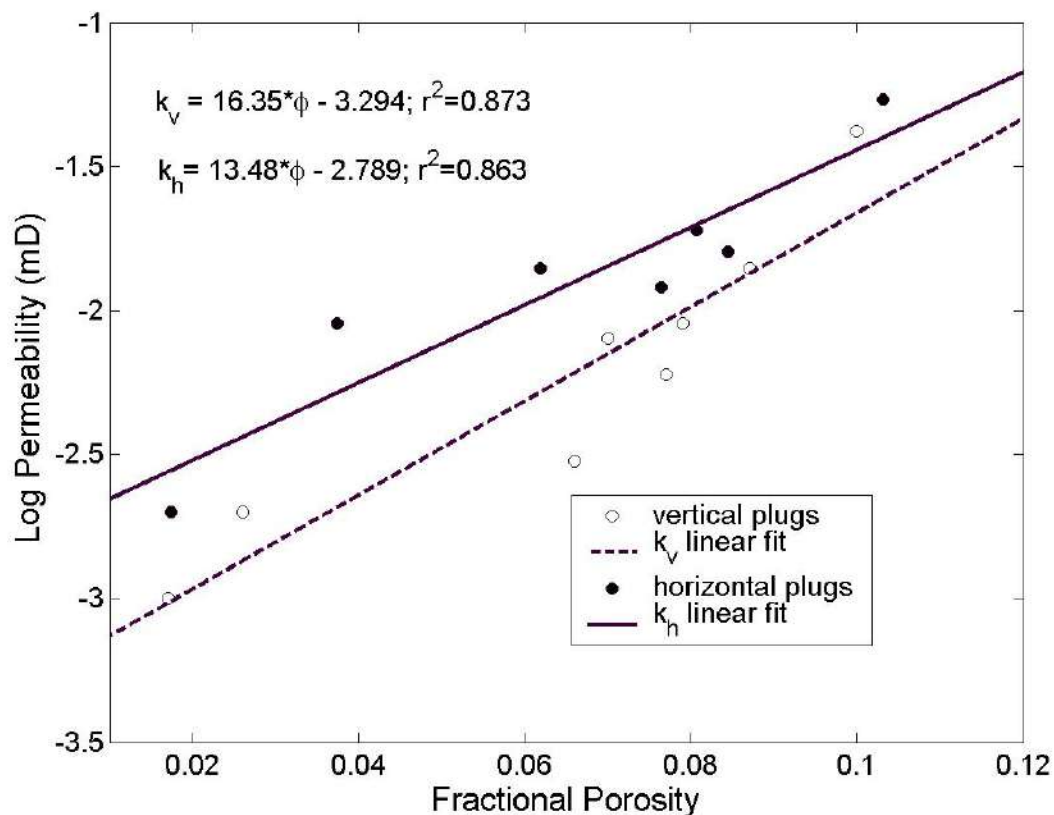


Figure 2-9 Porosity-permeability relationships for vertical and horizontal plugs. Lines are best fit for each data set. There is a general linear relationship between porosity and permeability. Two trends can be identified if the data is separated in horizontal and vertical core plugs indicating permeability anisotropy.

Although anisotropy strictly refers to the directional dependency of a measurement, the ratio between vertical permeability (k_v) and horizontal permeability (k_h)

is often used to quantify permeability anisotropy at different scales (core and reservoir scale). In this study, I measured permeability in vertical and horizontal direction for tight gas sandstones core plug samples. The anisotropic nature of permeability at core scale, will influence the anisotropy at reservoir scale. The problem with anisotropy not only depends on direction, but also may vary with scale. At reservoir and core scale permeability anisotropy is affected by the presence of fractures, thin layers, depositional environment, and in general, heterogeneity.

Figure 2-10 shows a plot of measured plug permeability anisotropy (k_v/k_h) versus depth. The plot shows high heterogeneity at core scale. High vertical permeability values lead to high permeability anisotropy.

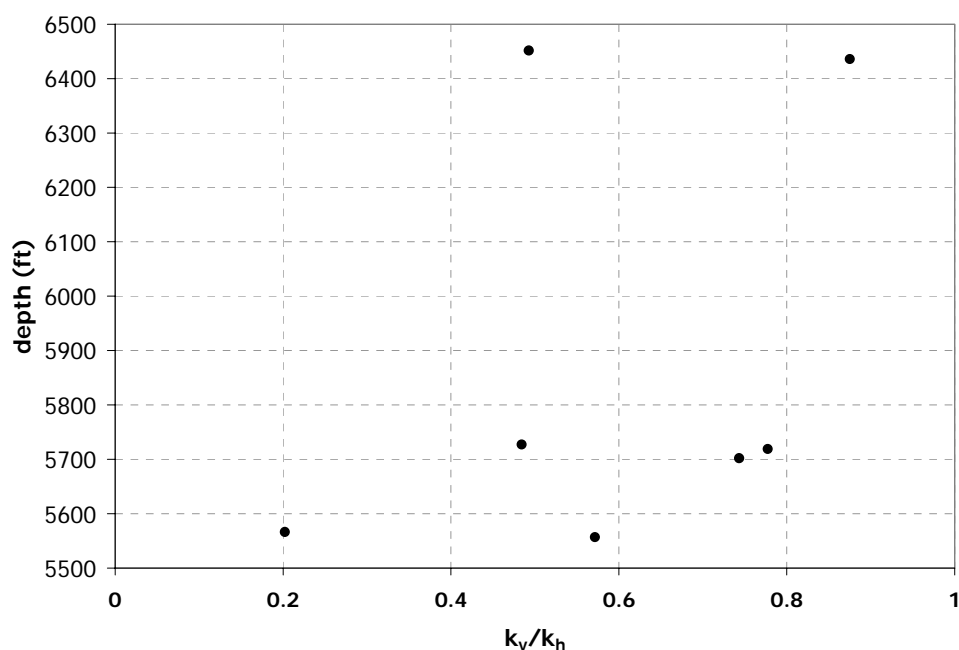


Figure 2-10 Measured plug permeability anisotropy (k_v/k_h) versus depth.

2.3.2 Mineralogical description

In order to characterize better the samples, before ultrasonic measurements were performed, a service company, K/T GeoServices, performed X-Ray Diffraction work in four of the fifteen samples used in this study. XRD is used in this study to (1) characterize the mineralogy of whole rocks, and (2) determine the types of clay minerals. Table 2-4 shows the result of the XRD measurements for four samples of this study. The samples were chosen taking into account the porosity, permeability, grain density and lithology description done.

Sample	R-6451.5V	R-5702V	R-5719V	R-5727.1V
Quartz	68%	58%	66%	73%
K-Feldspar	0%	0%	0%	0%
Plagioclase	10%	9.4%	20%	12%
Calcite	0.6%	18%	0.5%	0.6%
Dolomite	4.4%	4.6%	0%	0%
Siderite	1.6%	0%	0%	0%
Pyrite	0%	0%	0%	0%
Hematite	0%	0%	0%	0%
Gypsum	0%	0%	0%	0%
Anhydrite	0%	0%	0%	0%
Halite	0%	0%	0%	0%
Barite	0.4%	0%	0%	0%
Total Phyllosilicates	15%	10%	14%	13%
Total	100%	100%	100%	100%

Table 2-4 Whole rock mineralogy from results of XRD measurements (weight percentage).

Quartz and plagioclase, are the most common minerals. Phyllosilicates are present in most of the samples consisting of illites and micas (Table 2-5).

Sample	R-6451.5V	R-5702V	R-5719V	R-5727.1V
Mixed layer Illite-Smectite	20%	0%	17%	18%
Illite & Mica	79%	62%	69%	70%
Kaolinite	0.1%	8.1%	2.8%	2.4%
Chlorite	0%	30%	11%	9.7%

Table 2-5 Relative abundance (percentage) of phyllosilicate mineralogy from XRD measurements.

Sample	Major	Minor
R-6451.5V	Quartz, Plagioclase, Phyllosilicates	Dolomite, Siderite, Calcite, Barite
R-5702V	Quartz, Calcite, Phyllosilicates Plagioclase.	Dolomite
R-5719V	Quartz, Plagioclase, Phyllosilicates	Calcite
R-5727.1V	Quartz, Plagioclase, Phyllosilicates	Calcite

Table 2-6 Results of XRD measurements

2.3.3 Scanning electron microscopy

A Scanning Electron Microscope (SEM) was used to characterize the fabric of the samples. SEM can easily produce digital images of minerals, fossils, rocks, sands, and soils magnified 15,000 times. Samples are placed in an evacuated chamber and bombarded by a carefully focused beam of electrons, and the secondary electrons are collected, amplified and used to form an image, typically on a television screen, of the sample's surface (Figure 2-11). Samples are generally first made conductive through a microscopic coating of carbon or a special metal alloy.

Microfractures, grain contact areas, and pore structures can be examined in detail using scanning electron microscopy (SEM). The SEM can be used to understand the influence of microstructure on elastic properties.

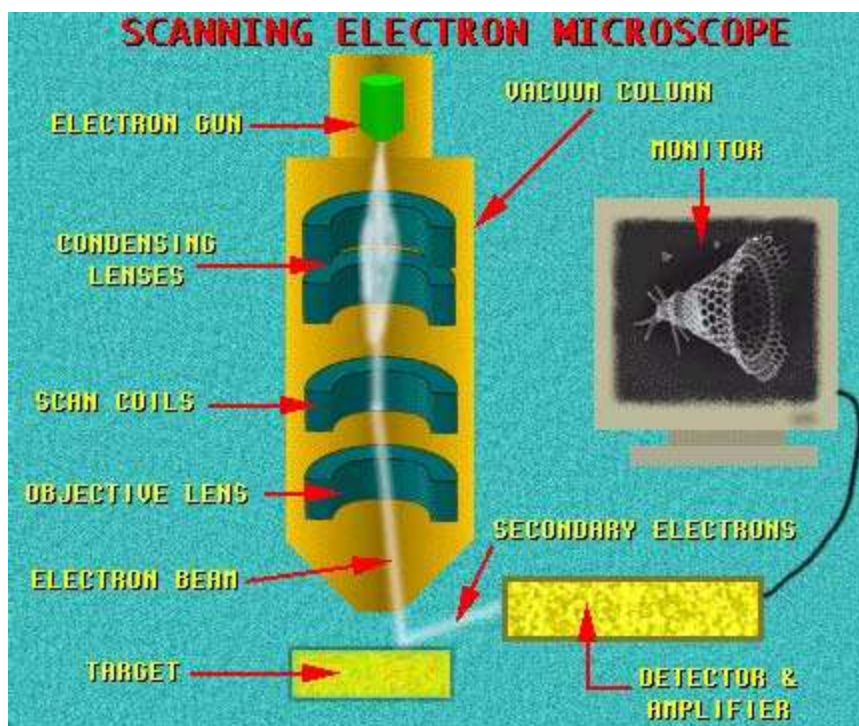


Figure 2-11 Scanning Electron Microscope diagram (Museum of Science, Boston, www.mos.org).

The polished surfaces of rock thin sections are examined in the scanning electron microscope. The thin sections are coated with a metal al to enhance the conductivity of the sample. Figure 2-12 and 2-13 show the thin section images of a typical reservoir tight gas sandstone (sample R-6451.5V) and a shaley sandstone (sample 5566.2H) of the Williams Fork Formation at Rulison Field.

From the images, it is possible to observe that figure have shale thin layers and in general is more heterogeneous that the rock in Figure 2-12. This fluvial environment is highly heterogeneous and this is possible to obverse visually when looking to thin sections of rocks.



Figure 2-12 Thin section of a reservoir tight gas sandstone sample (R-6451.5V). Depth 6451.5 ft, measured plug porosity is 7.9% and Klinkenberg corrected permeability is 0.009 mD.



Figure 2-13 Thin section of a reservoir tight gas shaley sandstone sample (R-5566.2H). Depth 5566.2 ft, measured plug porosity is 3.7%, Klinkenberg corrected permeability is 0.009 mD and grain density 2.71 g/cm^3 .

For more detail SEM is used to understand the presence of cracks in the sample, to try to distinguish between natural and induced cracks, and to observe grain contact

areas, and pore structures. Figure 2-14 shows SEM images at different magnification (50x, 100x, 500x, 1000x) acquired from sample R-6451.5. This sample has a low measured porosity and permeability. Dark areas in the SEM picture indicate pore space, high absorption of electrons, while lighter gray colors indicate heavier elements related to mineral surfaces. Natural cracks are identified because of the presence of cementation along them. Induced cracks are recent and will not show cementation (Figure 2-14). It is also possible to observe small isolated pores that will not contribute to fluid flow.

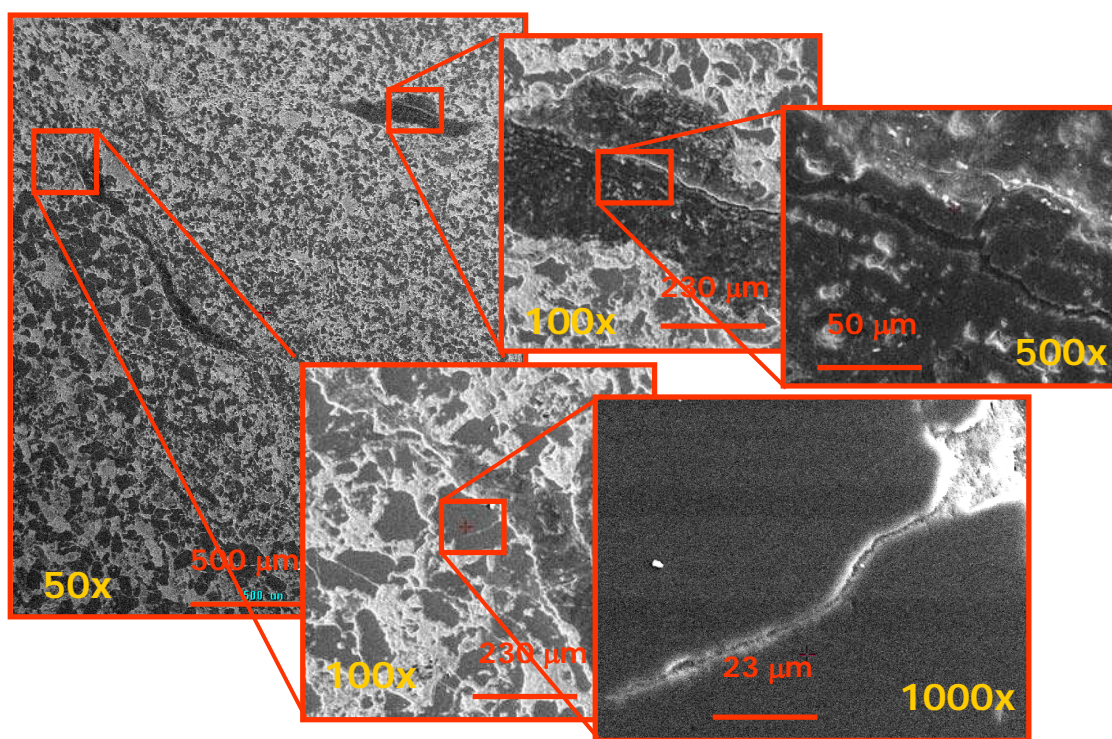


Figure 2-14 SEM pictures of sample R-6451.5 at different magnification (50x, 100x, 500x, 1000x). Depth is 6451.5 ft, measured plug porosity is 7.9% and Klinkenberg corrected permeability is 0.009 mD. A natural fracture (1000x image) shows cementation.

2.4 Ultrasonic velocity measurements

Ultrasonic measurements were performed on core samples from the Williams Fork Formation. The main purpose of doing ultrasonic measurements was to obtain dry rock elastic moduli for fluid substitution and to measured velocity changes to under pressure changes for seismic time-lapse interpretation. Anisotropy tests were conducted before preparing the sample for ultrasonic measurements under pressure.

2.4.1 Anisotropy test at room-conditions

Compressional and shear waves were propagated through each sample before preparing the sample for ultrasonic measurements under pressure. The purpose is to identify the fast and slow direction of propagation of shear wave data in each sample. Three transducers and three receivers were used in the experiment (Figure 2-15). Measurements of the shear wave propagation were recorded each 10 degrees while rotating the sample (Figure 2-16).

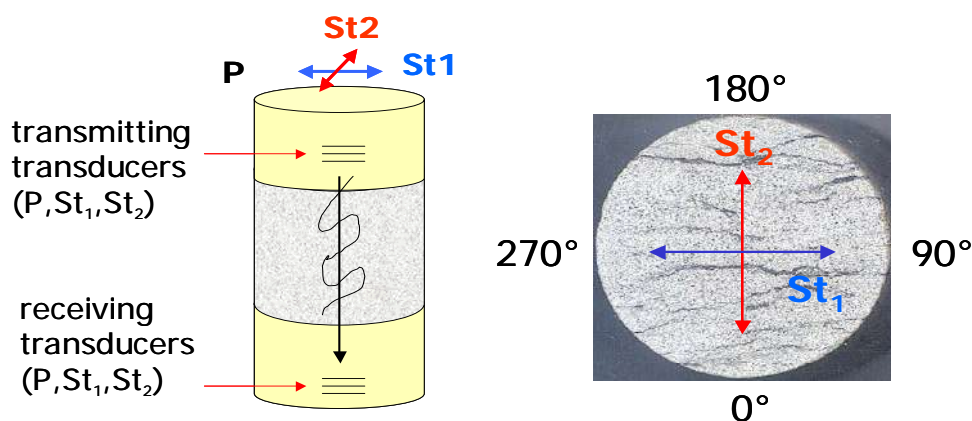


Figure 2-15 Anisotropy test setup at room-conditions. S-wave transducers (St_1 and St_2), are perpendicular to each other while rotating the sample.

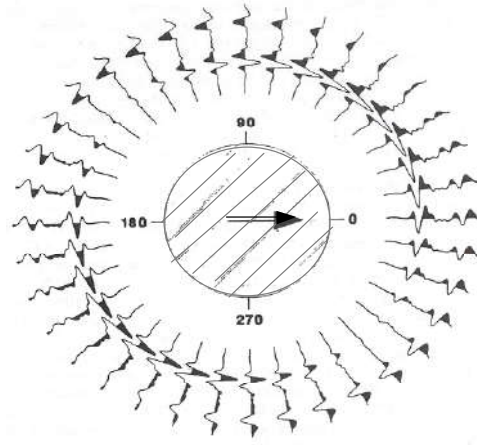


Figure 2-16 Schematic showing azimuthal dependence of shear wave propagation in a core sample. Adapted from Sondergeld and Rai (1986).

Fast and slow directions of shear wave propagation were identified. This information is used when preparing samples for ultrasonic measurements under pressure, with the idea of aligning properly two orthogonal S-wave transducers, one to the fastest and the other to the slowest direction of shear wave propagation in each core sample.

Fast and slow shear wave velocities can be measured in core samples. In most of the cases, fast shear wave velocity is measured when one of the S-wave transducer is aligned parallel to the shaley layers and cracks present in the samples, and the slow shear velocity is perpendicular to the fast shear wave velocity.

Examples of the recorded signals at room-conditions for sample R-6451.5H are shown in Figure 2-17. The P- and two S-wave signals going through sample are recorded.

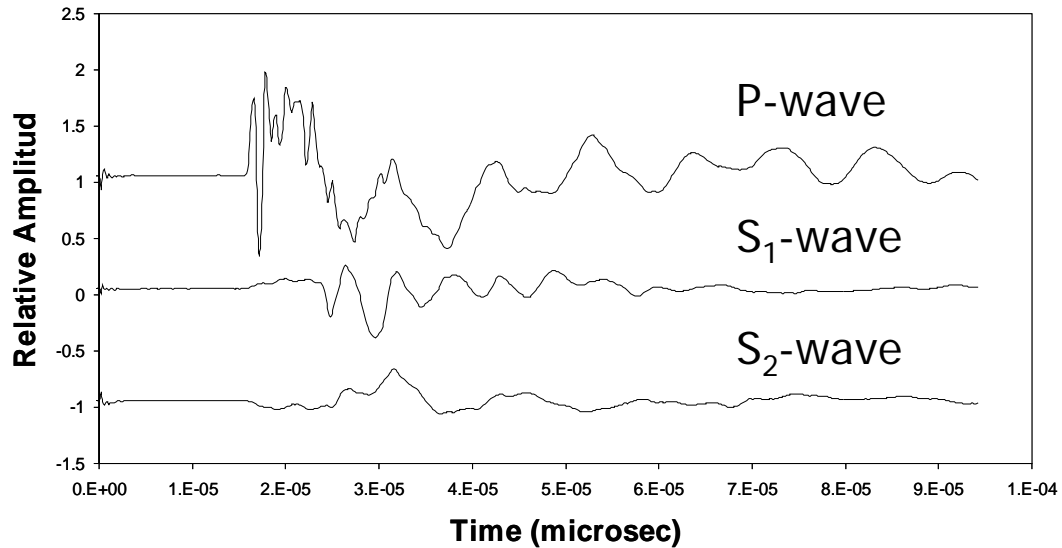


Figure 2-17. Compressional and shear (fast and slow) wave propagation through sample R-6451.5H.

It was possible to identify the directions that correspond to the polarizations of the fast and slow shear-waves. Knowing these directions, the shear splitting parameter for an anisotropic rock with transversely isotropic (TI) symmetry can be calculated (Thomsen, 1986) as shown in Equation 2-17,

$$\gamma \cong \frac{V_{s1}^2 - V_{s2}^2}{V_{s2}^2} \quad (2-17)$$

where γ is the shear-wave splitting parameter, and V_{s1} and V_{s2} are the fast and slow shear-wave velocities. For sample R-6451.5H, V_{s1} and V_{s2} were obtained and γ calculated at room-conditions ($\gamma=11.93\%$). In these measurements, the orientation of the core samples in the borehole was unknown.

2.4.2 Ultrasonic P- and S-wave velocity measurements at varying confining pressure

The experimental setup, instrumental errors and analysis of results are shown in this section.

2.4.2.1 Experimental setup

The P- and S-wave velocities of dry samples were measured as a function of hydrostatic confining pressure using a pulse transmission technique. The experiment diagram and engineering design is shown in Figure 2-18. Figure 2-19 and Figure 2-20 show the measurement assembly and the sample configuration.

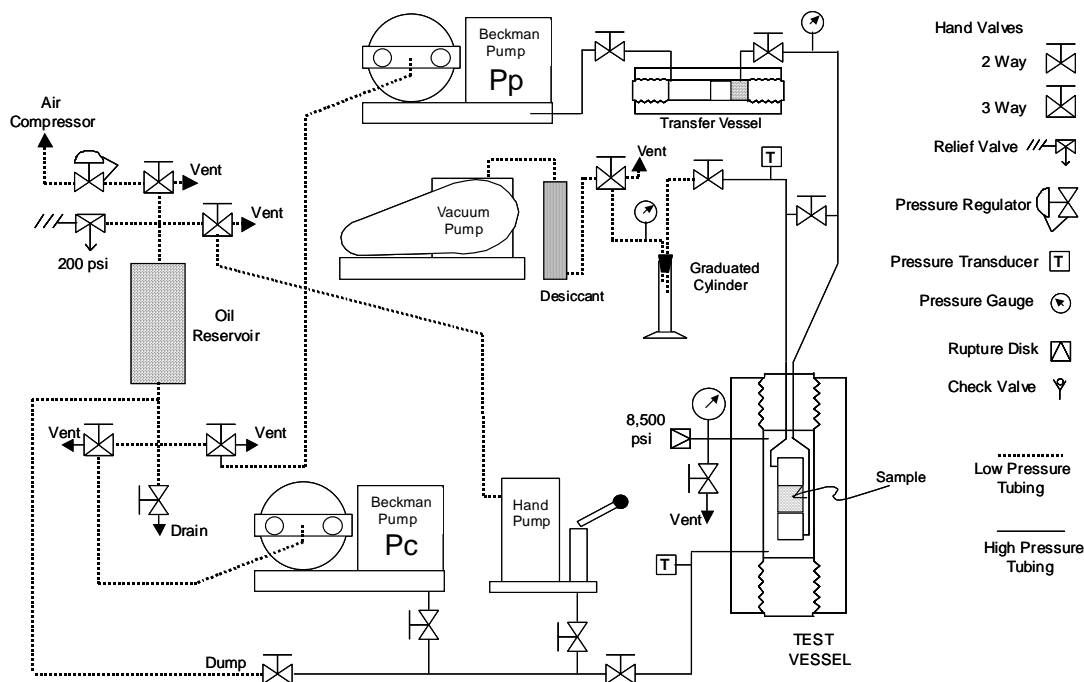


Figure 2-18 Schematic diagram of the pulse transmission technique for a core sample for varying confining and pore pressure (Batzle and Prasad, 2004) at the Center for Rock Abuse at the Colorado School of Mines.

Figure 2-19 shows a picture of the equipment used for the ultrasonic measurements and different components of the experiment setup. The machine was build during Fall 2004 using the engineering design shown in Figure 2-18. The pulse-transmission experimental setup for ultrasonic measurements consisted of a digital oscilloscope (Tecktronix- Model TDS 3014B) and a pulse generator (Parametrics Model 5055PR). Piezo-ceramic transducers were used to generate P- and S-waves. Hydrostatic confining pressure was applied to the sample in a pressure vessel. The confining pressure can range from 0 to 10000 psi (0 to 69 Mpa).

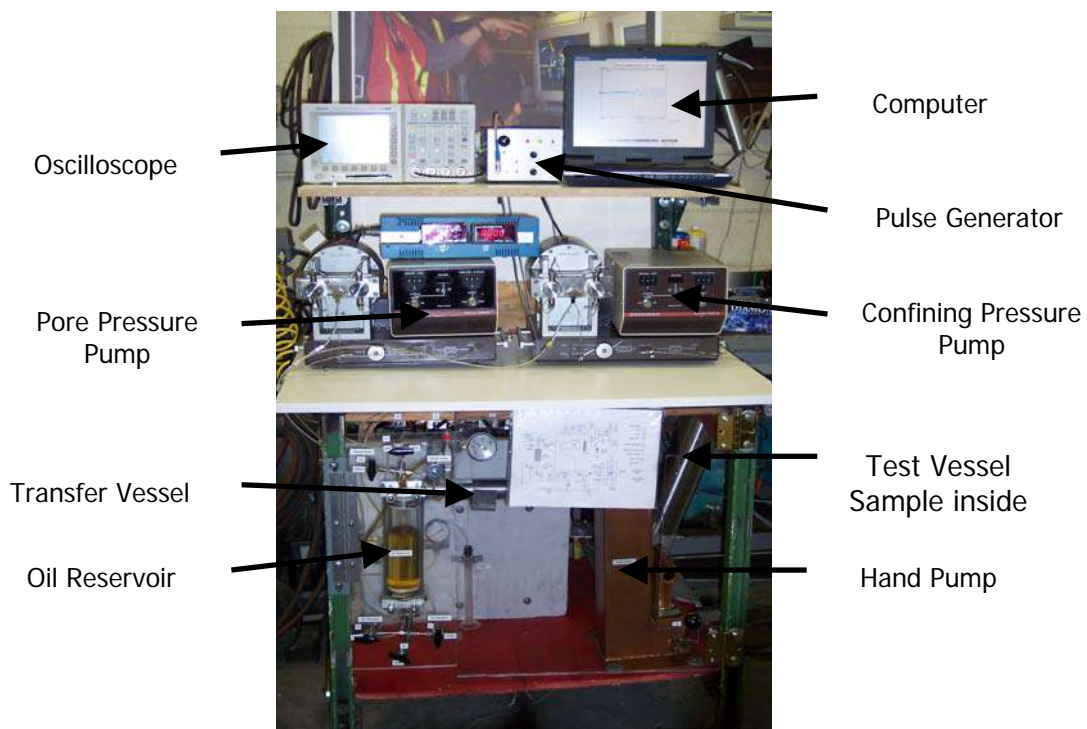


Figure 2-19 Picture of equipment for ultrasonic measurements under confining and pore pressure at the Center for Rock Abuse at the Colorado School of Mines.

The samples were jacketed with rubber tubing and clamped with metal wire (Figure 2-20) to isolate them from the confining pressure. The transducer casing also has pore fluid lines. The transducer wires and pore fluid lines are connected to the ultrasonic testing equipment. The sample is enclosed in a metal confining pressure vessel.

It is possible at the same time to apply pore pressure to the sample. Pore pressure is controlled independently by a pump (Figure 2-19). A transfer vessel allows the fluid in the sample to be changed, for example, from butane to water.

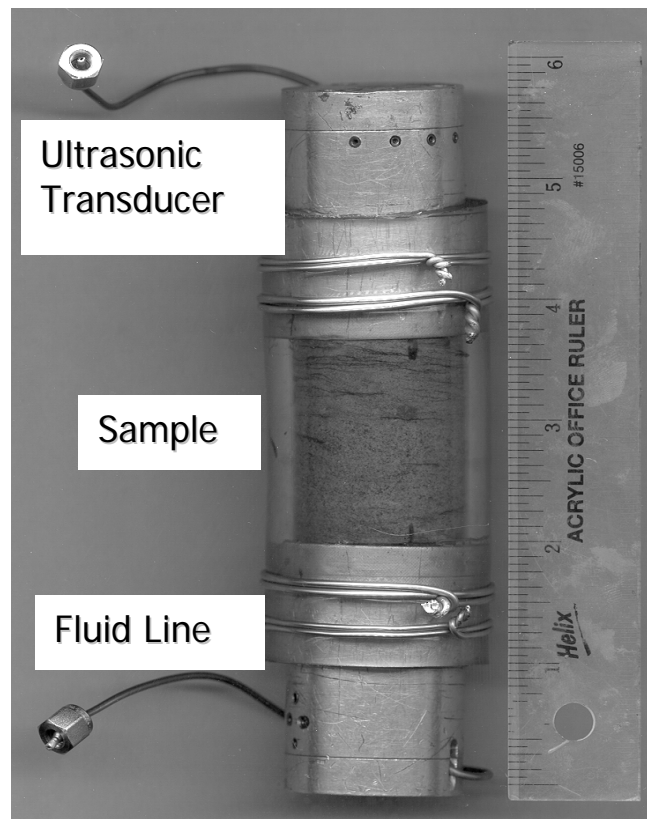


Figure 2-20 Sample setup for ultrasonic measurements.

A pulse generator is used to send a signal to the piezo-ceramic transducers and to trigger the digital oscilloscope used for recording the output signal. The pulses travel through the rock sample and are received at the other end by an identical transducer (receiver) that transforms the mechanical vibrations back into electrical signals. The signal received by the oscilloscope is recorded on a computer and first arrival's interpretation are done for velocity calculations. The principal frequency was about 0.5 MHz for P-wave and S-wave. In this setup, there is an electronic delay time of 9.518 μs for the compressional wave and 16.589 μs for the shear wave. The arrival time must be corrected by the zero-time calibration of the transducer pair.

2.4.2.2 Ultrasonic velocity and error calculations

The velocities are calculated from the travel time of the pulse through the sample. First arrivals are interpreted and the arrival times are corrected by the zero-time calibration of the transducer pair. Velocity of the sample is calculated from its length and the travel time of the signal after correcting the electronics delay time (Equation 2-18).

$$V = \frac{L}{t_M - t_T} \quad (2-18)$$

where, V is P-wave or S-wave velocity,

L is the length of the sample,

t_M is the travel time of the signal, and

t_T is the electronic delay time.

Velocity error calculation

$$\Delta V = \frac{\partial V}{\partial L} \Delta L + \frac{\partial V}{\partial t_M} \Delta t_M + \frac{\partial V}{\partial t_T} \Delta t_T \quad (2-19)$$

$$V_{error} = \frac{1}{t_M - t_T} \Delta L + \frac{L}{(t_M - t_T)^2} \Delta t_M + \frac{L}{(t_M - t_T)^2} \Delta t_T \quad (2-20)$$

where, V_{error} is the relative velocity error,

L is the length of the sample,

ΔL is the error in sample length measurements, $\Delta L = \pm 0.01$ mm, and

Δt_T and Δt_M are the oscilloscope's time resolution $\Delta t = \pm 0.1$ μ s.

The relative velocity error (instrumental error) is less than 3% in P-wave velocity estimation and 2% in S-wave velocity estimation. Errors in picking (human errors) are not quantified here, however from observations during the experimental work, the maximum absolute error for both V_p and V_s is less than ± 50 m/s, including the picking error. It is important to mention that at low differential pressures the error in picking is higher than at higher differential pressures.

2.4.2.3 Dry rock ultrasonic measurements results

Once the sample is properly prepared and placed in the ultrasonic equipment with all the proper connections (signal cables, pressure lines, etc.), dry measurements were conducted. For this case, the pore fluid lines are left open to the air, and the pore pressure pump is not used. Travel times were recorded at different confining pressures, so changes in velocities due to changes in confining pressure can be observed. The confining pressure is incremented for each measurement and later decremented to the starting pressure. The purpose of increasing and decreasing consistently the confining pressure while recording the wave propagation is to observe the stress hysteresis of the sample. Cracks (opening and closing) give rocks a different modulus during loading and unloading; and this process in the lab is reproduced when increasing and decreasing pressures in order to understand this difference in elastic behavior known as hysteresis.

During the measurements, at each confining pressure, it is important to let the pressure system stabilize at least for 5 minutes, in order to reduce errors in the confining pressure recording. At each confining pressure, P-wave and two S-wave measurements are made. The two shear waves are orthogonal and we try to align them to the principal directions of shear wave propagation related to the fabric of the core and obtained through the anisotropy test done at room-conditions before preparing the samples.

For velocity calculations it is necessary to interpret first arrivals of P- and S-waves. First breaks are sometimes difficult to interpret due to noise in the data, attenuation and heterogeneity of the sample.

Examples of the recorded signals at different confining pressures are shown for sample R-5719V. Figures 2-21 and 2-22 show the signals of P- and S-wave when increasing and decreasing confining pressure in sample R-5719V.

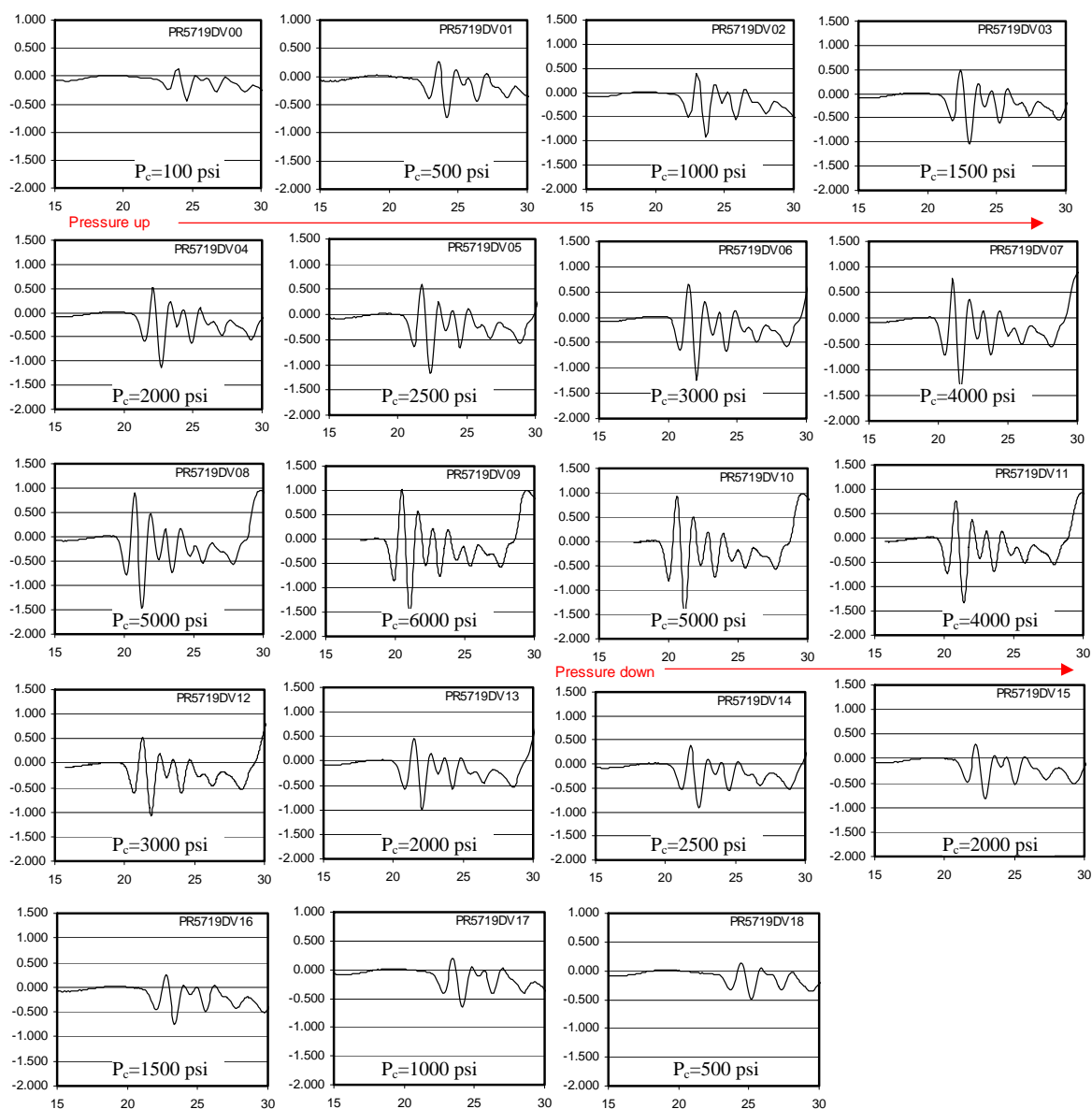


Figure 2-21 P-wave signal through sample R-5719V at different confining pressures.

Sample R5719-V was extracted from depth 5719 ft and has a measured porosity of 10% and permeability of 42 μ D.

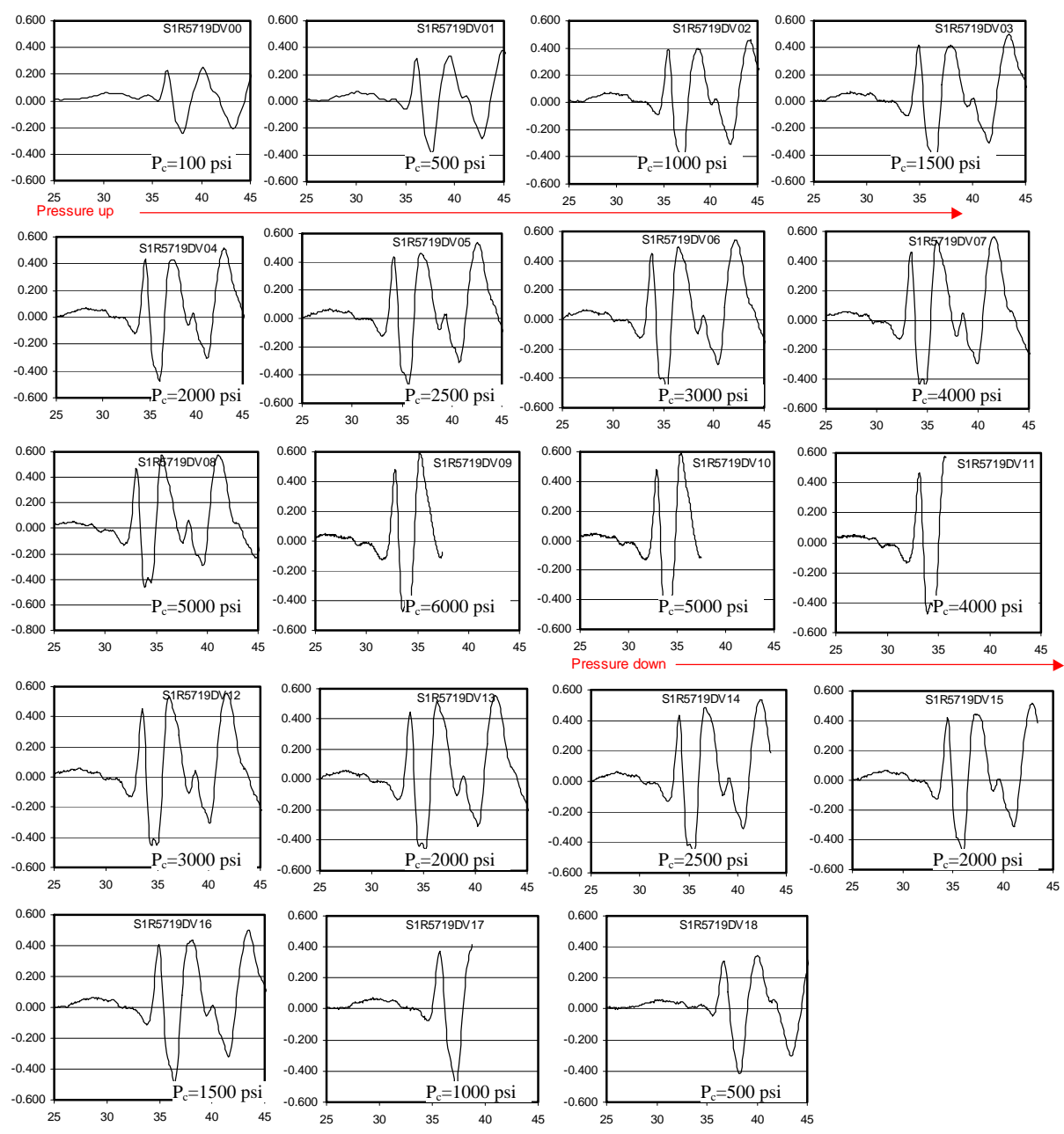


Figure 2-22 S-wave signal through sample R-5719V at different confining pressures.

P- and S-wave velocities were measured in dry tight sandstones at differential pressure between 100 to 6000 psi. Due to the large compressibility of gas, the in-situ velocity in a gas-saturated rock is very close to that in an air-filled rock at the same differential pressure. For tight gas sandstone reservoirs dry measurements give us a close result to the expected response of a methane-saturated tight sandstone.

Dry rock measurements are much simpler and quicker to perform than saturated rock measurements. Differential pressure, P_d , is the difference between confining pressure, P_c , and pore pressure, P_p , (Equation 2-21). The pore pressure is zero (atmospheric pressure), so the confining pressure is equal to the differential pressure (Equation 2-22).

$$P_d = P_c - P_p \quad (2-21)$$

$$P_p = 0 \rightarrow P_d = P_c \quad (2-22)$$

From first arrivals interpretation from P- and S-wave propagation, V_p and V_s are calculated at different differential pressures. From measurements of V_p and V_s for a range of differential pressures, the dependence of dry bulk modulus, K_{DRY} on differential pressure can be obtained (Equation 2-23).

$$K = \rho(V_p^2 - \frac{4}{3}V_s^2) \quad (2-23)$$

The variation of dry rock Lamé's parameters (λ_{DRY} and μ_{DRY}), can be calculating from the velocities (V_p and V_s) measured while changing pressures (Equation 2-24 and Equation 2-25).

$$\lambda = \rho(V_p^2 - 2V_s^2) \quad (2-24)$$

$$\mu = \rho V_s^2 \quad (2-25)$$

From measurements of V_p and V_s for a range of differential pressures, the dependence of P- and S-impedance on differential pressure can be obtained (Equation 2-26 and Equation 2-27).

$$I_p = \rho V_p \quad (2-26)$$

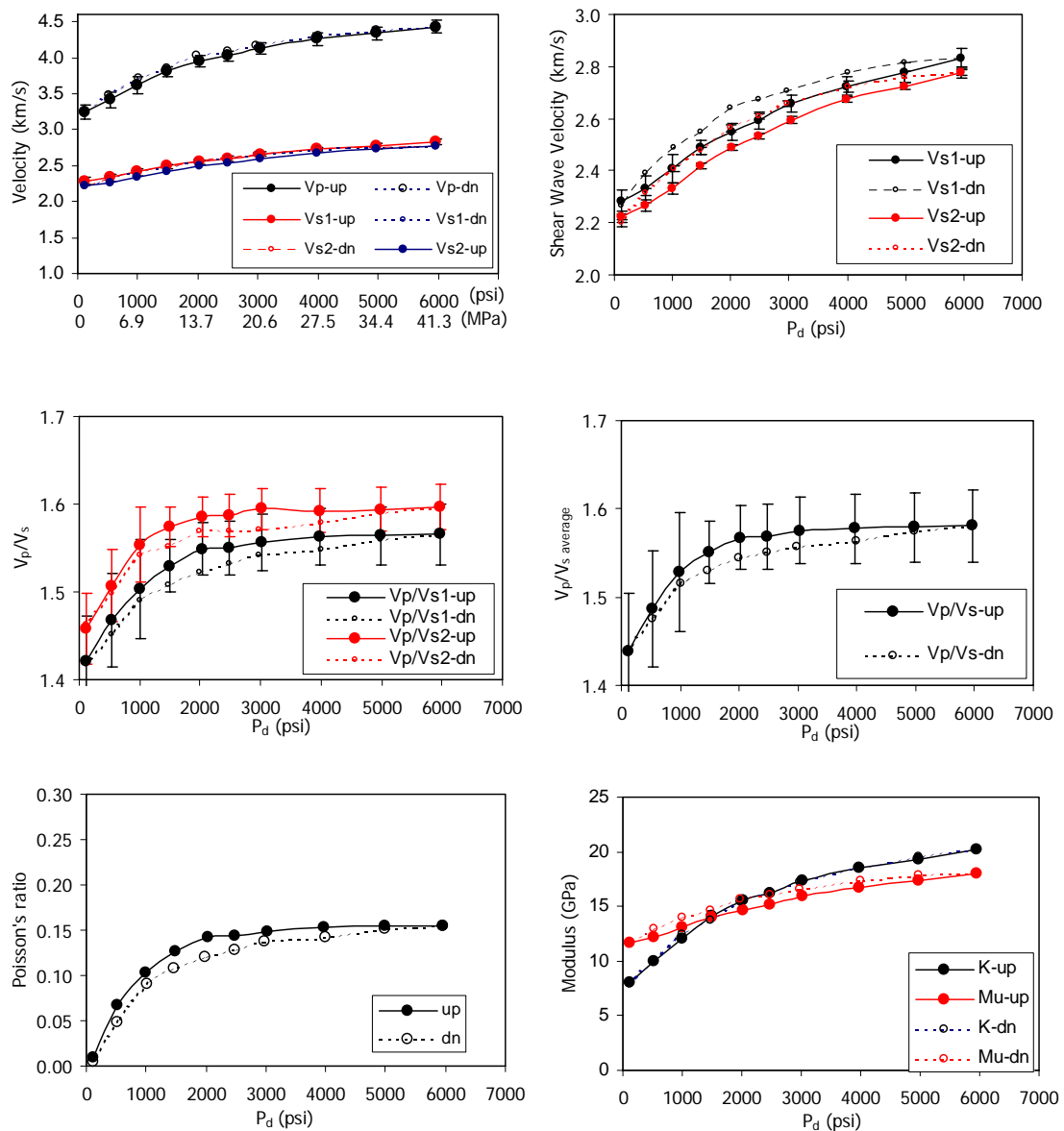
$$I_s = \rho V_s \quad (2-27)$$

Williams Fork Formation

Two samples from the Williams Fork Formation were tested. They are described in Table 2-7. Figure 2-23 and Figure 2-24 shows the effect of differential pressure on elastic properties of sample R-5719V. Also crossplots of elastic properties for sample R-5719V are shown Figure 2-25.

Sample	Fractional Porosity	Permeability (mD)	Grain Density (g/cm ³)	Dry Density (g/cm ³)
R-5719V	0.100	0.042	2.62	2.350
R-5727.1V	0.077	0.006	2.65	2.358

Table 2-7 Description of Williams Fork Formation samples.

Figure 2-23 Effect of differential pressure on elastic properties of sample R-5719V ($\phi=10\%$ and $k=0.042$ mD).

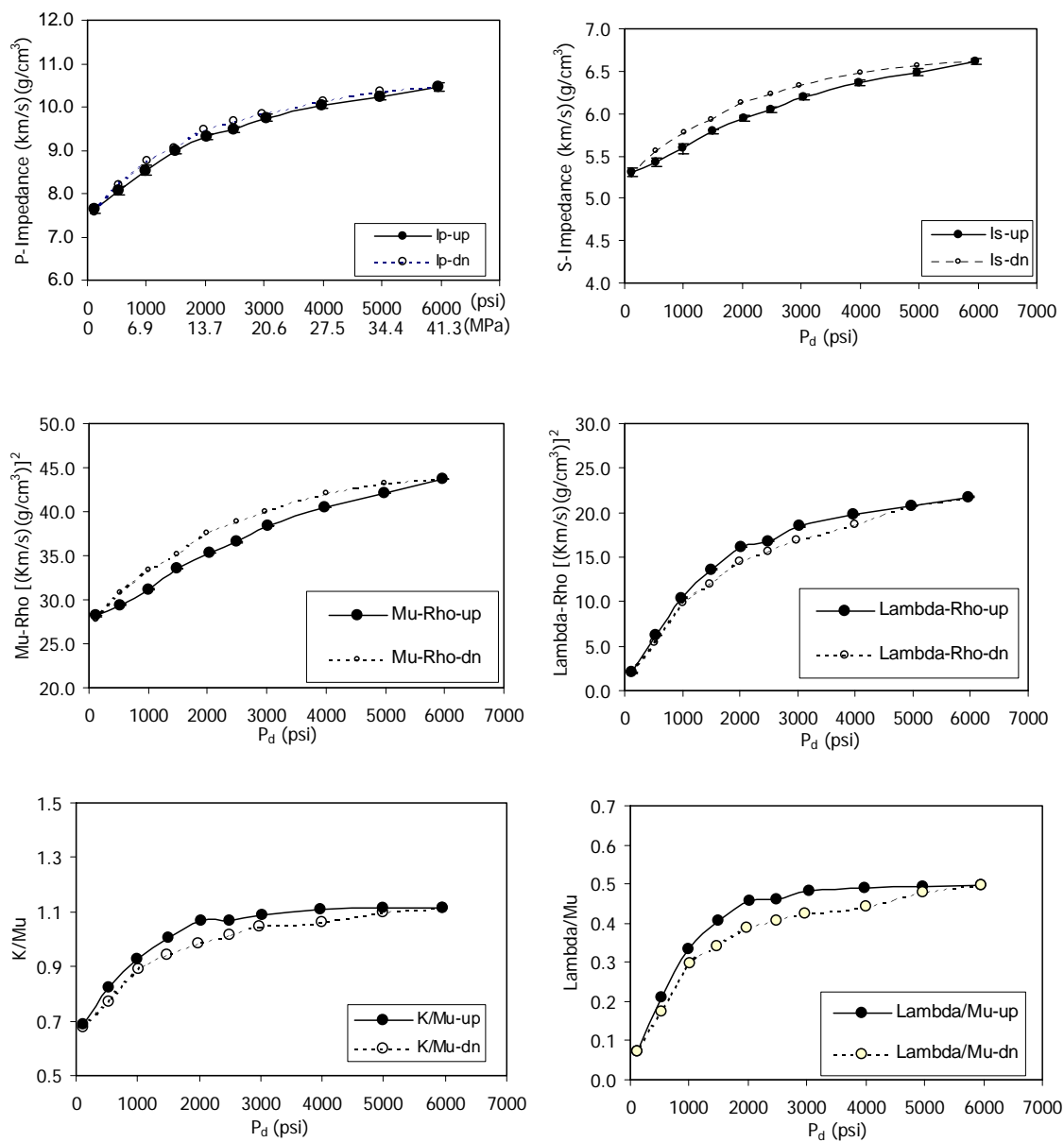


Figure 2-24 Effect of differential pressure on elastic properties and elastic ratios on sample R-5719V.

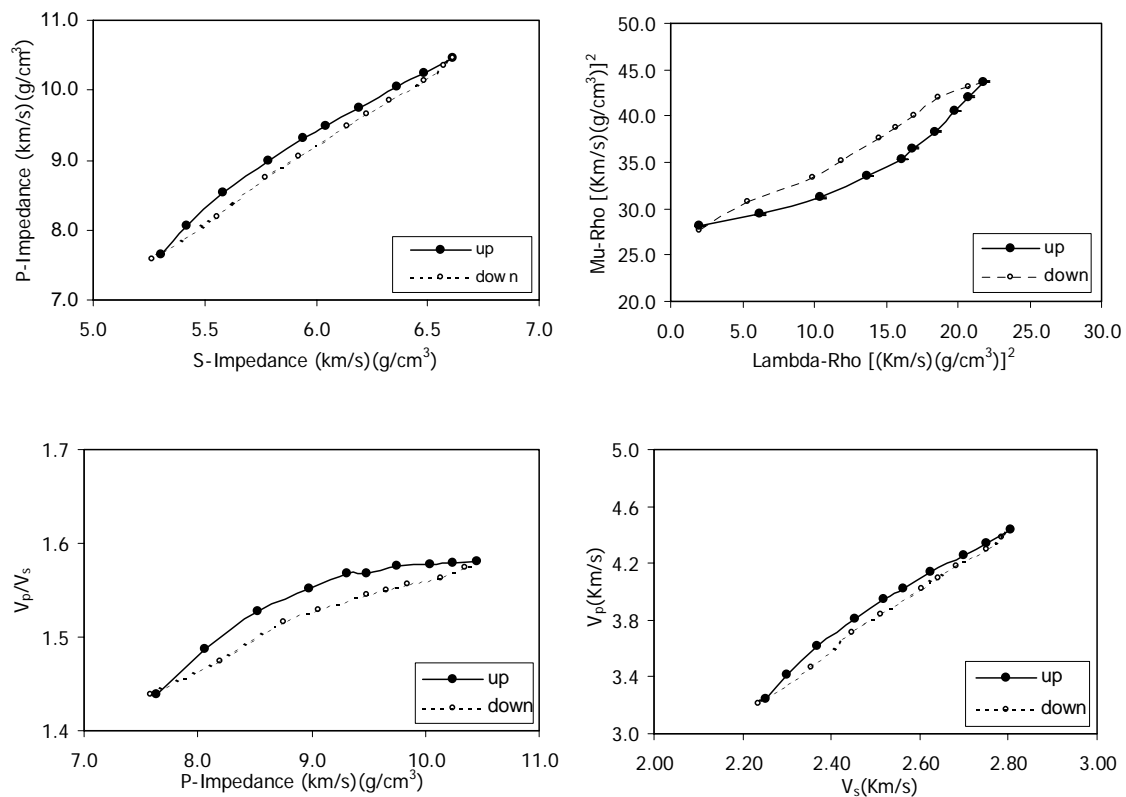


Figure 2-25 Crossplot of elastic properties of sample R-5719V at increasing (up) and decreasing (down) pressures.

Ultrasonic measurements were performed on sample R-5727.1V and results are shown in Figure 2-26, 2-27 and 2-28. All figures show the effect of differential pressure on elastic properties of sample R-5727.1V.

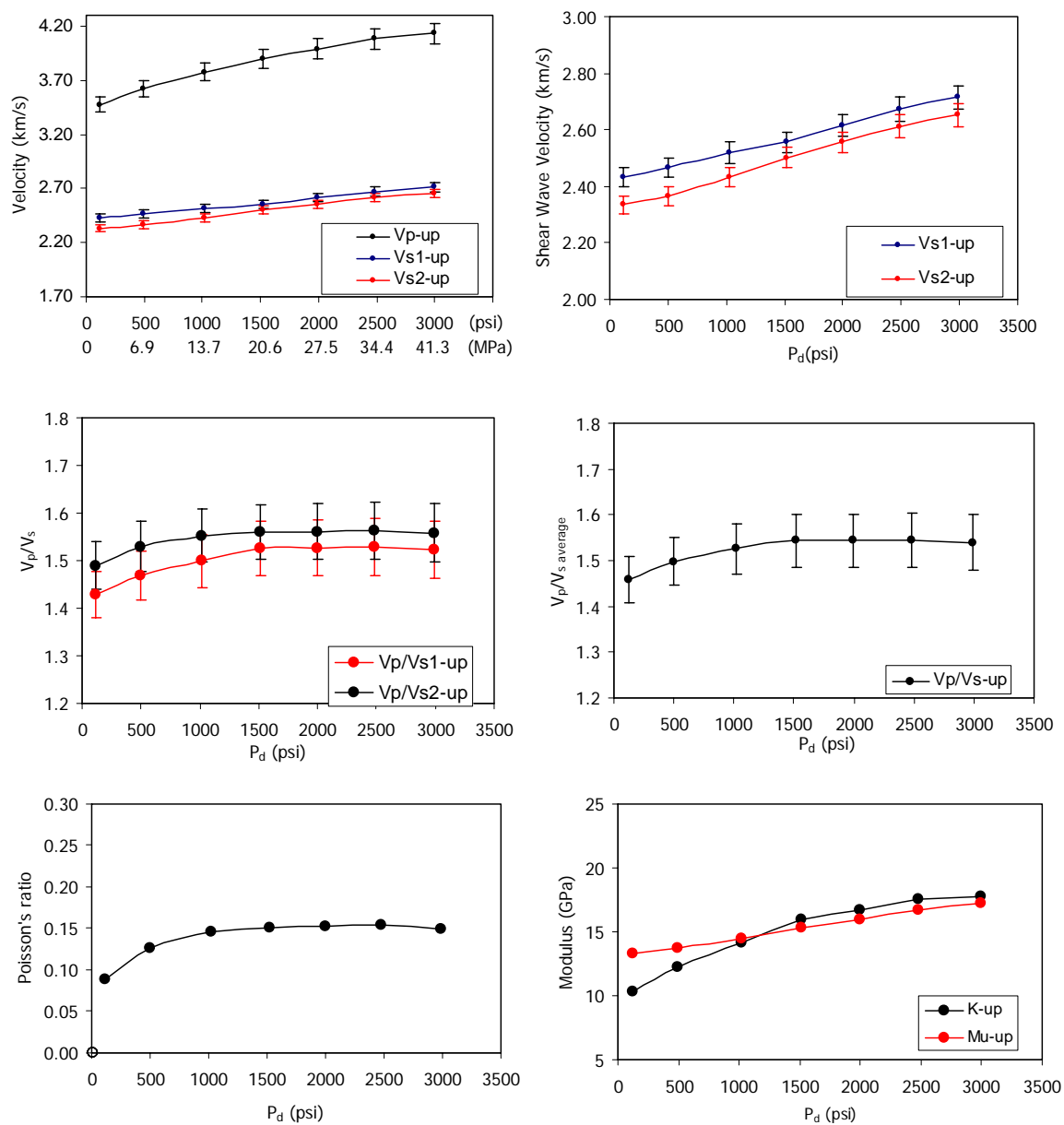


Figure 2-26 Effect of differential pressure on elastic properties of sample R-5727.1V ($\phi=7.74\%$, $k=0.006\text{mD}$).

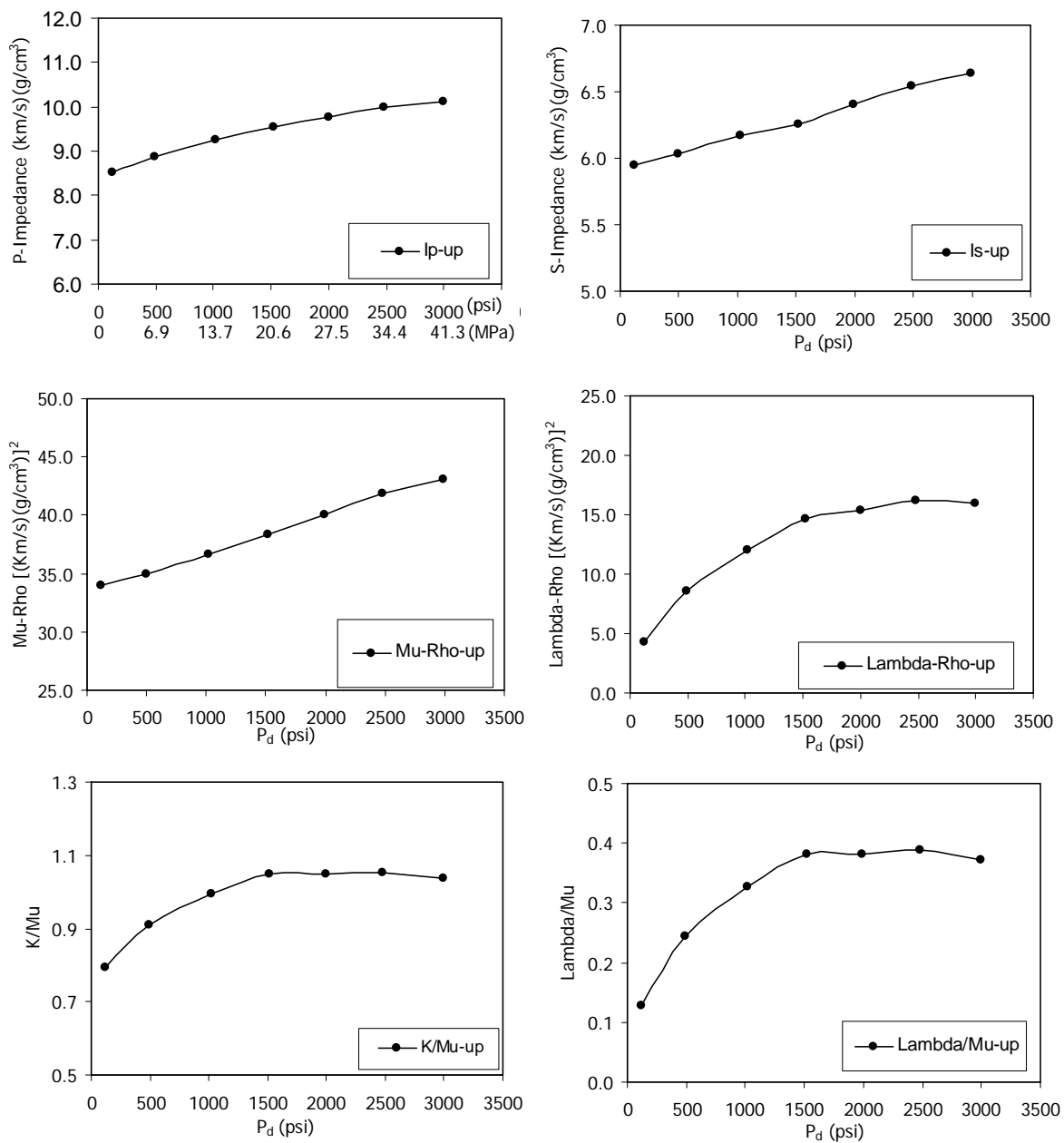


Figure 2-27 Effect of differential pressure on elastic properties and elastic ratios on sample R-5727.1V

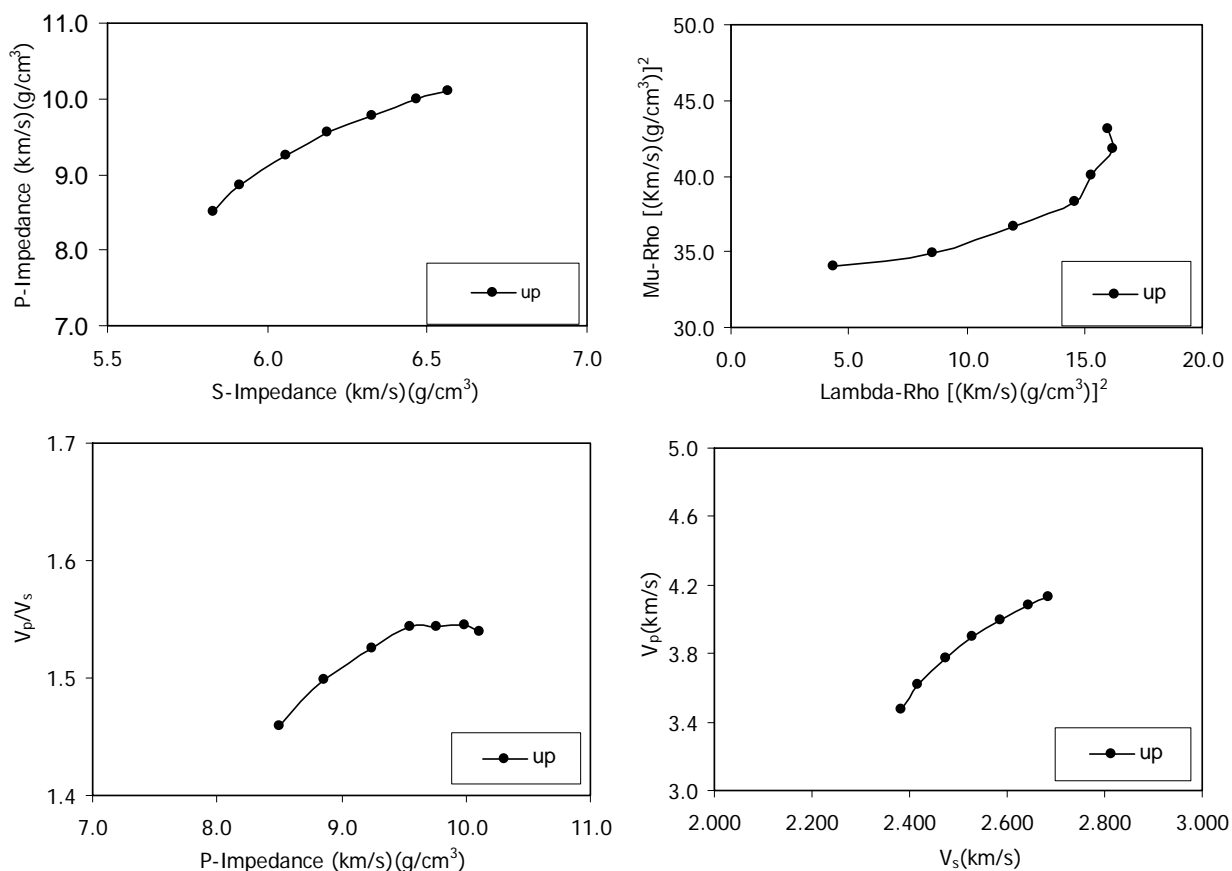


Figure 2-28 Crossplot of elastic properties of sample R-5727.1V at increasing (up) differential pressures.

2.4.3 Discussion of results

The effect of pressure on the elastic properties of tight gas sandstones is defined from the dry measurements. A decrease on elastic properties (V_p , V_s , I_p , I_s , K , μ) is observed when decreasing differential pressure. Due to the large compressibility of gas, the in-situ velocity in a gas-saturated rock is very close to that in an air-filled rock (dry measurements) at the same differential pressure. For tight gas sandstone reservoirs dry

measurements give us a close result to the expected response of a methane-saturated tight sandstone.

The dry rock moduli are used in isotropic numerical modeling (Chapter 3), and the effects of fluids will be modeled and compare with the dry measurements.

2.4.4 Assumption of experimental work

Laboratory velocity measurements conducted under isotropic state of stress can be used to predict velocity at in-situ conditions where, in general, there stress is not isotropic. This assumption is used since there is a lot of uncertainty in the horizontal stress in the reservoir. The results shown have limitations if the in-situ state of stress deviates from an isotropic system.

Chapter 3

ISOTROPIC NUMERICAL MODELING OF ELASTIC ROCK PROPERTIES

3.1 Introduction

Numerical modeling is used to understand and relate changes in seismic response to changes in reservoir fluid saturation and pressure. The isotropic modeling is done based on ultrasonic core data (Chapter 2). Gassmann's fluid substitution theory (Gassmann, 1951) is used for isotropic rock models. The results of the isotropic modeling can be used and compared with more detailed anisotropic rock models.

3.2 Gassmann's fluid substitution

P- and S-wave velocities were measured in dry tight sandstones at differential pressure between 100 to 6000 psi (Chapter 2). Velocities at in-situ saturation conditions were calculated from the dry-rock velocity using Gassmann's fluid substitution equations. Due to the large compressibility of gas, the in-situ velocity in a gas-saturated rock is very close to that in an air-filled rock at the same differential pressure. Using the measured ultrasonic data, I calculated velocities at in-situ conditions, and I analyzed the V_p/V_s behavior under different pressure conditions.

Gassmann's equations are commonly used to predict velocity changes due to different pore-fluid saturations. In seismic reservoir characterization studies it is critical to understand how pore fluids affect seismic velocities. In both direct hydrocarbon indicator (DHI) analysis and seismic monitoring, it is important to quantify the effects of pore-fluids on elastic properties (impedances, velocities, V_p/V_s , etc.). In this study the efforts are concentrated in understand those effects on V_p/V_s . The effects of pore fluids and pore pressures can be studied in two ways: direct measurements (e.g., laboratory tests) and numerical modeling (e.g., Gassmann's equations).

Gassmann's equation requires input parameters that are measured directly in the laboratory (e.g., K_{DRY} , ϕ). Here, Gassmann's formulation is presented in a way that has clear physical meaning (Han and Batzle, 2004),

$$K_{SAT} = K_{DRY} + \Delta K_{DRY} \quad (3-1)$$

$$\Delta K_{DRY} = \frac{K_M (1 - K_{DRY} / K_M)^2}{1 - \phi - K_{DRY} / K_M + \phi \times K_M / K_{FL}} \quad (3-2)$$

$$\mu_{SAT} = \mu_{DRY} \quad (3-3)$$

where, K_M , K_{FL} , K_{DRY} , K_{SAT} , are the bulk moduli of the mineral grain, fluid, dry rock, and saturated rock frame, respectively; ϕ is porosity, and μ_{SAT} and μ_{DRY} are the saturated and dry-rock shear moduli. K_{DRY} is an increment of bulk modulus as a result of fluid

saturation of dry rock. The shear modulus of the rock is not affected by fluid saturation. Numerous assumptions are involved in Gassmann's equations. The rock-fluid system is so complicated that in order to simplify the mathematics major assumptions are necessary. Before applying Gassmann's equation, it is very important to understand the assumptions and limitations of the model. Many of the assumptions may not be valid for tight gas sandstone reservoirs, however due to the simplicity and available input data, Gassmann's fluid substitution is a very good initial approach before going into more complex models.

The basic assumptions in the Gassmann's equation for a porous system are:

1. the rock or porous system is homogenous and isotropic,
2. the pores should be in flow communication, well connected and in pressure equilibrium (low frequency limit),
3. there are no chemical reactions between fluids and rock frame,
4. the rock-fluid system is closed (undrained), and
5. the pores are filled with frictionless fluid.

In hydrocarbon reservoirs, many of these assumptions may not be valid. For example, fractured reservoirs with high anisotropy rocks will violate assumption 1. Most of the assumptions are difficult to honor in very complex reservoirs where there are low permeability and porosity rocks, hydrocarbons with high viscosity, fluids chemically interacting with rocks, etc. However, Gassmann's equation is commonly used for initial

modeling of the matrix properties, and the results can be used as inputs for more complex modeling, for example, anisotropy rock physics models.

Laboratory measurements are necessary to obtain input parameters for rock physics models of hydrocarbon reservoir systems. This is the first time that dry measurements are conducted in Rulison Field tight gas sandstones. The information obtain in the laboratory is used for Gassmann's numerical modeling and results are used as an initial approach, to quantify pore pressure and fluid-saturation effects on elastic rock properties. The Gassmann's approach will provide an estimate of relaxed velocity at zero frequency, which is a lower bound of the fluid–saturation effect.

In this study, velocities at in-situ saturation conditions were calculated from the dry-rock velocity using Gassmann's fluid substitution equations. Due to the large compressibility of gas, the in-situ velocity in a gas-saturated rock is very close to that in an air-filled rock at the same differential pressure. Using the measured ultrasonic data, velocities at in-situ conditions were estimated, and the V_p/V_s behavior under different pore-pressure and pore-fluid saturation conditions was studied.

3.2.1 Input variables for Gassmann's equation

Here, I show, a brief explanation of the way the input variables for Gassmann's equation were calculated for this study.

3.2.1.1 Mineral modulus, K_M and μ_M

Different minerals compose rocks. In this study the information about mineralogy was obtained using XRD methodology. Table 2-4 and Table 2-5 show the mineral composition of four core samples used in this study. The Reuss-Voight-Hill average (Hill, 1952) was used to calculate the grain (matrix) bulk and shear moduli (Equation 3-4).

$$M = \frac{1}{2}(M_V + M_R) \quad (3-4)$$

where M is the effective grain modulus that can be either K_M or μ_M and M_V is the Voight average (isostrain behavior),

$$M_V = \sum_{i=1}^n c_i M_i \quad (3-5)$$

and M_R is the Reuss average (isostress behavior),

$$\frac{1}{M_R} = \sum_{i=1}^n \frac{c_i}{M_i} \quad (3-6)$$

c_i and M_i are the volume fraction and the modulus of the i th component, respectively. Wang (2000) shows that the Voight-Reuss-Hill model works quite satisfactorily for solid rocks composed of various minerals when the elastic properties of the minerals are within

a relatively narrow range. This model is very useful when mineralogical data are available. In order to calculate, the Voigt-Reuss-Hill average to obtain K_m necessary for Gassmann's fluid substitution, mineralogical data and elastic properties of minerals (Wang, 2000) were used.

In this study, the mineral elastic moduli for each sample were calculated: (1) using the exact mineralogical composition reported in the XRD study, (2) using the mineralogical composition and using averaged-clay elastic modulus, and (3) assuming the rock is 100% quartz. Considering these different cases, the Gassmann's fluid substitution was calculated and a sensitivity analysis was conducted for the mineral bulk modulus. Table 3-1 shows the Hill-Voigt-Reuss calculated with mineralogical information available of sample R-5719V. The mineral moduli were obtained from Wang (2000). Table 3-2 shows the Hill-Voigt-Reuss calculated with mineralogical information available of sample R-5719V, and averaged-clay elastic modulus. Table 3-3 shows the values used for the case of assuming the rock 100% Quartz.

3.2.1.2 Fluid modulus, K_f

At Rulison Field, the fluids in the Williams Fork Formation are brine and a light gas, mostly methane. The chemical composition of Rulison Field gas was obtained from the MWX-site (Table 3-4). Pore pressure gradient data are available for the MWX-site (Figure 1-5, Chapter 1). The pressure gradient information show that the pore pressures vary from approximately 2250 to 4420 psi (15 to 30 MPa). High pressures occur at the

Williams Fork Formation, but pressure should decrease near areas already depleted (primary depletion production process).

Mineral	Volume Fraction	K_M (Wang, 2000)	μ_M (Wang, 2000)
Quartz	0.66	38.00	44.40
Plagioclase	0.20	75.60	25.60
Calcite	0.005	76.70	32.30
Mixed-Layer Illite-Smectite	0.025	35.70	17.80
Illite-Mica	0.099	57.20	28.65
Kaolinite	0.004	46.01	23.89
Chlorite	0.016	165.02	52.10
Voigt bound		49.96	38.79
Reuss bound		44.06	35.50
Hill average		47.01	37.15

Table 3-1 Effective K_M and μ_M using Hill-Voight-Reuss average and mineralogical composition of sample R-5719V.

Mineral	Volume Fraction	K_M (Wang, 2000)	μ_M (Wang, 2000)
Quartz	0.66	38.00	44.40
Plagioclase	0.20	75.60	25.60
Calcite	0.005	76.70	32.30
Clay-average	0.140	35.00	12.50
Voigt bound		45.48	36.33
Reuss bound		41.52	29.38
Hill average		43.50	32.85

Table 3-2 Effective K_M and μ_M using Hill-Voight-Reuss average, mineralogical composition of sample R-5719V, and using averaged elastic modulus for clays.

Mineral	Volume Fraction	K_M (Wang, 2000)	μ_M (Wang, 2000)
Quartz	1.00	38.00	44.40

Table 3-3 Effective K_M and μ_M assuming sample R-5719V is 100% Quartz.

Well Name	Depth of Sample(ft)	N ₂ and (or) air (vol.%)	CH ₄ (vol. %)	CO ₂ (vol. %)	C ₂ H ₆ (vol. %)	C ₃ H ₈ (vol. %)	i-C ₄ H ₁₀ (vol. %)	n-C ₄ H ₁₀ (vol. %)	C ₁ /C ₁₋₅ (vol. %)
MWX-1	5885	8.93	84.25	0.01	5.08	1.19	0.32	0.21	0.925

Table 3-4 Results of compositional and isotopic analysis of gases at Rulsion Field, MWX-1 well (Johnson and Rice, 1990)

Figure 1-5 (Chapter 1) shows the pore pressure gradients measured from well tests in the U.S. DOE's Multiwell Experiment (MWX) site at Rulsion field (Spencer, 1989). Down to 5200 ft the pore pressure gradient is 0.433 psi/ft, leading to a pore pressure of approximately 2250 psi. In the zone of interest, (5000-6500 ft) the pore pressure gradient increases with depth up to 0.68 psi/ft at 6500 ft, leading to a pore pressure of 4420 psi at a depth of 6500 ft. In general, pore pressure increases with depth to progressively larger overpressure gradients. Pore pressure decreases during primary depletion. However, due to high reservoir heterogeneity, production wells drain only small areas and possibly leaving overpressured zones in undrained areas.

Brine is another important fluid at Rulsion Field. According to Cumella and Otsby (2003), gas associated with overpressuring are trapped in discontinuous fluvial sandstones with high irreducible water saturations (40-65%). According to Williams Oil Company (personal communication with Lesley Evans), the Williams Fork Formation water has a salinity of 25,000 ppm. Brine is the simplest fluid to model since it only depends on salinity. The bulk modulus of brine was modeled using the Fluid Acoustics for Geophysics (FLAG 4) program, this tool was developed in the Fluids Project at the Colorado School of Mines and Houston Advanced Research Center, the program models

the bulk modulus and density of fluids (brine, gas, oil) as a function of salinity, temperature and pressure. The FLAG equations for the acoustic properties of fluids are described by Batzle and Wang (1992). Brine is the most dense and least compressible fluid in Rulison Field. Figure 3-1 shows the bulk modulus of brine as a function of pressure for a salinity of 25,000 ppm NaCl at 80°C. Figure 3-2 shows the density of brine as a function of pressure for a salinity of 25,000 ppm NaCl at 80°C.

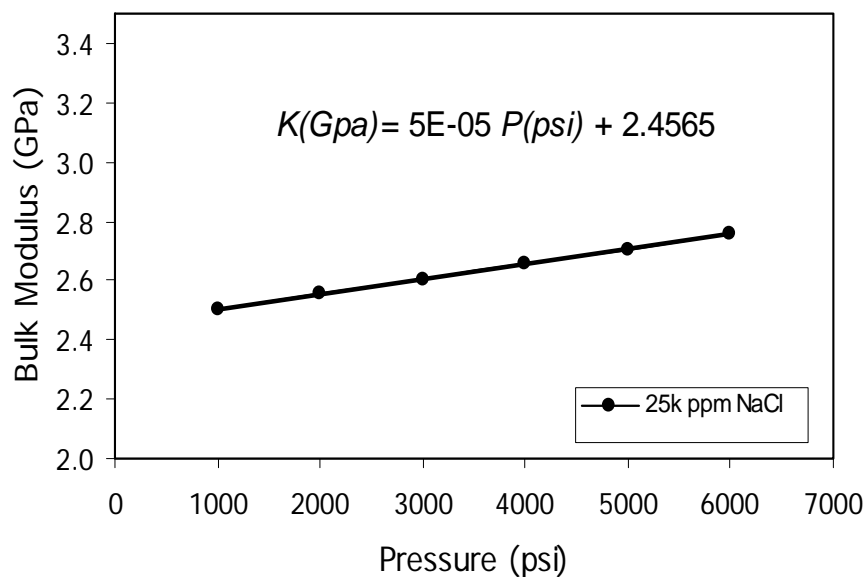


Figure 3-1 Bulk modulus of brine as a function of pore pressure, at reservoir temperature (80°C) and salinity (25,000 ppm NaCl) [FLAG 4].

Rulison gas is a light gas, mainly a mixture of methane, ethane and nitrogen. Acoustic properties were calculated using FLAG 4 for different cases: (1) Rulison Field mixture of gases, and (2) 100 % methane. For simplicity, Rulison Field composition was assumed to be 85% methane, 10% nitrogen, and 5 % ethane (based on Table 3-4).

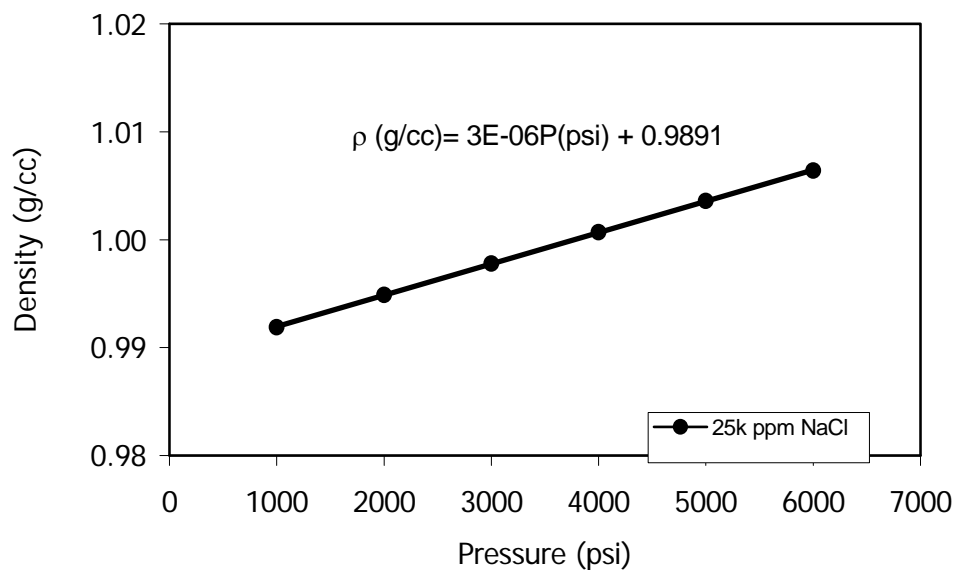


Figure 3-2 Density of brine as a function of pore pressure, at reservoir temperature (80°C) and salinity (25,000 ppm NaCl) [FLAG 4].

Figure 3-3 shows the bulk modulus of Rulison gas (mixture of gases) and 100% methane as a function of pressure at 80°C. Figure 3-4 shows the density of Rulison gas (mixture of gases) and 100% methane as a function of pressure at 80°C.

The bulk modulus and density relations for brine and Rulison Field gas under expected pressure and temperature conditions are successfully modeled. The acoustic properties of these fluids are used for fluid substitutions to determine the fluid effects on seismic properties of the reservoir.

In a reservoir system, to be realistic, we cannot consider one single fluid compound. At Rulison Field, we have a mixture of gas and irreducible water with salinity

of 25,000 ppm NaCl. In low permeability reservoirs, specifically at Rulison field, the irreducible water saturation tends to be high, 45 to 65% (Cumella, and Ostby, 2003).

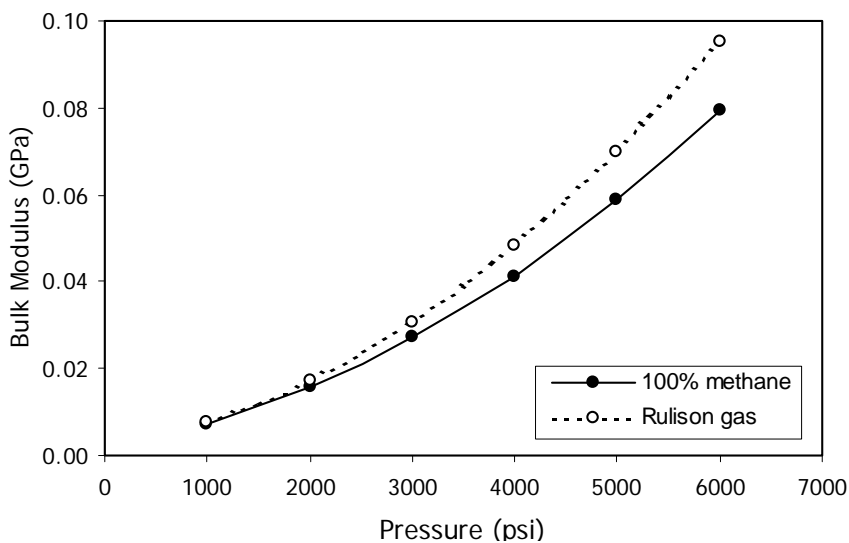


Figure 3-3 Bulk modulus of Rulison gas (85% methane, 10% nitrogen, and 5% ethane) and 100% methane as a function of pore pressure at reservoir temperature (80°C) [FLAG 4].

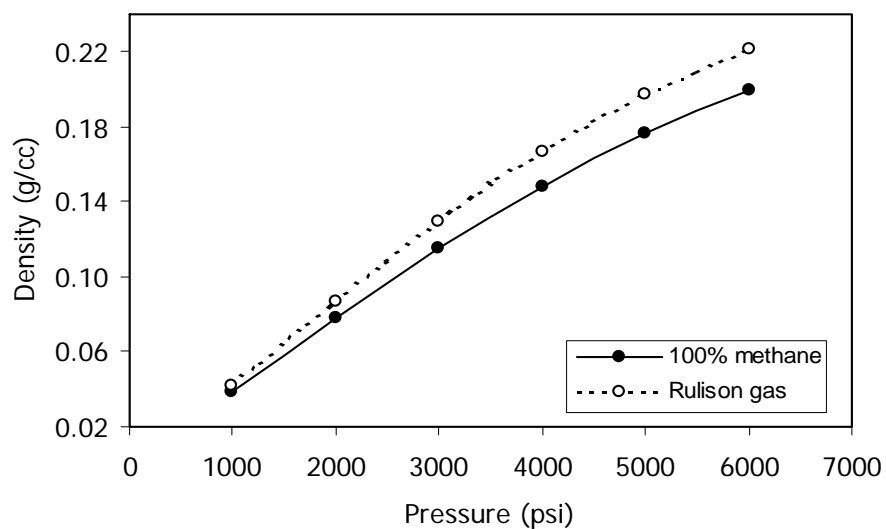


Figure 3-4 Density of Rulison gas (85% methane, 10% nitrogen, and 5% ethane) and 100% methane as a function of pore pressure at reservoir temperature (80°C) [FLAG 4].

Knowing the modulus of the brine and gas at Rulison Field at different pressures and at reservoir temperature, we can calculate the modulus of the mixture using Wood's equation. For the case of two compounds (brine and gas) with known properties, K_w and K_g , respectively, and saturation $S_g=1-S_w$, the modulus of the mixture or effective bulk modulus, K_{EFF} can be calculated as:

$$\frac{1}{K_{EFF}} = \frac{S_w}{K_w} + \frac{1-S_w}{K_g} \quad (3-7)$$

where K_w and S_w are the bulk modulus and saturation of the water or brine, K_g and S_g are the bulk moduli and saturation of the gas, and K_{EFF} is the effective bulk modulus.

$$\rho = c_{gas}\rho_{gas} + c_w\rho_w \quad (3-8)$$

where c_w and ρ_w are the volume fraction and density of the water or brine, and c_{gas} and ρ_{gas} are the volume fraction and density of the gas.

The effective fluid density and bulk modulus can be modeled for the Williams Fork Formation. Since this Williams Fork Formation is highly heterogeneous, we will calculate the acoustic properties of the mixture for different saturation and pressure scenarios. The results of this modeling can be used as input parameters for Gassmann's fluid substitution. Figure 3-5 shows the comparison of the bulk moduli of different fluid composition scenarios possible in the reservoir in terms of gas saturation and pore

pressure. I also show the upper and lower bound of the fluid bulk modulus for Rulison Field. In this case the upper bound will be the bulk modulus for 100% brine, and the lower bound will be the bulk modulus for 100% gas.

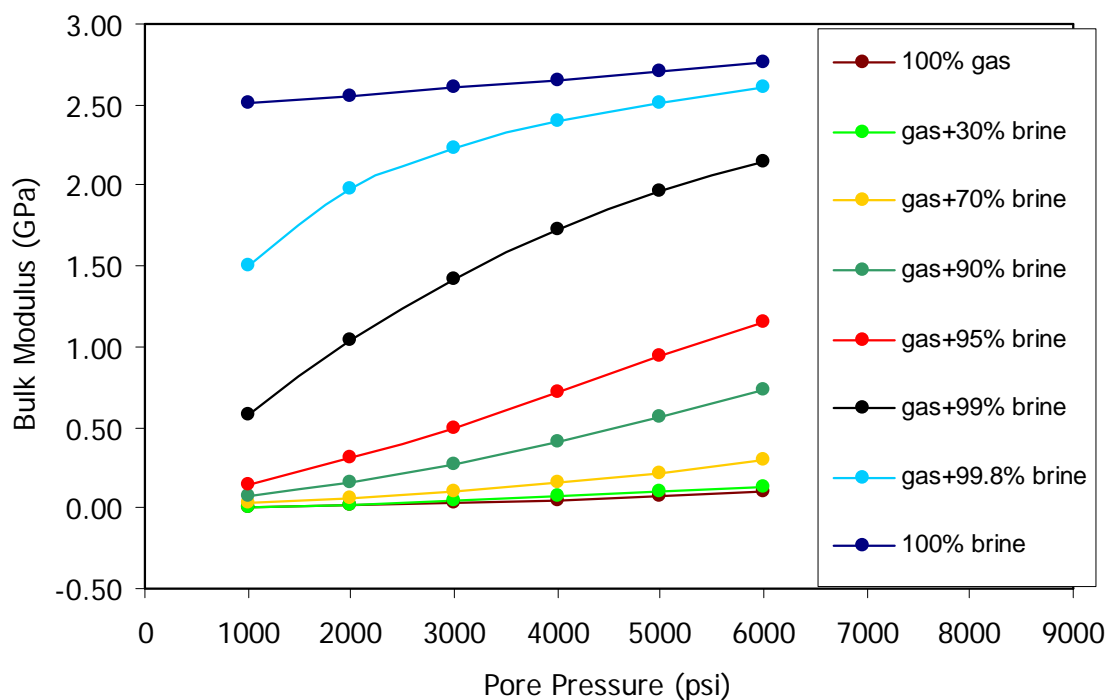


Figure 3-5 Bulk modulus of reservoir fluids as a function of pore pressure and saturations ($T=80^{\circ}\text{C}$).

Figure 3-6 shows the comparison of the density of different fluid scenarios in the reservoir in terms of gas saturation and pore pressure. The Williams Fork Formation contains high irreducible or residual brine saturation (40-65%). I also show the upper and lower bound of the fluid density for Rulison Field. In this case the upper bound will be the density for 100% brine, and the lower bound will be the density for 100% gas.

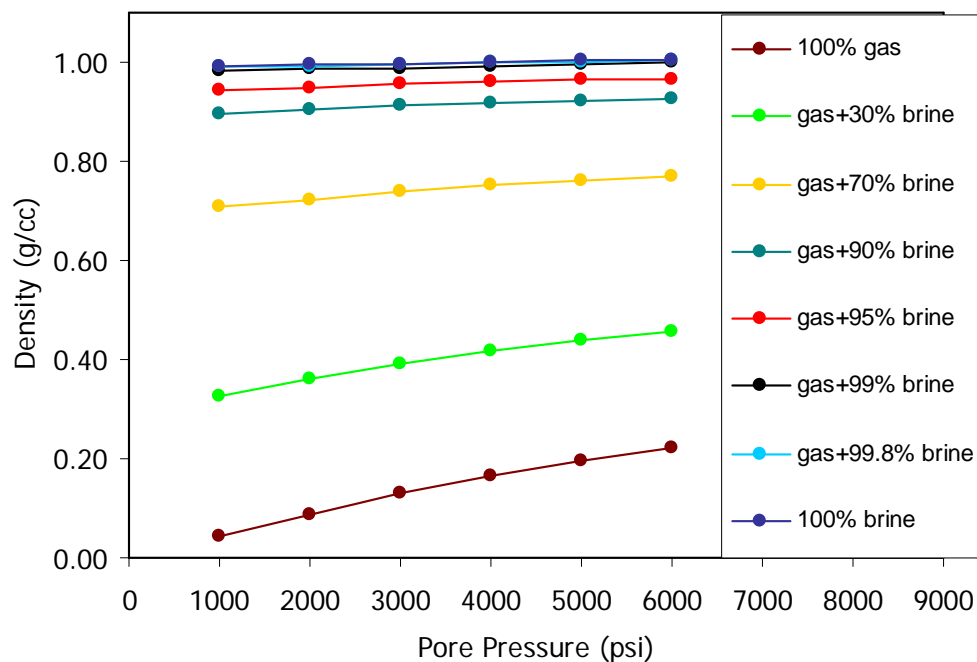


Figure 3-6 Density of reservoir fluids as a function of pore pressure and saturations (T=80°C).

Figure 3-5 shows how the bulk modulus change dramatically when adding to the fluid composition less than 1% gas. In the Rulison Field case, brine saturations (irreducible water) are between 45 and 65%, at these saturation conditions the bulk modulus is almost constant. Therefore, the fluid saturation is expected to play little or no role in the change in the seismic response. From Figure 3-6 it is possible to observe that the density changes are directly proportional to gas saturation changes.

3.2.1.3 Dry modulus, K_{DRY}

In this study the dry modulus was calculated from the velocities measured directly in the laboratory.

3.2.1.4 Porosity, ϕ

The porosity was measured in the laboratory using Archimedes's principle.

3.2.2 Results of Gassmann's fluid substitution

After obtaining each of the variables necessary for Gassmann's equations, different scenarios (pressures and saturations) were numerically modeled. The examples shown here correspond to sample R-5719V ($\phi=10\%$, $k=0.042\text{mD}$).

Figure 3-7 shows P-wave velocity variations due to differential pressure changes. The fluid substitution was done for three cases: (1) assuming the sample 100% quartz (black dots), (2) assuming an average clay bulk (Wang, 2000) modulus for the 14 % of phyllosilicates present in the sample (open symbols), and (3) using detail mineralogical information from XRD study and values of mineral bulk modulus reported by Wang (2000).

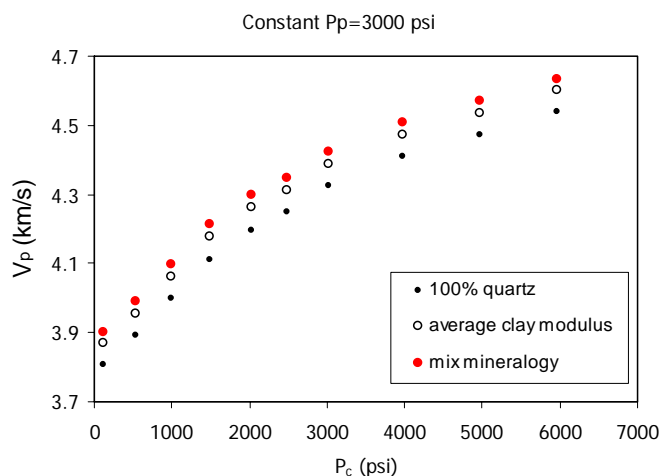


Figure 3-7 P-wave velocity versus confining pressure after Gassmann's fluid substitution at constant pore pressure ($P_p=3000$ psi) on sample R-5719V using different mineral bulk modulus.

Figure 3-7 shows that the changes in velocity due to assuming different mineral bulk modulus (three cases presented in this study) as an input for Gassmann's equation is less than 100 m/s or 2.3%.

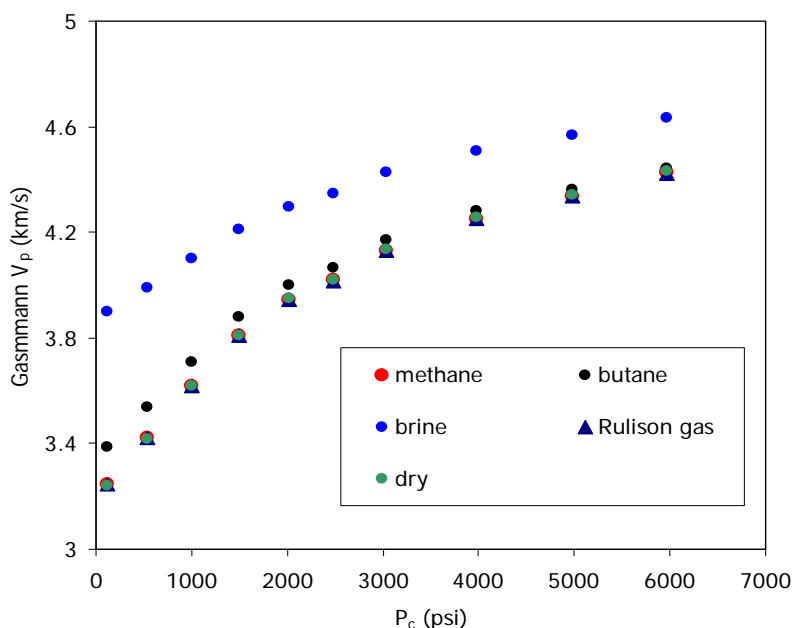


Figure 3-8 P-wave velocity versus confining pressure after Gassmann's fluid substitution at a constant pore pressure ($P_p=3000$ psi) on sample R-5719V using different fluids.

Figure 3-8 shows that velocity at in-situ saturation conditions (Rulison field gas, represented by blue triangles) is very close to the velocity calculated from dry measurements (air-filled rock) in the laboratory at the same confining pressure. Also the velocity estimation when doing 100% methane saturation or when using the mixture of gases in Rulison (85 % methane, 10 % nitrogen and 5 % ethane) are very close. As expected, considerable changes of velocity are observed when saturating with 100% water compared to 100% gas.

Figure 3-9 shows the s-wave velocity of the rock (sample R-5719V) predicted by Gassmann's equation after fluid substitution with different fluids. Because in Gassmann's theory shear modulus is not affected by fluid saturation, a change is observed due to saturation related with density changes. The S-wave velocities for the brine saturated sample may be slightly lower than the gas and unsaturated case, because of the fluid density effect.

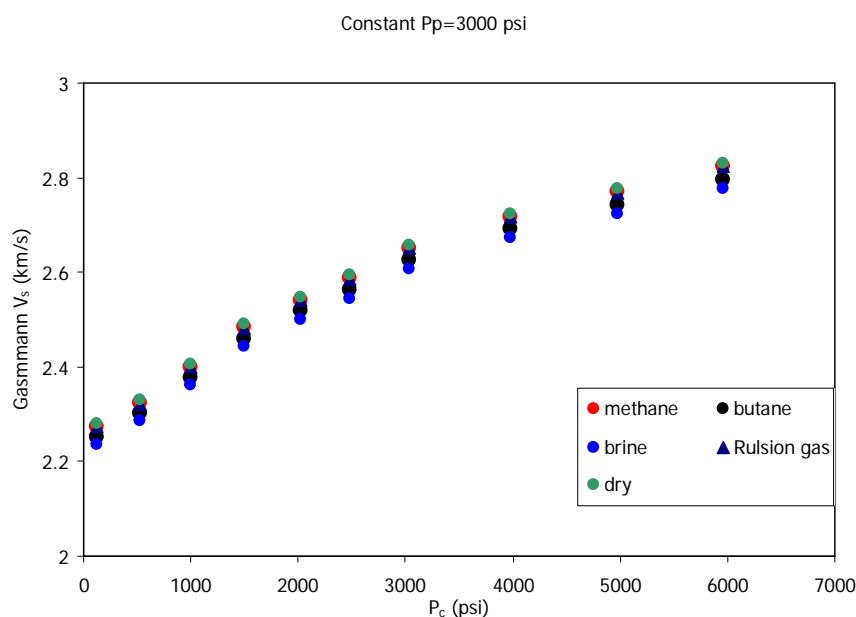


Figure 3-9 S-wave velocity versus confining pressure after Gassmann's fluid substitution at a constant pore pressure ($P_p=3000$ psi) on sample R-5719V using different fluids.

In the reservoir, differential pressure changes due to primary depletion process or due to gas overpressure areas, involve changes in pore pressure at a constant confining pressure. During ultrasonic measurements, confining pressure is held constant. This confining pressure applied to a sample in the laboratory is isotropic. During a primary

depletion process, the vertical confining or overburden stress remains approximately constant, and pore pressure decreases due to gas production. However, due to the high reservoir heterogeneity, production wells drain only small areas leading to overpressured zones in undrained areas.

Figure 3-10 shows P-wave variation with pore pressure for a gas and brine saturated sample after Gassmann's fluid substitution. The data shown in this figure are at a constant confining pressure ($P_c=6000$ psi). The decrease in velocity with increasing pore pressure in both cases (brine and gas) can be observed. At a constant confining and pore pressure the difference in velocity is the fluid effect. In this case, the end members were modeled since the data are at 100% brine and 100% gas saturation.

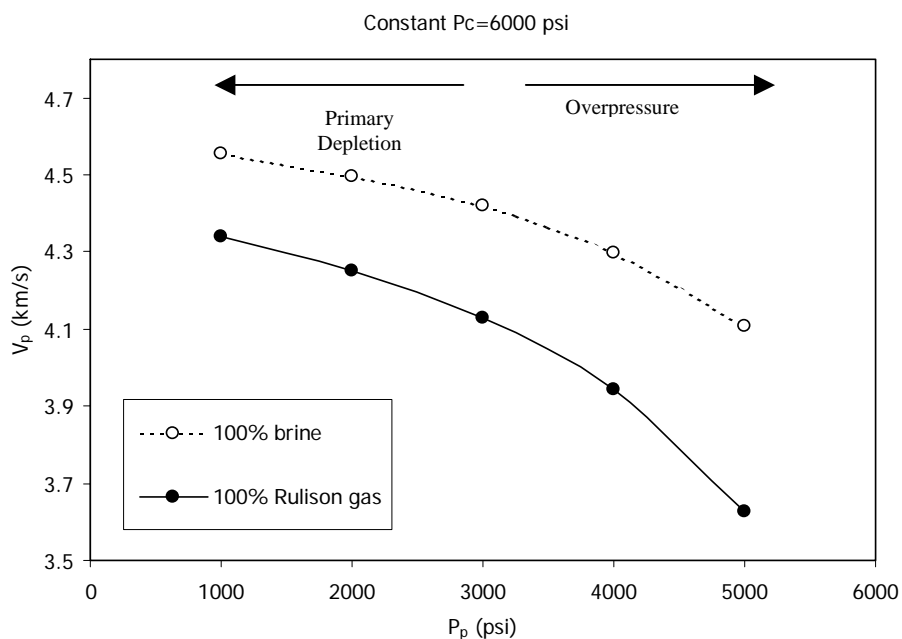


Figure 3-10 P-wave velocity changes with pore pressure and pore fluid (brine and Rulison gas) at a constant confining pressure for sample R-5719V after Gassmann's fluid substitution.

Figure 3-11 shows P-wave variation with differential pressure for a gas and brine saturated sample after Gassmann's fluid substitution. The data shown in this figure are at a constant confining pressure ($P_c=6000$ psi). We can observe the increase in velocity with increasing differential pressure in both cases (brine and gas). At a constant confining and differential pressure the difference in velocity is due to the fluid effect.

At reservoir conditions, rock's velocities react to the differential pressure (confining minus pore). The data collected can be used to predict in-situ velocity variations in rock with gas due to pore pressure changes at a constant confining pressure (overburden). In Figure 3-11 results from dry measurements (air-filled rock) are very close to the results after a fluid substitution with the reservoir gas. Due to the large compressibility of gas, the in-situ velocity in a gas saturated tight sandstone is very close to that in rock with air in the laboratory (dry measurements) at the same differential pressure.

Figure 3-12 shows Gassmann's modeling of more realistic scenarios in a reservoir. Different gas and brine saturation conditions are considered and P-wave velocities are modeled. Figure 3-5 shows the modeling of fluid bulk modulus variation with differential pressure for different fluid saturation scenarios. The results of the modeling show that for low brine saturation the bulk modulus of the fluid is close to the modulus of 100% gas, and this explains the results observed when modeling the velocity changes of the rock with different gas and brine saturation conditions.

Gassmann's equations assume that the pore fluid will not interact chemically with the solid in a way that would influence the elastic properties of the mineral. This assumption leads to $\mu_{sat} = \mu_{dry}$. In other words, all the changes of the porous system occur only for the bulk modulus and density. Figure 3-13 shows S-wave variation with differential pressure for a gas and brine saturated sample after Gassmann's fluid substitution. The data shown in this figure are at a constant confining pressure ($P_c = 6000$ psi). We can observe the increase in velocity with increasing differential pressure in both cases (brine and gas). Shear wave velocity depends on μ and density. At a constant confining and differential pressure the difference in velocity is due to a density effect, since μ will not change in Gassmann's model.

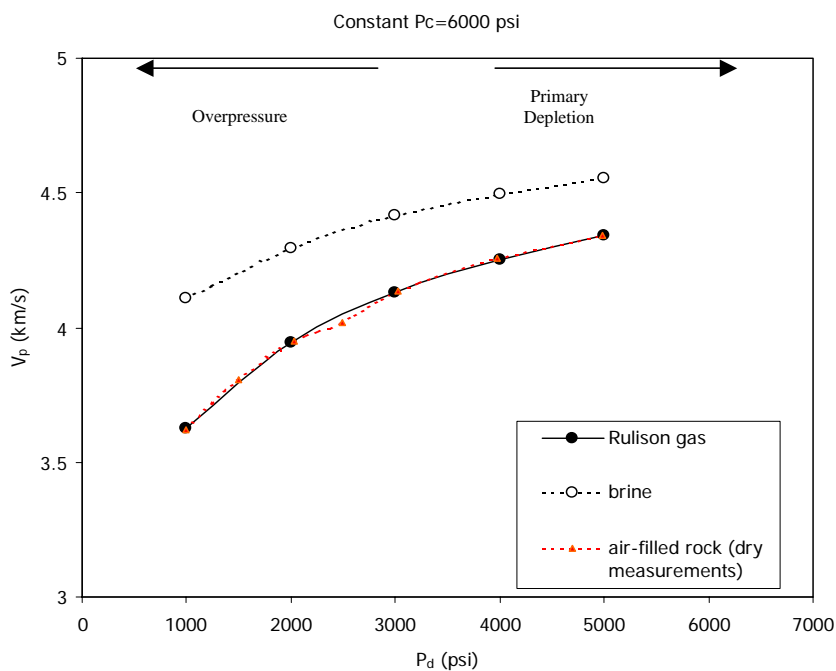


Figure 3-11 P-wave velocity changes with differential pressure and pore fluid (brine and Rulison gas) at a constant confining pressure for sample R-5719V after Gassmann's fluid substitution.

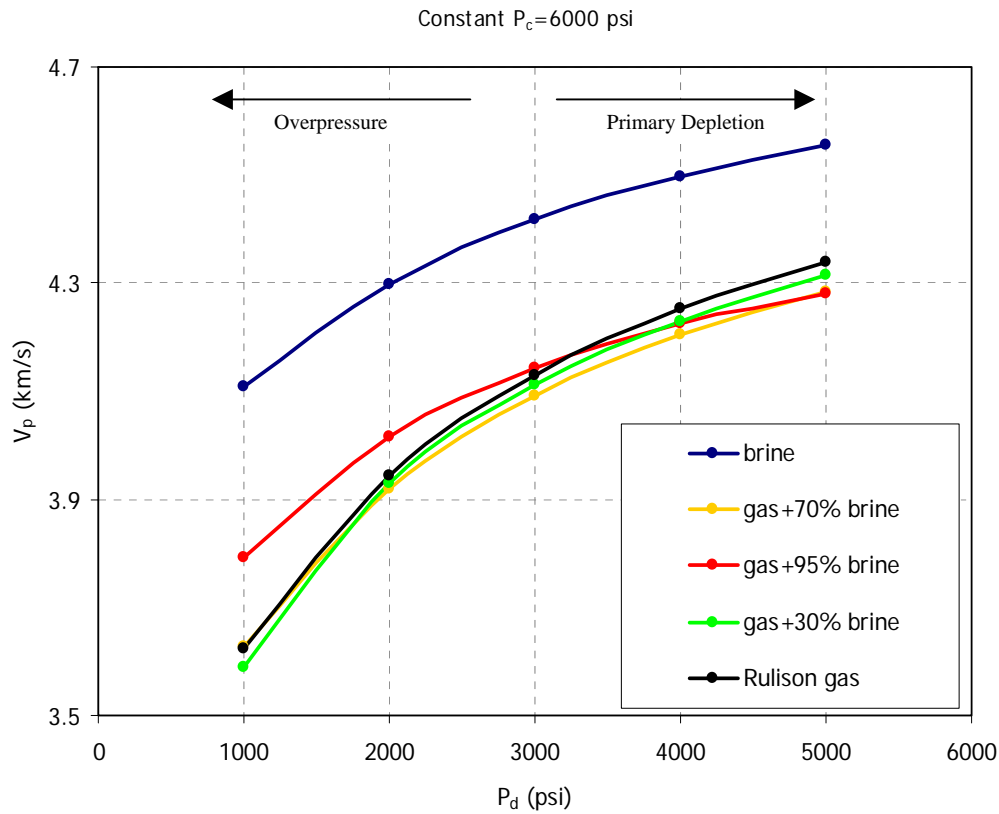


Figure 3-12 P-wave velocity changes with differential pressure and different pore fluid saturation at a constant confining pressure for sample R-5719V after Gassmann's fluid substitution.

In Figure 3-13 results from dry measurements (air-filled rock) are very close to the results after a fluid substitution with the reservoir gas. In this case the small change of S-wave velocity for brine-saturated rock is due to a density effect.

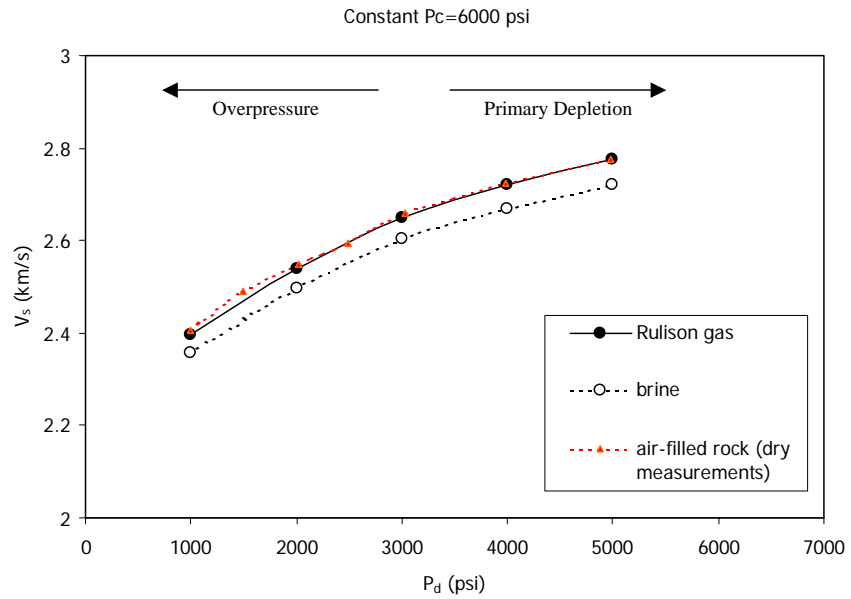


Figure 3-13 S-wave velocity changes with differential pressure and pore fluid (brine and Rulison gas) at a constant confining pressure for sample R-5719V after Gassmann's fluid substitution.

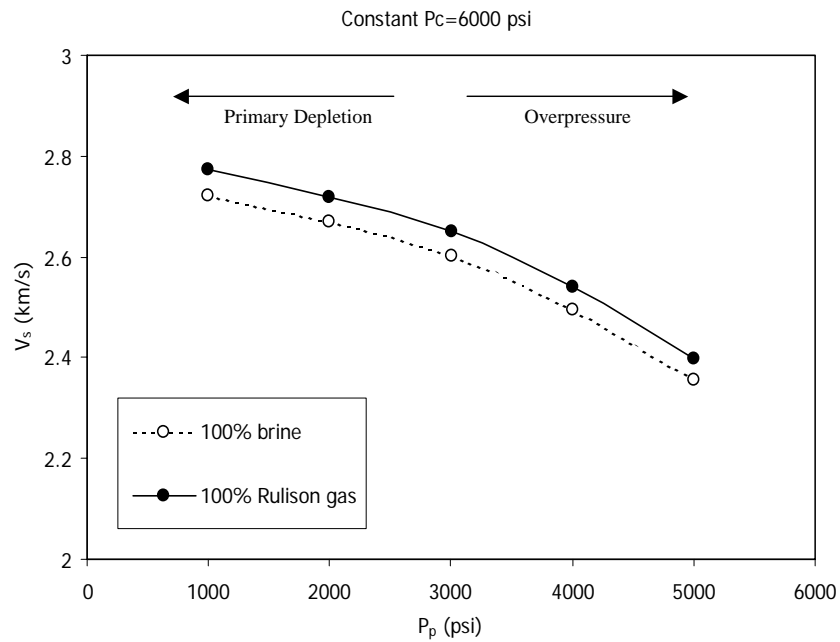


Figure 3-14 S-wave velocity changes with pore pressure and pore fluid (brine and Rulison gas) at a constant confining pressure for sample R-5719V after Gassmann's fluid substitution.

Figure 3-14 shows pore pressure influence on S-wave velocity for a gas and brine saturated rock. S-wave velocity decreases with increasing pore pressure.

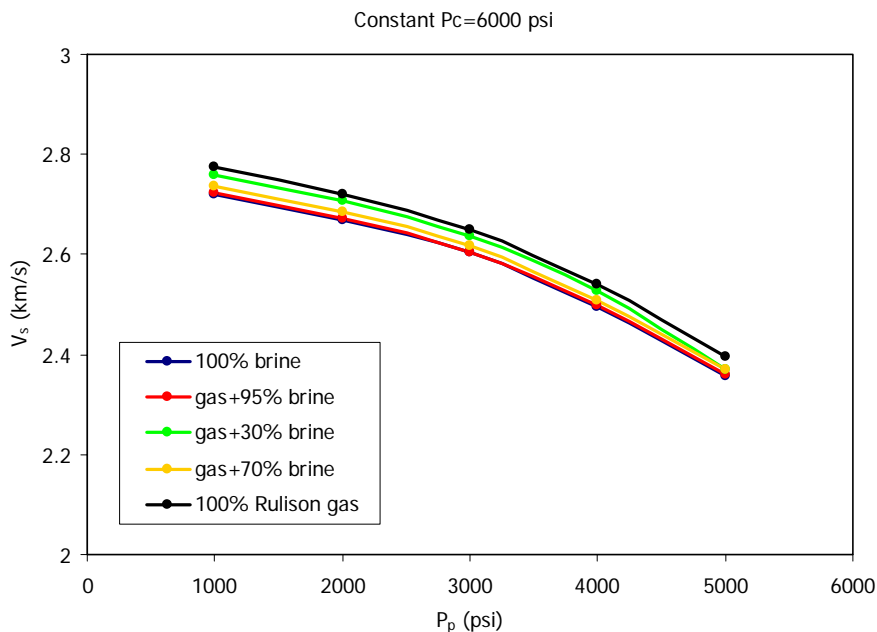


Figure 3-15 S-wave velocity changes with differential pressure and different pore fluid saturation at a constant confining pressure for sample R-5719V after Gassmann's fluid substitution.

Figure 3-15 shows Gassmann's modeling of more realistic scenarios in a reservoir. Different gas and brine saturation conditions are considered to model S-wave velocity. Figure 3-6 shows the modeling of fluid density modulus variation with differential pressure for different fluid saturation scenarios. It is possible to observe that the density changes are directly proportional to gas saturation changes. Since Gassmann's equation assumes shear modulus constant, the changes observed on V_s are mainly due to a density effect.

Using P-wave information alone can be ambiguous in many cases. A drop in P-wave can be caused both by overpressure and by presence of gas. Combining P-wave and S-wave information can help to differentiate between both cases. P- and S-wave information collected in the laboratory was used to compute V_p/V_s for dry measurements and for gas and brine-saturated rocks. Figure 3-16 and 3-17 show V_p/V_s for tight sandstone saturated with brine and gas as a function of differential pressure and pore pressure, respectively. In general, brine saturated sandstone has the highest V_p/V_s . Dry V_p/V_s measurements (air-filled rock) are very close to V_p/V_s results of a gas saturated rock after a fluid substitution with the reservoir gas.

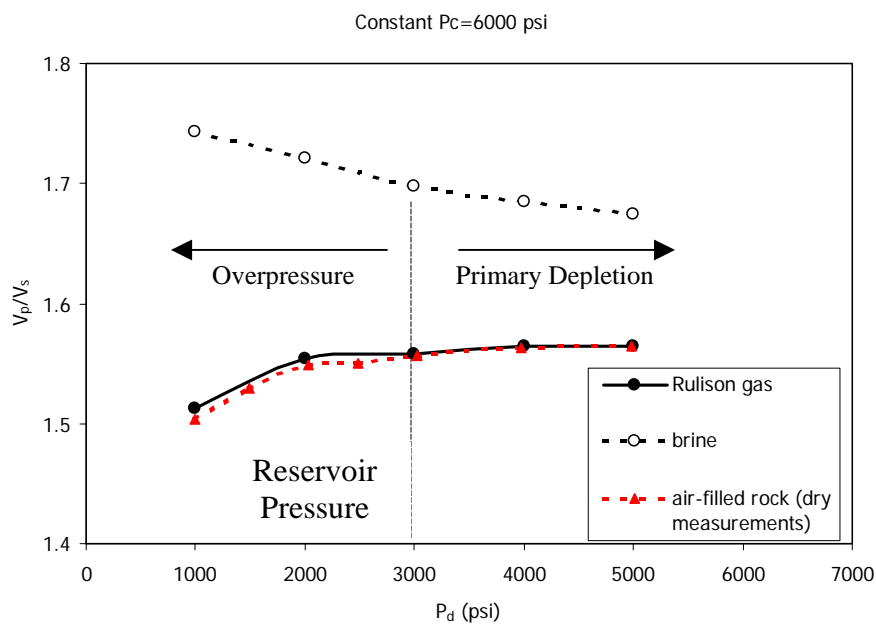


Figure 3-16 V_p/V_s versus differential pressure for a saturated sample (brine and gas) calculated with Gassmann's equation. Also dry measurements are plotted. The dashed line indicates reservoir pressure assuming a pore pressure gradient of 0.5 psi/ft.

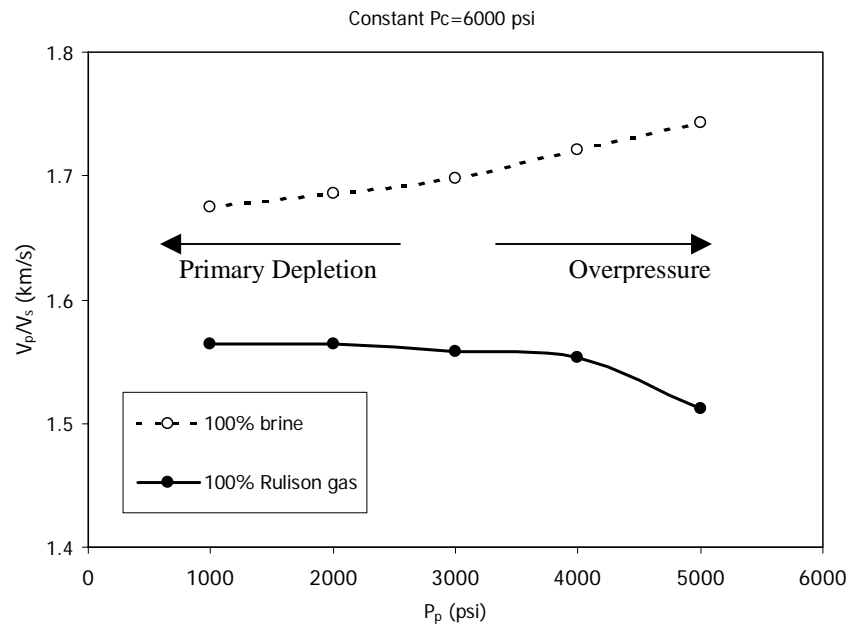


Figure 3-17 V_p/V_s changes with pore pressure and pore fluid (brine and Rulison gas) at a constant confining pressure for sample R-5719V after Gassmann's fluid substitution.

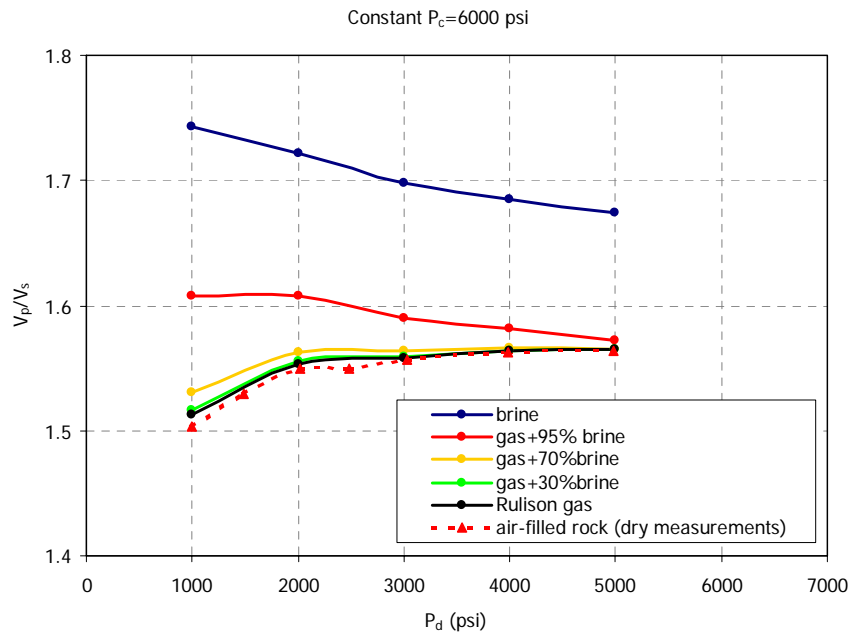


Figure 3-18 V_p/V_s changes with differential pressure and different pore fluid saturation at a constant confining pressure for sample R-5719V after Gassmann's fluid substitution.

Figure 3-18 shows the gas effect on V_p/V_s in tight sandstones. A small amount of gas will immediately drop P-wave velocity, and therefore V_p/V_s will decrease. At overpressure conditions the effect is larger.

3.3 Discussion of results

The numerical modeling using Gassmann's equation and laboratory core data allows us to understand the effects of pressure and pore fluid on velocities and changes can be quantified. The results obtained can be used for seismic reservoir characterization. It is also very important to understand the assumptions and limitations of the laboratory and numerical modeling done.

3.3.1 Overpressure and fluid effects on velocities

Analysis of ultrasonic P- and S-wave velocities in dry tight sandstones shows that V_p/V_s ratio at low differential pressures (overpressure conditions) decreases rapidly with pressure (Figure 3-19). For pressures greater than 2500 psi, V_p/V_s does not change much with pressure. The ultrasonic data show that V_p/V_s ratio can be used as an indicator of overpressure zones in tight gas sandstones (Figure 3-19).

V_p/V_s sensitivity to different fluids under differential pressure changes is shown in Figure 3-20. Rulison gas bulk modulus was calculated considering a mixture (Batzie and Wang, 1992) of 85% methane, 10% nitrogen, and 5% ethane. Due to the large compressibility of gas, the in-situ velocity in a gas-saturated rock is very close to that in

an air-filled rock (dry measurements) at the same differential pressure (Figure 3-20). Thus, measured velocity versus pressure data combined with fluid substitution can be used to predict velocity changes during the production process. This information can be used for time-lapse seismic data interpretation. Figure 3-20 shows that in water-saturated sandstones, V_p/V_s increases with increasing pore pressure (differential pressure decreases) and that an opposite trend exists for gas-saturated sandstones.

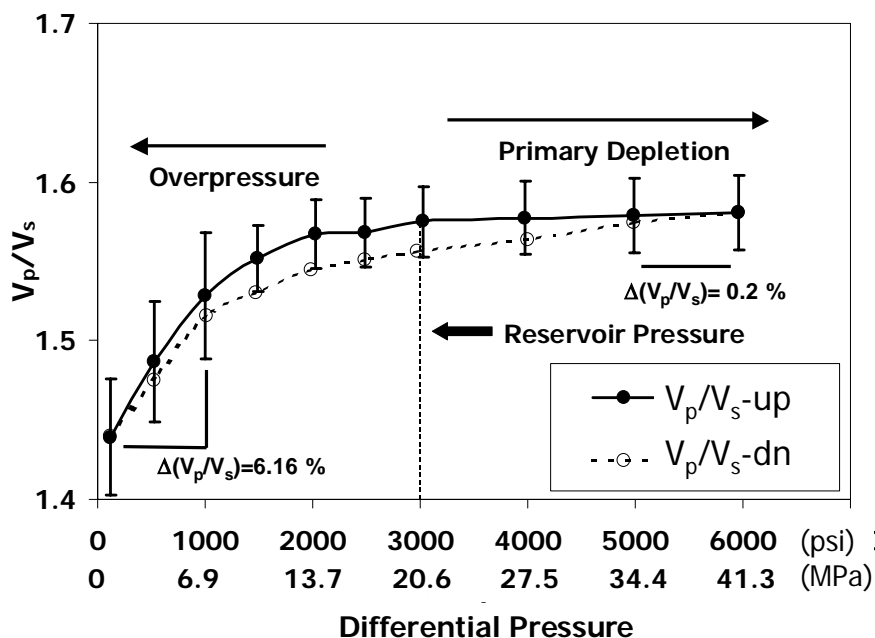


Figure 3-19 V_p/V_s versus differential pressure in a dry tight sandstone ($\phi=10\%$ and $k=42 \mu\text{D}$, depth=5719 ft). Filled symbols are velocities measured while increasing confining pressure. Open symbols are velocities measured while decreasing confining pressure.

From Figure 3-20, I estimate V_p/V_s variation for a typical tight sandstone due to pore fluid changes (100% gas to 100% brine) is approximately 8%. This change is less at partially saturated conditions and is enhanced by overpressure conditions. V_p/V_s variation

for a typical tight sandstone due to pore pressure increases (hydrostatic to overpressure) is approximately 6%. V_p/V_s variation due to pore pressure decreases (primary depletion) is less than 0.5% in unfractured tight sandstone cores. V_p/V_s changes due to primary depletion (pore pressure decreases) are difficult to observe in tight gas unfractured sandstones. However, the presence of fractures can enhance velocity changes (Xu et al., 2005). V_p/V_s is sensitive to pore pressure increases and could be used as an overpressure indicator.

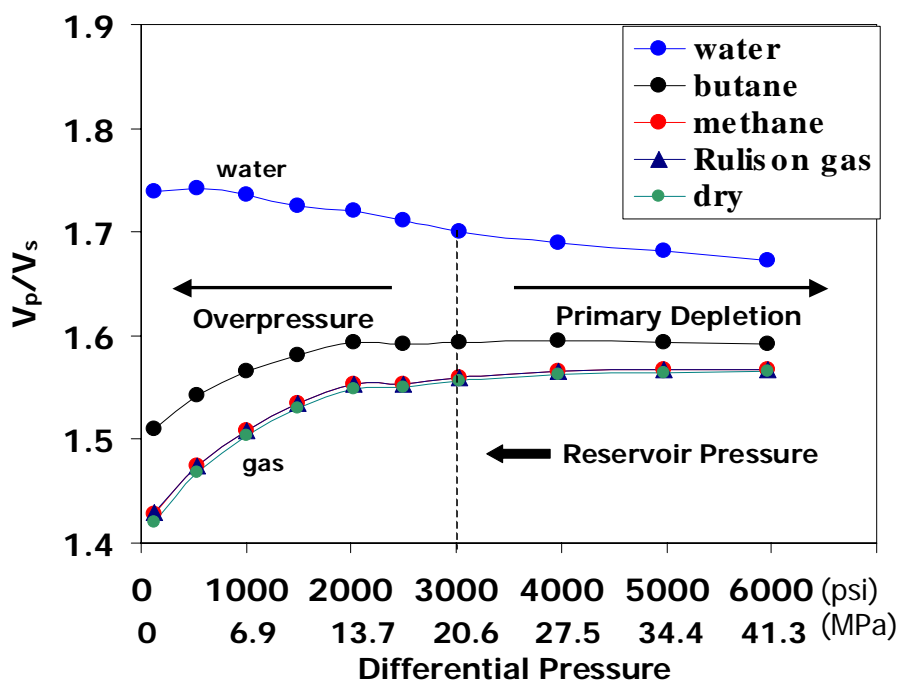


Figure 3-20. V_p/V_s versus differential pressure for a saturated sample (tight gas sandstone, $\phi=10\%$, $k=42\ \mu\text{D}$, depth= 5719 ft). Fluid substitution using Gassmann's equation was done for 100% water saturation (salinity 25000 ppm), butane, methane and a mixture of gases (85% methane, 10% nitrogen and 5 % ethane.), which represents Rulison Field gas.

3.3.2 Assumptions of experimental and modeling study

- Laboratory velocity measurements conducted under isotropic state of stress can be used to predict velocity in-situ conditions where, in general, there stress is not isotropic. This assumption is used since there is a lot of uncertainty in the horizontal stress in the reservoir. The results shown have limitations if the in-situ state of stress deviates from an isotropic system.

- The elastic-wave velocity in a rock is a function of the differential pressure rather than the effective pressure. This seems to be a good assumption for unconsolidated rocks, however for consolidated, low permeability and low porosity rocks, it has been shown (Hofmann et al., 2005) that the velocities in a rock is a function of effective stress.

- Gassmann's theory is assumed to be applicable to seismic modeling of Rulison Field rock matrix elastic properties. This theory seems to be a good option for initial modeling. Anisotropic rock physics modeling is necessary to evaluate the effects of fractures on the seismic properties of the reservoir.

Chapter 4

RELATIONS BETWEEN ELASTIC AND PETROPHYSICAL PROPERTIES FROM CROSS-DIPOLE SONIC LOGS

4.1 Introduction

In the laboratory, it is possible to test samples with a fixed lithology, porosity and permeability. The variation of seismic properties with pressure and fluid saturation can be studied for few samples. With sonic logging, it is also possible to obtain the variation of elastic properties with lithology, porosity, and fluid saturation under fixed in-situ conditions. When studying sonic logs, I assume small variations on pressure data, so seismic properties calculated from sonic logs are analyzed at a constant pore pressure.

There are many advantages of analyzing cross-dipole sonic data for reservoir characterization. With logs we obtain continuous information of rock properties in much larger volumes than with laboratory data. At the same time, sonic information from logs has a lower frequency than ultrasonic measurements.

Slowness P- and S-wave data from two cross-dipole sonic logs acquired in the field were analyzed at Williams Fork Formation interval (approximately from 4500 to 6500 ft of depth), with the purpose of estimating V_p/V_s of characteristic lithologies in the field (clean to shaley tight sandstones), and to calculate shear wave anisotropy.

V_p/V_s is sensitive to gas in most clastic reservoirs and will often show a marked decrease with gas presence (Kithas, 1976; Gregory, 1977; Tatham, 1982; Eastwood and Castagna, 1983; Ensley, 1984; McCormack et al., 1985). Shear waves are less sensitive to fluid or gas, and therefore give more information about the rock matrix. On the other hand, P-waves are sensitive to both matrix and pore fluid. When gas is present V_p will decrease, and since V_s is minimally affected by pore fluid, there is an overall decrease in V_p/V_s .

4.2 Quality control of the data

Many factors can affect log measurements. For example, when these measurements are made in the borehole with wireline logging tools or instruments embedded in the drill string, they are usually affected by the mud invaded zone around the borehole. Mud filtrate may penetrate the formation and partially replace the fluids around the well bore, and immediately affect the results of sonic logs, resistivity and others. Not taking invasion into account can lead to inaccuracies in porosity, permeability predictions, elastic rock properties estimations, and the correlation of surface seismic to wellbore data.

In order to quality control the data, it was necessary to determine whether the density, P-wave and S-wave velocity are from the virgin or from the invaded formation. The well log tools, such as the density, resistivity, and sonic measure the rock volume that extends from the borehole to some depth into the formation. Depending on the depth

of investigation of the different tools and the invasion during drilling, the well log measurements may be affected by the mud filtrate invasion.

In tight gas sandstones, low permeability reservoirs, rock properties prediction such as porosity, saturation, permeability, elastic properties, etc., are complicated, because conventional formation-evaluation techniques are often not applicable or can be more sensitive to errors in input parameters. In tight gas sandstones, there is complex lithology with poorly defined clay type and volume, the presence of thin beds, high heterogeneity, and rapid variations in invasion due to low permeability in μD range (Briceño, 2004).

Briceño (2003) developed and applied a forward model and inversion routine that not only uses shallow resistivity, but also porosity logs as input, and produces an invasion profile that differs from the typical step invasion model, porosity, and permeability indicators. Briceño (2004) applied this methodology at Rulison Field. Her results show that in the Williams Fork Formation, the most frequent invasion models are very shallow with a flushed zone shallower than the depth of investigation, and this can be explained because of the low permeability of the formation.

Briceño (2004) study shows that in Rulison Filed, we don't expect density and sonic logs to be directly affected by invasion. So, I assume in this study that the density tool measures past the invaded zone and deep into the formation, and therefore is measuring the virgin formation. In this case, I assume the fluid density for all calculations is the density of the mixture of gas and brine (irreducible water).

In the case of the sonic tool, I also assume that P-wave velocity and S-wave velocity will come from the virgin formation. Crossplots between P-wave velocity and S-wave velocity support this assumption.

4.3 Relations between porosity, lithology, fluids and elastic properties obtained from cross-dipole sonic logs

Different crossplots of petrophysical and elastic properties of the Rulison Field reservoir rocks were done, in order to reveal the interdependence among them. These crossplots will be used to identify lithology, pore fluid, and to predict porosity in future studies using seismic data.

As the main purpose of this thesis, I focus in the sensitivity of V_p/V_s to petrophysical properties. First, V_p and V_s are independently analyzed, and later combined through the estimation of V_p/V_s .

Combining information from gamma ray measurements and identifying the cross over effect from the neutron and density porosity it was possible to identify gas sands. Low V_p/V_s values for the sands charged with gas (V_p/V_s equal and lower than 1.6) were observed. In the presence of shales and shaley sandstones higher V_p/V_s were observed (V_p/V_s equal to or higher than 1.7).

As indicated in the previous Chapter, V_p/V_s is sensitive to gas in this reservoir and will show a marked decrease in its presence (as observed in Figure 4-1). I observe that V_p/V_s is a better lithology indicator than P-impedance in this reservoir.

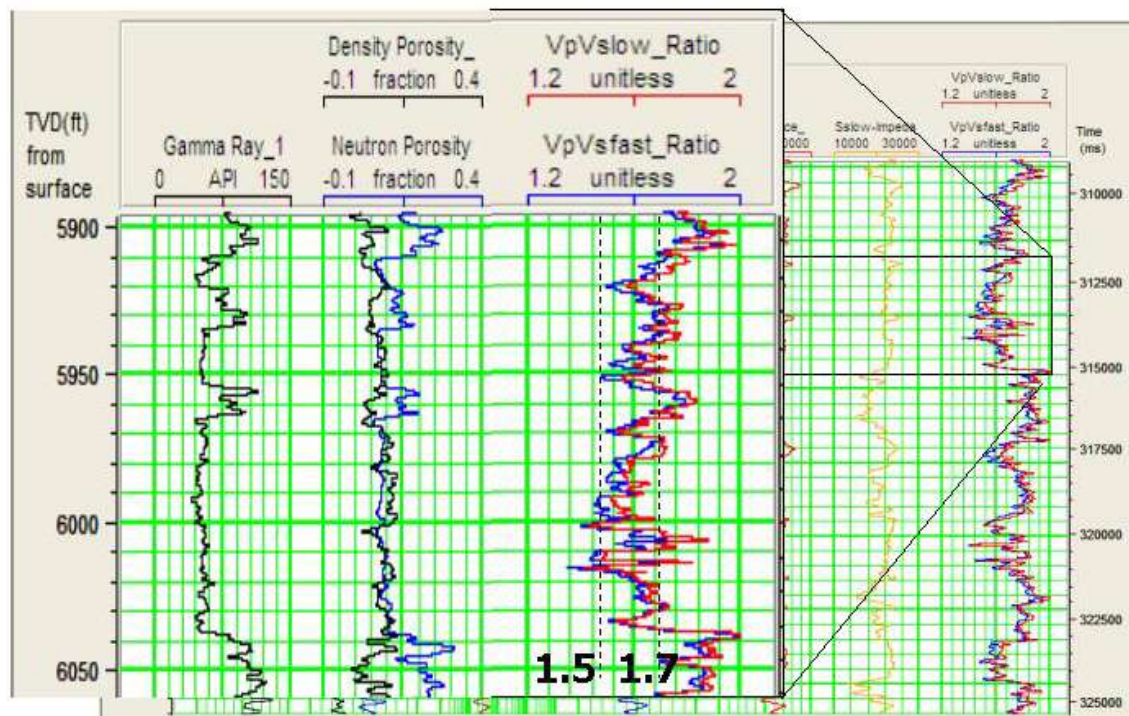


Figure 4-1 V_p/V_s calculated from P-wave slowness, S_1 slowness and S_2 slowness data from cross-dipole sonic log in well RWF332-21. The results were analyzed in combination with conventional log curves (gamma ray, caliper, resistivity, neutron and density porosity) to understand V_p/V_s variations with lithology and fluid.

Figure 4-2 shows V_p/V_{s1} , V_p/V_{s2} and shear anisotropy calculated along well RWF 332-21. It is interesting to observe high anisotropy values related to very thin sands, probably due to a higher density of fractures in thin sands. It is also interesting to observe that the higher values of azimuthal shear anisotropy correspond to these sands (Figure 4-3).

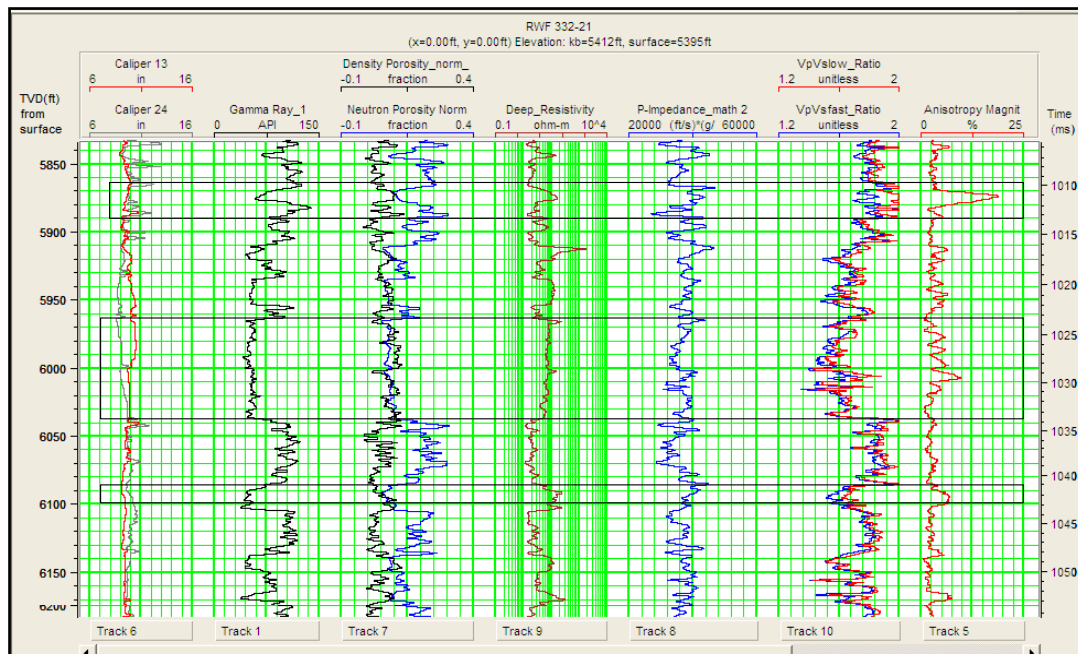


Figure 4-2 P-impedance, V_p/V_{s1} , V_p/V_{s2} and shear anisotropy magnitude calculated using the cross-dipole sonic acquired in RWF 332-21. Observe high anisotropy values related to very thin sands indicated with the rectangles.

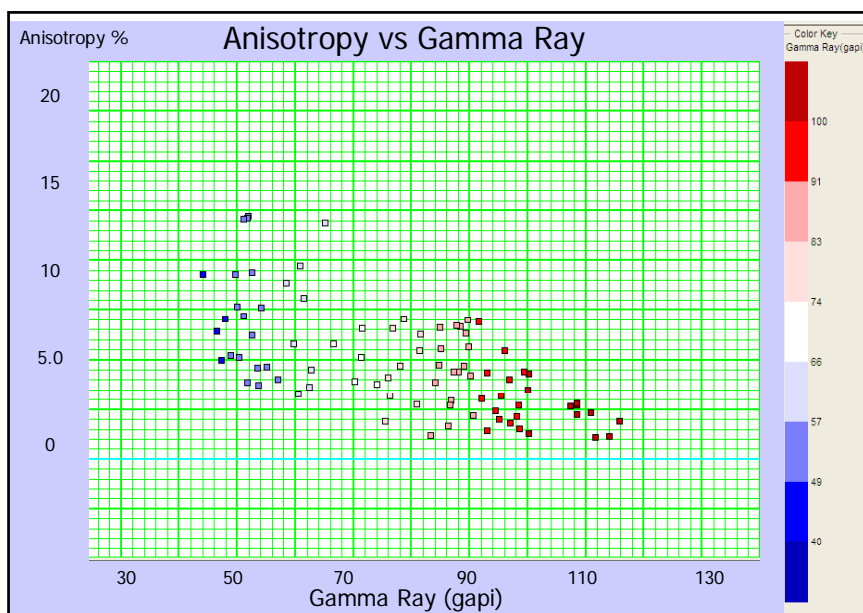


Figure 4-3 Anisotropy vs. gamma ray plot showing higher anisotropy values in sands.

4.3.1 Elastic properties and fluid-lithology discrimination

P-wave velocity alone is not a good indicator of lithology because of the overlap in V_p for various types of rocks. Additional information provided by V_s reduces the ambiguity. Figure 4-4 shows different regions identified in the V_p/V_s versus P-impedance crossplot. We can observe that it is possible to discriminate lithologies from V_p/V_s measurements. However, P-impedance alone is highly affected by fluid effects and there is ambiguity in lithology separation. Combining both P- and S-wave information we can separate fluid effects and lithology as shown in Figure 4-4. Low V_p/V_s values are directly related to sandstones with low clay content. Generally, there is a small increase in V_p/V_s for sandstones with more clay or shaliness. Shales themselves have significantly higher V_p/V_s than sandstones. Figure 4-4 shows a decrease in V_p/V_s and P-impedance for gas-saturated sandstones and an increase of V_p/V_s and P-impedance for water-saturated sandstones.

S-wave impedance is less affected by fluids, therefore, a crossplot of V_p/V_s versus S-wave impedance color-coded by gamma ray measurements shows better lithology discrimination (Figure 4-5). Tight sandstones will typically have a V_p/V_s lower than 1.7, while shales will have V_p/V_s higher than 1.7. Thus, we expect a decrease in V_p/V_s from shales to reservoir sandstones. Typically, the presence of gas-saturated sandstones lowers the V_p/V_s even further (V_p/V_s of 1.6 or lower) and overpressure conditions can lower V_p/V_s even more (<1.5).

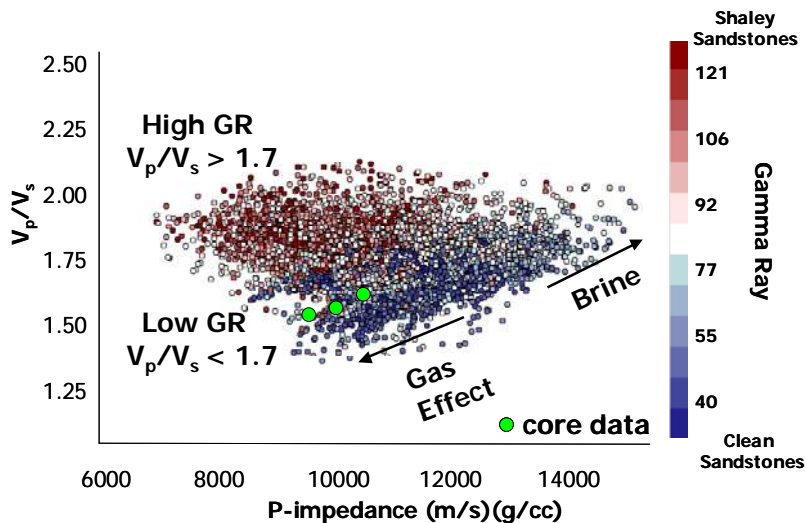


Figure 4-4 V_p/V_s versus P-wave impedance calculated from two dipole sonic logs (RWF 332-21 and RWF 542-20) in Rulison Field tight sands and shales. Blue symbols are for low gamma ray values. Red symbols are for high gamma ray values. The gas and brine effects are shown with the arrows. Gas saturated sandstone core data are integrated in the chart (green symbols).

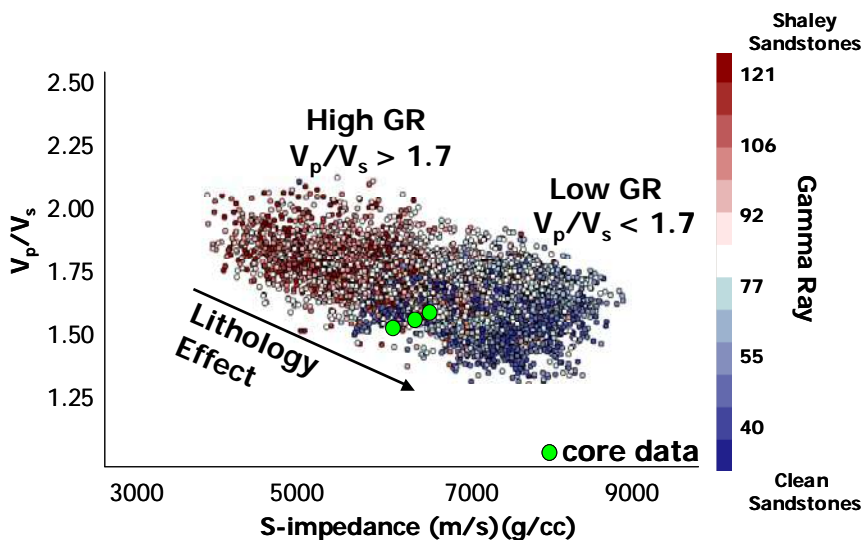


Figure 4-5 V_p/V_s versus S-wave impedance calculated from two dipole sonic logs (RWF 332-21 and RWF 542-20) in Rulison Field tight sands and shales. Blue symbols are for low gamma ray values. Red symbols are for high gamma ray values. Core data are integrated in the chart (green symbols). The arrow shows the trend of a V_p/V_s decrease and S-impedance increase due to the presence of clean sandstones.

4.3.2 Elastic properties and porosity

V_p and V_s versus density porosity are plotted independently in Figure 4-6 and 4-7.

Neutron porosity information is not used because the neutron porosity data is affected by high clay content in Williams Fork Formation.

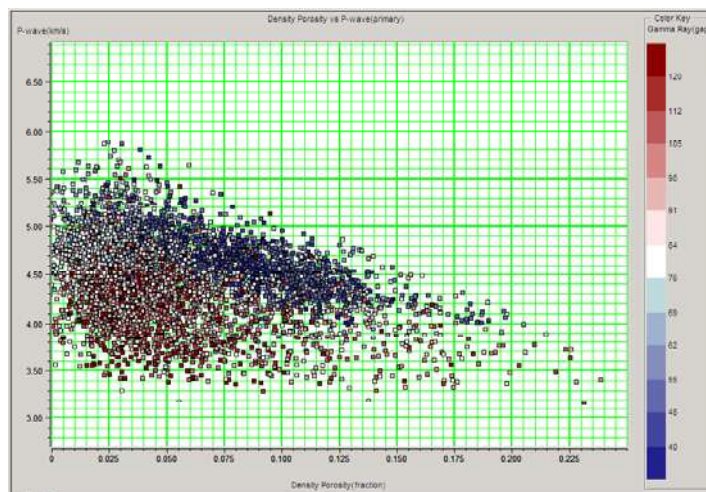


Figure 4-6 Crossplot of P-wave velocity versus density porosity of Williams Fork Formation (4500-6500 ft of depth) colored by gamma ray measurements.

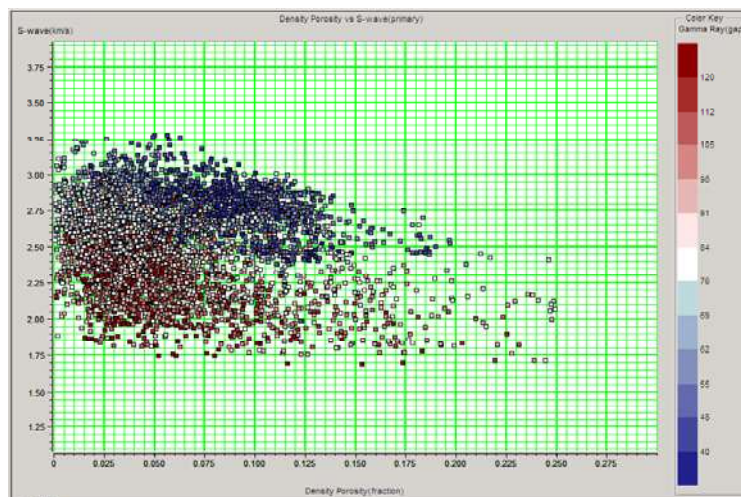


Figure 4-7 Crossplot of S-wave velocity versus density porosity of Williams Fork Formation (4500-6500 ft of depth) colored by gamma ray measurements.

Figure 4-6 and 4-7 show higher P- and S-wave velocities for clean sandstones than for shales and shaly sandstones. From V_p/V_s vs. porosity crossplot (Figure 4-8), it is possible to observe that when porosity in clean sandstones (blue dots) increases V_p/V_s decreases.

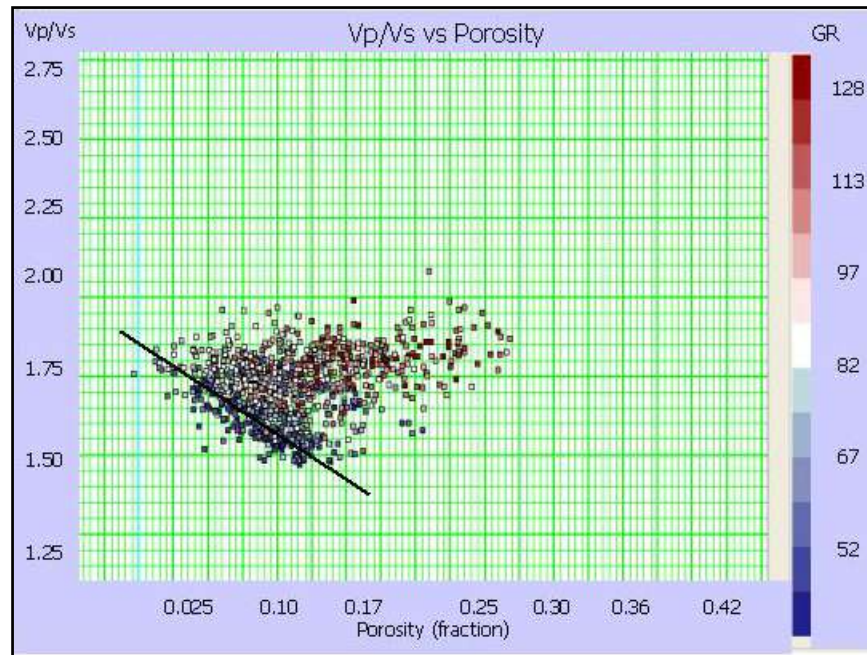


Figure 4-8 V_p/V_s versus porosity colored by gamma ray measurements.

4.3.3 Elastic properties and fluid saturation

From resistivity and porosity logs, water saturation S_w can be calculated using a modified Archie's equation (4-1) where the saturation and cementation exponents are both assumed to be equal to 2

$$S_w = \sqrt{a\phi^m \frac{R_w}{R_t}} \quad (4-1)$$

where a is a tortuosity factor,

R_w is the resistivity of formation water at formation temperature,

R_t is the true resistivity formation, and

m is a cementation exponent.

P-wave impedance is affected by fluids; therefore a crossplot of V_p/V_s versus P-wave impedance, color-coded by estimated water saturation measurements, shows a better pore fluid discrimination (Figure 4-9). Typically, the presence of gas-saturated sandstones lowers the V_p/V_s (V_p/V_s of 1.6 or lower). Figure 4-9 shows a decrease in V_p/V_s and P-impedance for gas-saturated sandstones (low S_w) and an increase of V_p/V_s and P-impedance for brine-saturated sandstones.

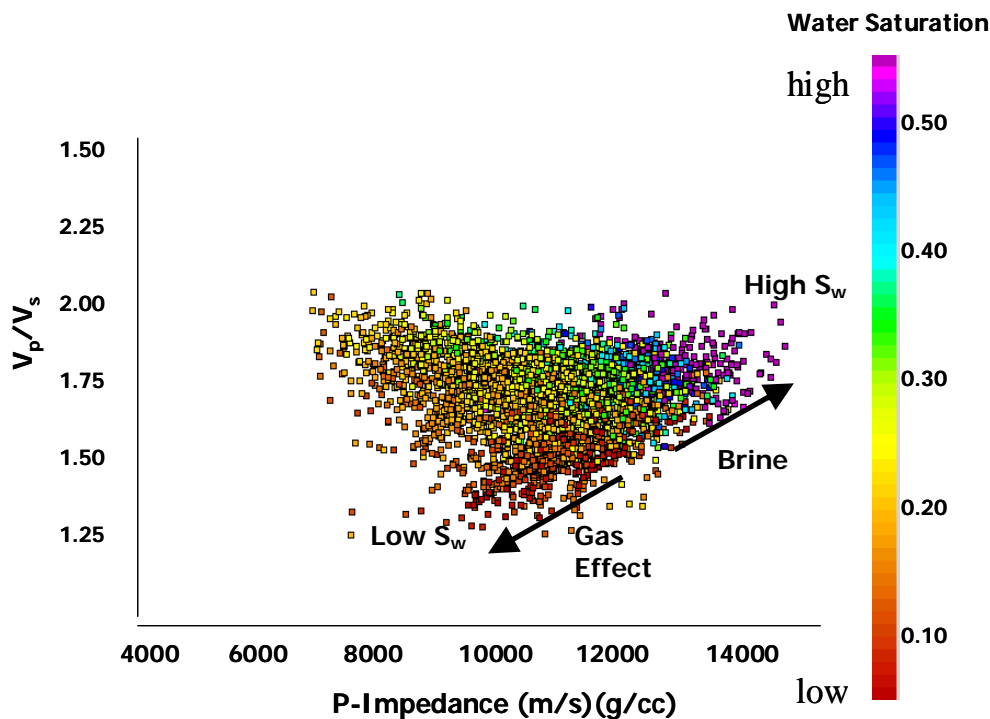


Figure 4-9 V_p/V_s versus P-wave impedance colored by estimated S_w . The gas and brine effects are shown with the arrows.

4.4 Discussion of results

Results from the cross-dipole sonic analysis show that V_p/V_s is a good lithology and hydrocarbon indicator in tight gas sandstone reservoirs. The presence of gas in the pore space reduces the bulk modulus and V_p is lowered, V_s will not be directly affected by fluids or gas, so the result is a drop of V_p/V_s in the presence of gas saturated sands.

4.4.1 Lithology and fluid effects on velocities

The results show that lithology has a significant influence on V_p/V_s . Fluid effects on V_p/V_s are significant but less than lithology effects. It is possible to separate fluid effects and lithology as shown in Figure 4-4, 4-5 and 4-9. This is possible when combining P-wave and S-wave information. Low V_p/V_s values are directly related to sandstones with low clay content. Generally, there is a small increase in V_p/V_s for sandstones with more clay or shaliness. Shales themselves have significantly higher V_p/V_s than sandstones. S-wave impedance is less affected by fluid effects, therefore can be used as a lithology discrimination. Tight sandstones will typically have a V_p/V_s lower than 1.7, while shales will have V_p/V_s higher than 1.7. Thus, I expect a decrease in V_p/V_s from shales to reservoir sandstones. Typically, the presence of gas-saturated sandstones lowers the V_p/V_s even further (V_p/V_s of 1.6 or lower).

4.4.2 Quantifying V_p/V_s variations

From laboratory analysis I estimate V_p/V_s variation for a tight sandstone due to pore fluid changes (100% gas to 100% brine) is approximately 8%. This change is less at partially saturated conditions and is enhanced by overpressure conditions. Similarly using log analysis (Figure 4-5), I estimate the V_p/V_s variation due to lithology changes (clean to shaley sandstone and shales) is approximately 12%.

The results show that lithology has a significant influence on V_p/V_s . Fluid effects on V_p/V_s are significant but less than lithology effects. V_p/V_s change due to primary depletion (pore pressure decrease) is difficult to observe in tight gas sandstones. However, V_p/V_s is more sensitive to pore pressure increases and could be used as an overpressure indicator.

4.4.3 Assumptions of log analysis

- Density and sonic logs are not affected by invasion during drilling. I am assuming the density and sonic tool measurements past the invaded zone and deep into the formation, therefore providing measurement of the virgin formation. In this case, I assume the fluid density for all calculations is the density of the mixture of gas and brine.
- Porosity calculated from density logs is a good approximation of true porosity in the reservoir zone.

Chapter 5

ELASTIC ROCK PROPERTIES FROM SEISMIC DATA AND APPLICATIONS

5.1 Introduction

Seismic reservoir characterization includes the application of rock physics to seismic data to predict pore fluids, lithology, pore pressure (e.g., Landro et al., 2003) and rock properties such as porosity and permeability (e.g., Prasad, 2003). An understanding of the relations between elastic rock properties (e.g., μ , λ , V_p/V_s , I_p , I_s) and petrophysical (e.g., porosity, permeability) and reservoir conditions (e.g., pore fluid and pressure) is necessary. Chapter 2, 3 and 4 focus on obtaining these relations from laboratory experiments and numerical rock physics modeling using core data and from cross-dipole sonic analysis. This Chapter focuses on obtaining elastic rock properties from seismic and applying the relations obtained from core and log data to better characterize the reservoir.

In order to apply the relations obtained between elastic properties of rocks and petrophysical properties, it is necessary to calculate elastic properties from seismic data, such as, V_p/V_s , P-impedance, S-impedance. A 9-C multicomponent seismic survey, acquired by RCP (Reservoir Characterization Project) during October 2003 was used in

this thesis. Elastic rock properties were estimated from this data set. One year later, during October 2004, a monitor multicomponent survey was acquired with similar acquisition parameters. In this thesis I focus on the 2003 survey. However, the relations obtained from laboratory experiments under pressure changes can be applied for time-lapse interpretation at Rulison Field.

First, quality control of seismic data and review of processing workflows were done in order to understand the limitations in the processing that might affect the amplitude of the data. Synthetic seismic traces were made from sonic and density logs to tie wells to seismic in P, S and PS time domain. Key horizons were interpreted in the multicomponent seismic data, and interval V_p/V_s was estimated. Finally, acoustic and elastic impedance inversions were done using P- and S-wave data. The rock physics relations obtained in Chapter 2, 3 and 4 are used for interpretation of 3D multicomponent seismic, and to aid the acoustic and elastic impedance inversion. This integrated methodology can enhance the reservoir characterization, reduce drilling risk and enhance field productivity.

5.2 Multicomponent seismic interpretation

Here, I present the analysis and interpretation of coupled P- and PS-wave data at Rulison Field. Interpretation for pure S-wave data was obtained from Jansen (2005). A complete review and comparison of P-, PS-, and S-wave was done in this study. Successful well synthetic ties were done in the three time domains (P, PS, and S) in six

different wells in the field, in order to assist multicomponent seismic interpretation and inversion.

Coupled P-wave and PS-wave seismic analysis allows us to derive information about P- and S-reflectivities. Shear wave data is sensitive to rigidity and density, while compressional wave propagation is sensitive to rigidity, density and compressibility. When combining both (P and S reflectivities) we can discriminate lithology, porosity, fluid content, and pore pressure (Landro et al., 2003). It is also true that it has been difficult to interpret P- and PS-wave volumes consistently. These difficulties are related to the different event times and frequencies in the PS-wave data, together with differences in P-wave and PS-wave reflectivities. Due to the difference in frequency, velocity, wavelength and reflectivity, PS sections may exhibit geologically significant changes in amplitude or character of events, which are not apparent on conventional P-wave sections. Improved images can be obtained with PS- and pure S-wave data when the presence of gas causes poor seismic data areas in the P-wave sections.

Many challenges are faced during multicomponent seismic interpretation:

- PS-wave data have lower frequency than conventional P-wave data. PS-wave is more highly attenuated than P-wave. Unconsolidated shallow zones (weathering layer) with high V_p/V_s can cause high attenuation in PS- and S-wave data.
- The processing of PS data is complex due to the asymmetry of PS-wave gathers. In the presence of anisotropy (fractured reservoirs) the processing is even more

complicated, and processing has to take into account anisotropy so true amplitudes can be obtained.

- It is difficult to identify geologic markers on PS data and insure that P and PS interpretations are consistent. PS-wave data gives better seismic imaging in areas where the presence of gas affects conventional P-wave data seismic.

Through the analysis of multicomponent data, important elastic rock properties such as interval V_p/V_s can be calculated. This property can improve predictions about lithology, porosity, and reservoir fluid type as shown previously in Chapter 3 and 4. Compressional seismic velocity alone is not a good lithology indicator because of the overlap in V_p for various rock types. The additional information provided by V_s can reduce uncertainty involved in interpretation.

Travel time interpretation for interval V_p/V_s estimation using both P- and PS-wave data was performed on the Rulison data. Rock physics relations studied in Chapter 3 and 4 were used to interpret interval V_p/V_s obtained from travel time interpretation.

During the coupled P- and PS-wave data interpretation a detailed workflow was followed which includes:

- Build synthetics seismograms in P, and PS-time using dipole sonic logs.
- Correlate and interpret key P and PS horizons.
- Create interval V_p/V_s maps at the reservoir level (Williams Fork Formation) and compare anomalies.

P-, PS-, S-wave data sets were visually compared and the main reflectors in all three volumes were identified using the well ties to seismic. In this study, the main focus interval is on the Williams Fork Formation. The first step during the analysis of the data was to identify the horizons of interest (top and base of the reservoir) in P- and PS- time (S-time horizons were provided by Jansen, 2005). The coupled P- and PS-wave interpretation of reflections was guided by P and PS synthetic seismograms created from available dipole sonic and density log information. Strong P reflections (top of UMV-shale and top of the Cameo coal) can be correlated with corresponding PS reflections with low uncertainty or error.

5.2.1 Well ties to seismic

Using dipole sonic information available in the field, P-, S-, and PS-synthetic traces were computed and used to tie the seismic data. Figures 5-1 and 5-2 shows synthetic ties in P-time and PS-time domain respectively. The examples shown are from well RMF 332-21. For both figures, the blue trace is the synthetic zero-offset P-wave response calculated from the log. The red trace beside the seismic is an average of the nine nearest traces surrounding the well location. The logs were bulk shifted for a better alignment with the seismic. Impedances were computed using density and velocity logs. Correlation coefficients were computed for each well tie to seismic. Final correlations for P- and PS-wave data are better than 75%.

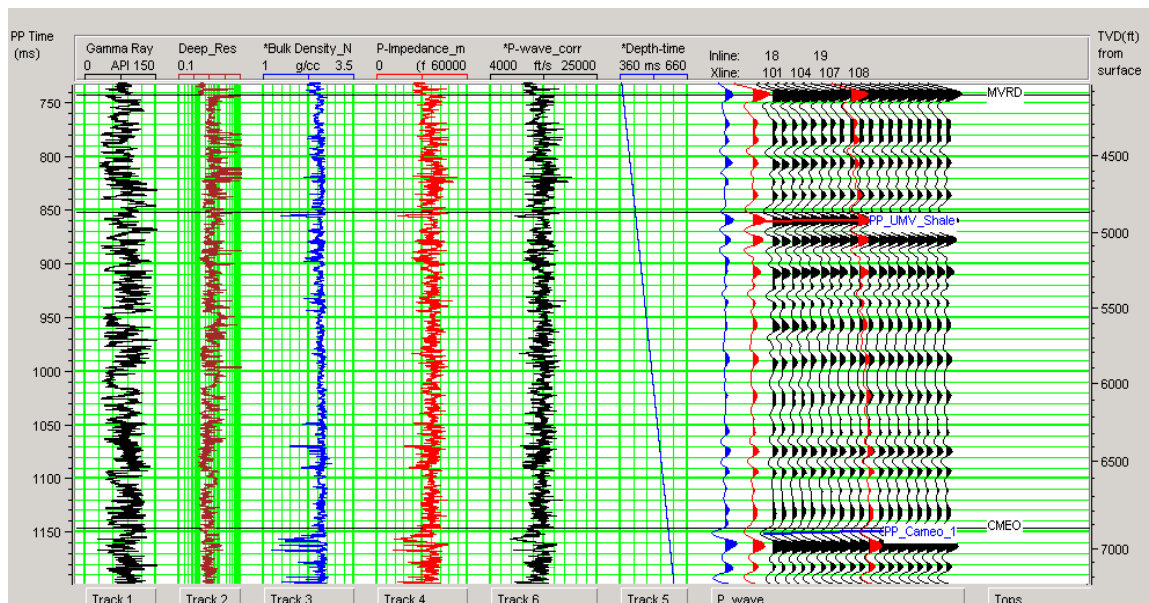


Figure 5-1 P-wave data tie to well control. From left to right the different curves are gamma ray log, deep resistivity log, density log, calculated P-impedance, P-wave log, depth-time curve, P-synthetic trace (blue), actual seismic trace at well location (red), seismic profile through the well location, formation top and horizon interpretation around the well (blue).

The ties allow us to identify the reflections of interest in this study (top of the UMY shale and top of the Cameo coal). After geological tops and main reflections are tied, it is possible to obtain V_p/V_s from corrected P- and S-wave logs. Registration of events is a key element for P- and PS interpretation. In order to take advantage of reflectivity differences on P- and PS-waves (Figure 5-3), and relate these differences to rock and fluid properties, one must be confident that P- and PS-data are correctly tied to depth.

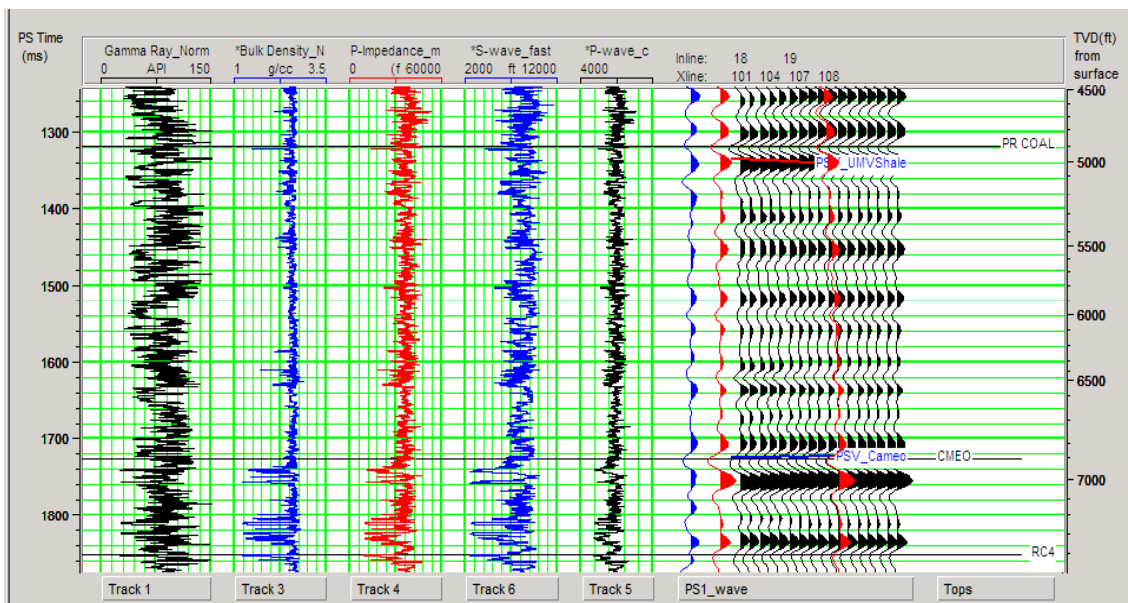
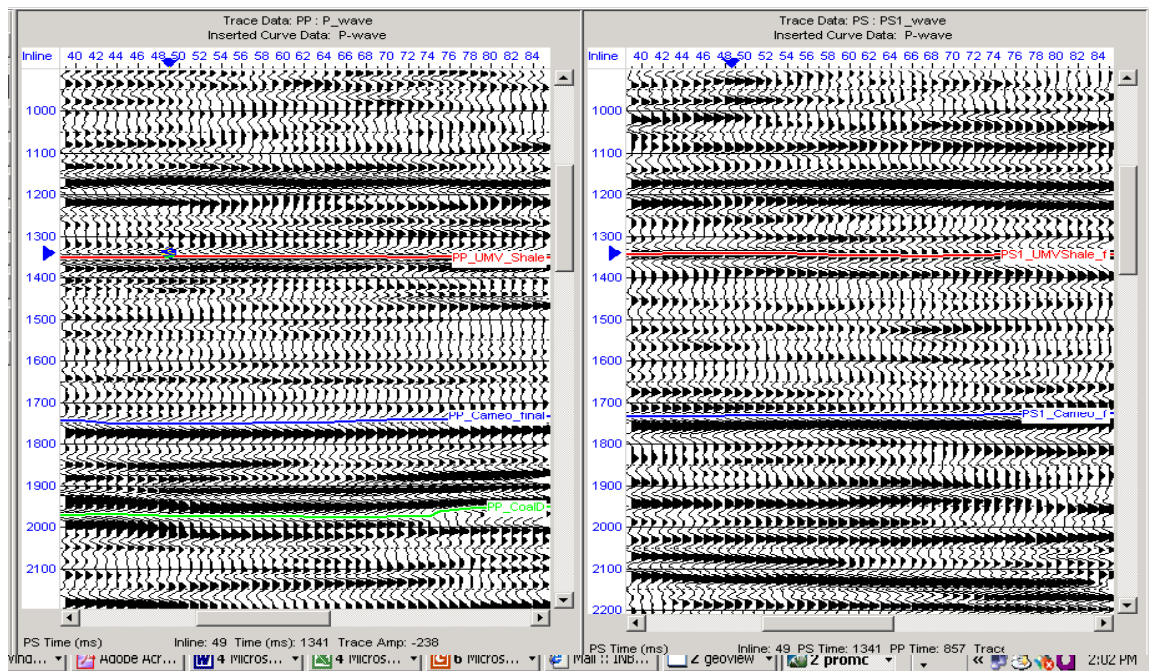


Figure 5-2 PS-wave data tie to well control. From left to right the different curves are gamma ray log, density log, calculated P-impedance log, S wave and P-wave logs, PS synthetic trace (blue), actual seismic trace at the well location (red), seismic profile through the well location, formation top and horizon interpretation around the well (blue).

Figure 5-3 shows the P- and PS-wave data both in PS time after registration of events using a spatially variant V_p/V_s function obtained after interpolating the V_p/V_s information from wells after log correlation to seismic.

5.2.2 Interval V_p/V_s estimation from multicomponent travel time data

In this study, isochron ratios between the top of the UMV shale and the top of the Cameo coal were computed from P-wave and PS-wave horizon interpretation. These isochrons are directly used in Equation 5-1.



PP data (PS time)

PS₁ data (PS time)

Figure 5-3 Migrated sections from RCP 2003 multicomponent survey (Inline 48). P-wave data is on the left, PS data on the right. PP and PS data are represented in PS time. Key horizons (top of UMV shale and Cameo coal) were picked on the P-wave volume and on the PS volume. Note the differing reflectivity between the PP and PS sections.

$$\frac{V_p}{V_s} = \frac{2\Delta t_{PS} - \Delta t_P}{\Delta t_P} \quad (5-1)$$

where V_p is P-wave velocity,

V_s is S-wave velocity,

Δt_{PS} is the isochron in PS time, and

Δt_P is the isochron in P time.

Figure 5-4 shows the interval V_p/V_s map between the UMV shale and the Cameo coal reflections. Due to the high heterogeneity of the reservoir, it was not possible to compute higher resolution V_p/V_s maps of thinner intervals or individual sands bodies from the Williams Fork Formation. The map shown in Figure 5-3 can be interpreted in terms of V_p/V_s as an average of rock properties from top to bottom of the thick reservoir (1700 to 2000 ft). There is high uncertainty in this kind of map because of the high heterogeneity in the Williams Fork Formation and the difficulty to map individual sand bodies from this interval in PP and PS data. We are interested in identifying low anomalies in the V_p/V_s maps, which could be indicative of overpressure areas (potential prospect areas), gas fluid content and good rock quality (clean sandstones) as shown in Chapter 3 and 4.

The results from laboratory and dipole sonic log data analysis showed that lithology has a significant influence on V_p/V_s . Fluid effects on V_p/V_s are significant but less than lithology effects. V_p/V_s is also sensitive to pore pressure increases and could be used as an overpressure indicator.

Low V_p/V_s is related to good quality reservoir rocks (sandstones with low clay content) and gas overpressure conditions in tight gas sandstones. The possibility of detecting pressure, lithology and fluid effects by analyzing V_p/V_s extracted from multicomponent reflection data, will depend on the accuracy of the velocities obtained from seismic. Discrimination between the different effects from seismic is difficult. However, at Rulison Field, low V_p/V_s anomalies can be interpreted as a prospect

indicator, since we are looking for gas-saturated sandstones at overpressure conditions (undrained areas) and we have shown that in this case, fluid, lithology and pressure conditions, all contribute to lower V_p/V_s .

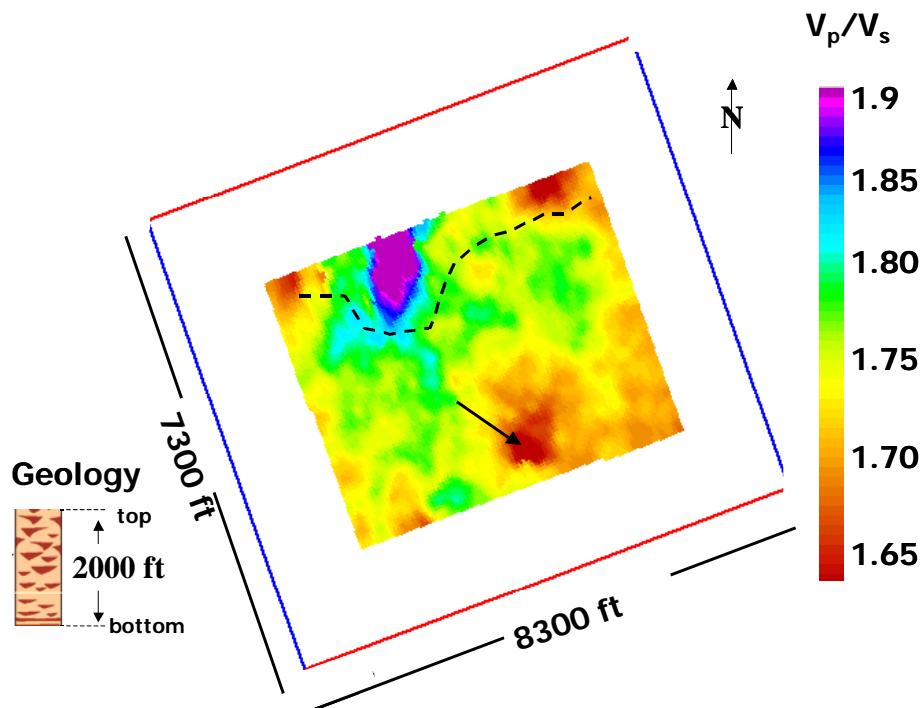


Figure 5-4 Interval V_p/V_s map from the top of UMV shale to the top of Cameo coal, computed using P- and PS-wave data. The black arrow indicates an anomaly of low V_p/V_s .

From Figure 5-4 it is possible to observe a low V_p/V_s anomaly indicated by the arrow that is interpreted as a potential prospect area. Since this map is a measure of V_p/V_s on a thick heterogeneous interval (1700 to 2000 ft), it is showing an average of rock properties (sandstones with different clay content and shales) with possible areas saturated by gas. As mentioned before, there is a high uncertainty in this kind of map, due

to the high heterogeneity of the interval and limitations to measure higher resolution V_p/V_s from travel time information. Therefore, different methods such as AVO analysis, acoustic and elastic inversion have to be used to obtain higher resolution elastic properties (V_p/V_s , I_p , I_s).

5.3 Application of rock physics to multicomponent seismic data inversion

It is very important to obtain and understand the rock physics trends of the field, which relates rock elastic properties to rock bulk properties and reservoir conditions, and therefore reduce uncertainty in seismic data interpretation. Such rock physics trends are derived from log and core data (Chapter 3 and 4), and then applied to seismic data.

Elastic properties such as P-impedance, S-impedance, Poisson's ratio and V_p/V_s can be obtained from seismic data using acoustic and elastic impedance inversion (Connolly, 1998). For this purpose Hampson-Russell Strata software is used to invert multicomponent data using the model based inversion technique (Hampson-Russell Software Services, Ltd.). P-impedance and S-impedance from multicomponent data in Rulison Field were estimated.

All inversion algorithms suffer from non-uniqueness. In other words, there is more than one possible geological model consistent with the seismic data. To constrain the solution the model based inversion technique uses an initial guess model constructed with sonic log data and seismic horizons.

Model based inversion method minimizes an objective function (Equation 5-2),

$$J = \text{weight}_1(T - W * r) + \text{weight}_2(M - H * r) \quad (5-2)$$

where T is the seismic trace,

W is the wavelet,

r is the final reflectivity,

M is the initial guess model impedance,

H is the integration operator which convolves with the final reflectivity to produce the final impedance, and

$*$ is the convolution process.

The first term of the equation forces a solution that models the seismic trace, and the second term of the equation forces a solution that models the initial guess impedance using the specified block size. The weights determine how the two parts are balanced.

A practical scheme of the model based inversion technique involves the following steps: wavelet extraction, building a geological initial model and integrating the geological model with the inverted seismic data (Russell, 2005).

Important limitations to take into account when using this method are (Russell, 2005):

- The wavelet is assumed to be known, and its effects are removed, as much as possible, from the seismic during the calculation. Therefore errors in the estimated wavelet will cause errors in the inversion results.
- The results can be very much dependent on the initial guess model. However, this can be alleviated by filtering the model.
- There is a non-uniqueness problem.
- The results are high resolution, high frequency detail, but the detail may be coming from the initial guess model, and not from the seismic.

The model based inversion was applied to Rulison Field P- and S-wave data independently. In order to avoid survey edge effects, a smaller area of the RCP survey was chosen for inversion. Figure 5-4 shows the location of RCP survey and the sub-area used during the inversion of P- and S-wave data. Also the wells used during construction of the initial guess model are shown in Figure 5-5. For each inversion process an initial guess model was derived using dipole sonic data available and horizons interpreted on P and S-wave data.

Figure 5-6 shows possible P-impedance values obtained after the model based inversion calculation. The values obtained are consistent with P-impedance calculated from core and log data (Figure 4-4 in Chapter 4).

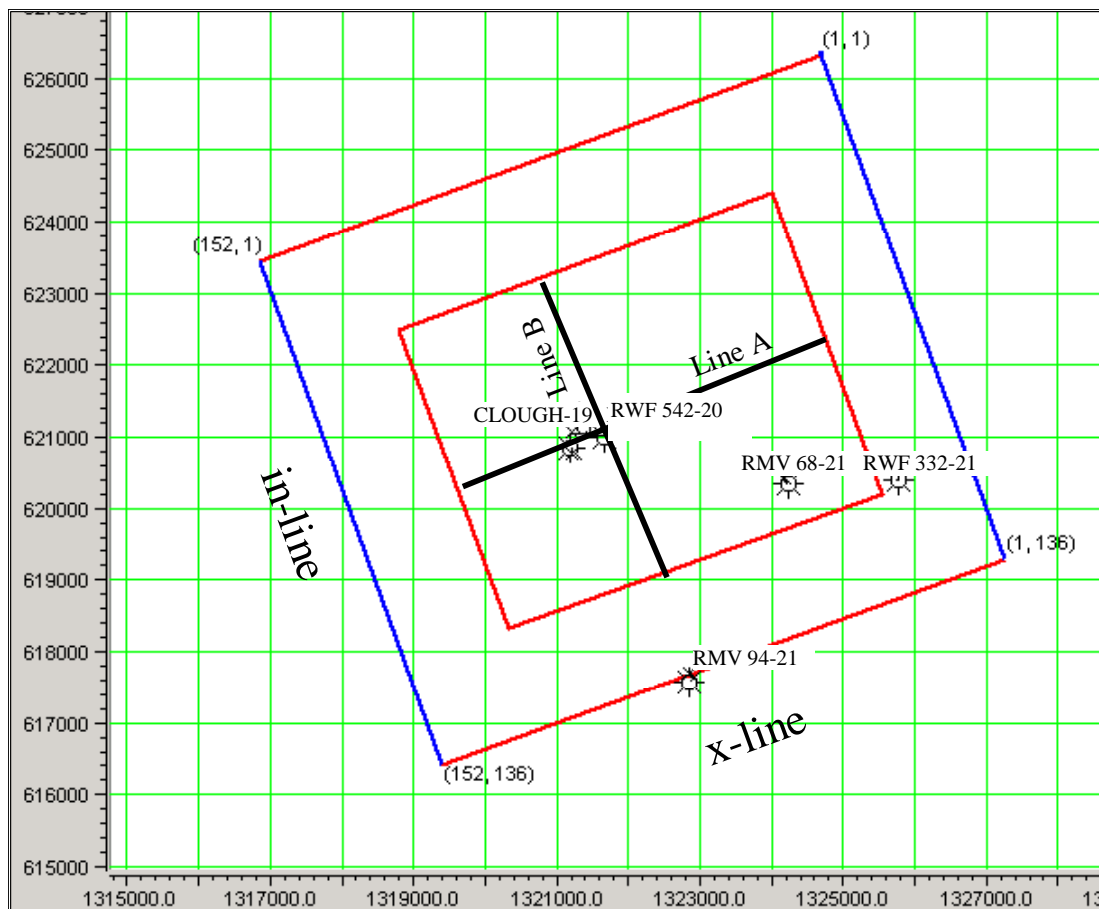


Figure 5-5 RCP survey area represented by the external polygon and sub-area of the survey used for the seismic inversion is represented by the smaller polygon. Note the location of the wells with P- and S-wave log information used for the construction of the initial guess model.

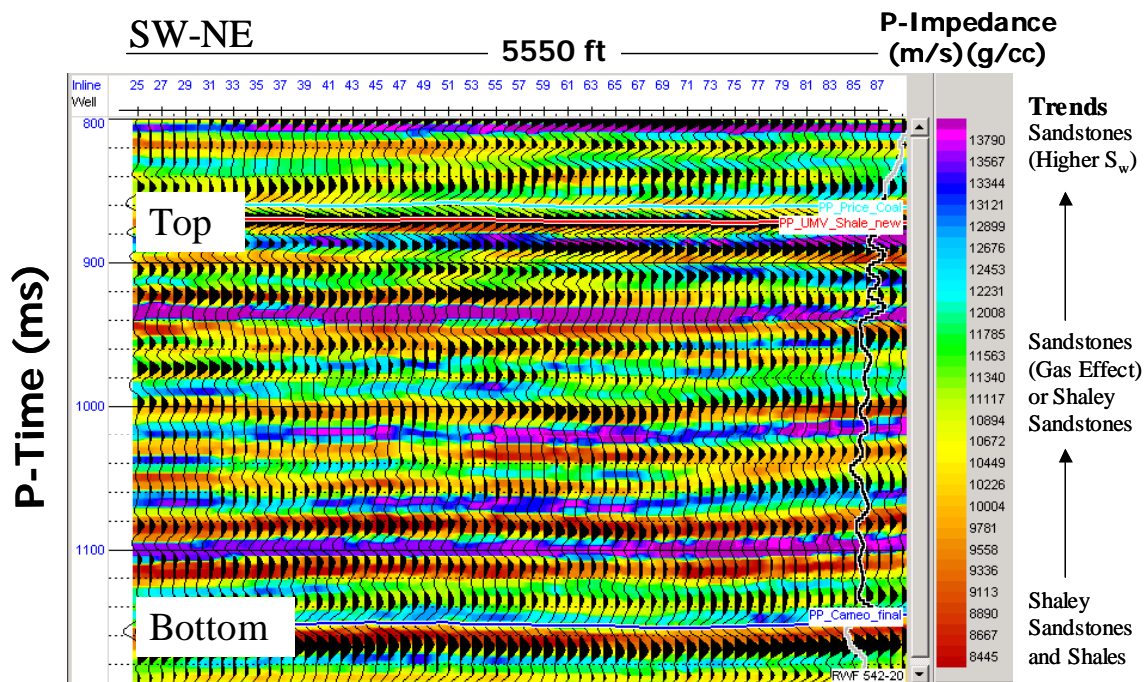


Figure 5-6 Seismic line A (x-line 72) from Rulison Field showing the P-impedance inversion from post-stack data in P-time. Note the location of the top (top of UMV shale) and bottom (top of Cameo coal) of the area of interest or reservoir. Filtered P-impedance log from well RWF 542-20 is plotted to quality control the acoustic inversion results. Figure 5-5 shows the location of the line.

The crossplot of V_p/V_s versus P-impedance is shown on Figure 4-4 in Chapter 4. It illustrates that gas saturated sands have low V_p/V_s and medium to low P-impedance values. The inversion in Figure 5-6 and 5-7 shows areas with very low P-impedances that are related with shaley areas, this is confirmed with the low impedance zone corresponding with the UMV shale. Medium P-impedance values (green and yellow areas) could be related with clean sandstones saturated with gas. However, as discussed in Chapter 4, P-impedance alone is not a good lithology indicator because of the overlap

in V_p for various types of rocks. Additional information provided by V_s and S-impedance reduces ambiguity.

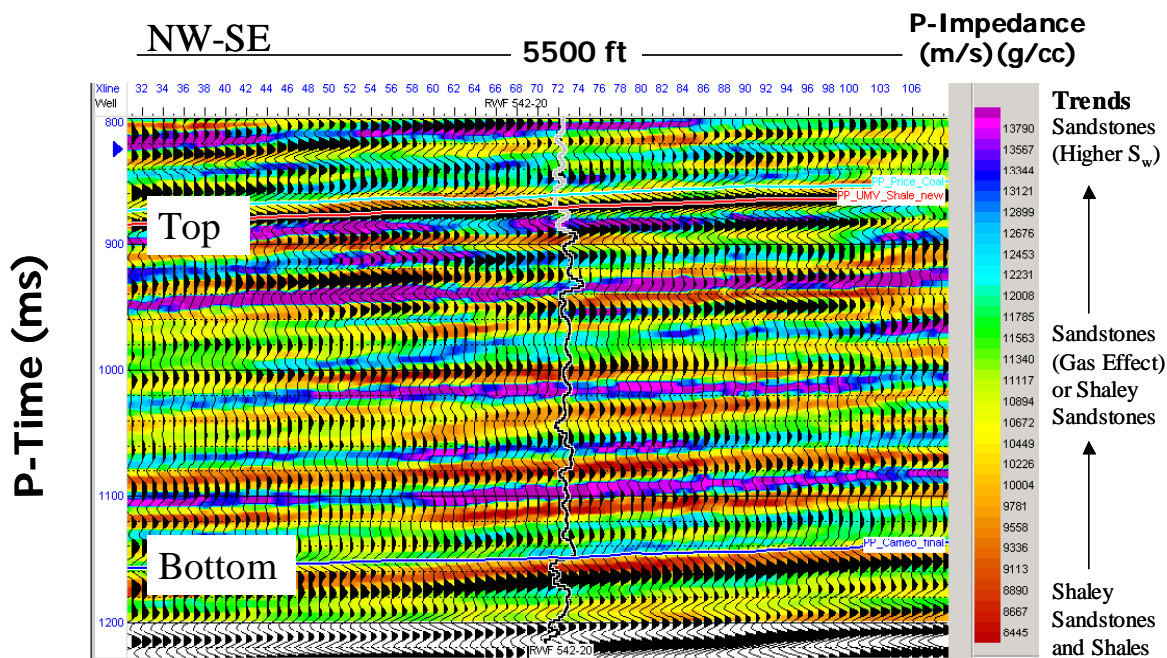


Figure 5-7 Seismic line B (in-line 85) from Rulison Field showing the P-impedance inversion from post-stack data in P-time. Note the location of the top (top of UMV shale) and bottom (top of Cameo coal) of the area of interest or reservoir. Filtered P-impedance log from well RWF 542-20 is plotted to quality control the acoustic inversion results. Figure 5-5 shows the location of the line.

Figure 5-7 shows the details obtained from model based inversion in the Williams Fork Formation. As shown in the figure, the inversion results have a higher resolution than the P-wave reflection data. They show more detail due to the incorporation of log data during the creation of the initial guess model.

Figure 5-8 shows a histogram of the P-impedance numerical values estimated from the inversion calculation. It matches the P-impedance calculated from well data.

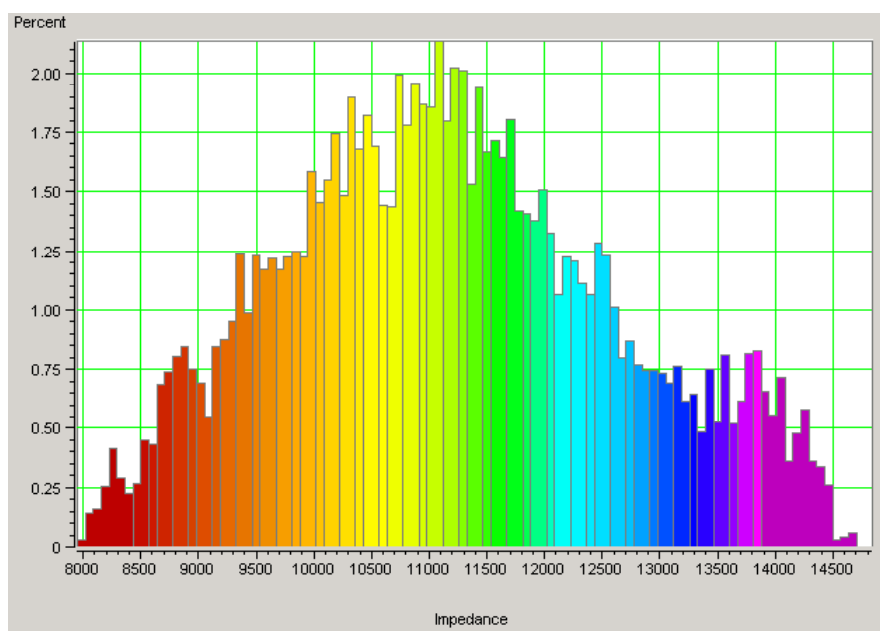


Figure 5-8 Histogram of P-impedance numerical values in the thick heterogeneous reservoir area.

Figure 5-8 suggests that most of the P-impedance numerical values obtained from the seismic inversion are in the range of 9500 to 12500 (m/s)(g/cc), which is consistent with the P-impedance values related with sandstones saturated with gas (Chapter 4). Figure 5-9 shows a crossplot between P-wave velocity log and calculated P-impedance log in the interval of interest (approximately between 4500 to 6500 ft of depth) from the crossplot a linear relation was obtained between V_p and I_p for this field (Equation 5-3).

$$V_p = 0.325I_p + 722.809 \quad (5-3)$$

where, V_p is P-wave velocity (m/s), and

I_p is P-impedance (m/s)(g/cc).

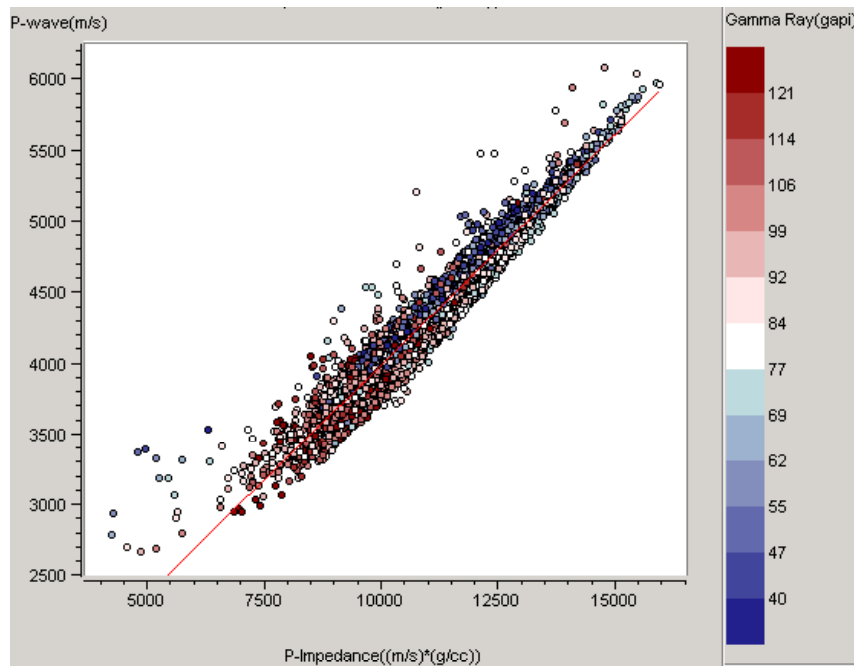


Figure 5-9 Crossplot of P-wave velocity versus P-impedance from log data colored by gamma ray measurements. The red line shows the least square best fit to the data (Equation 5-3).

Equation 5-3 was used as a transform relation to obtain P-wave velocity from P-impedance after seismic inversion. Figure 5-10 shows two time-slices at 1000 ms (P-time).

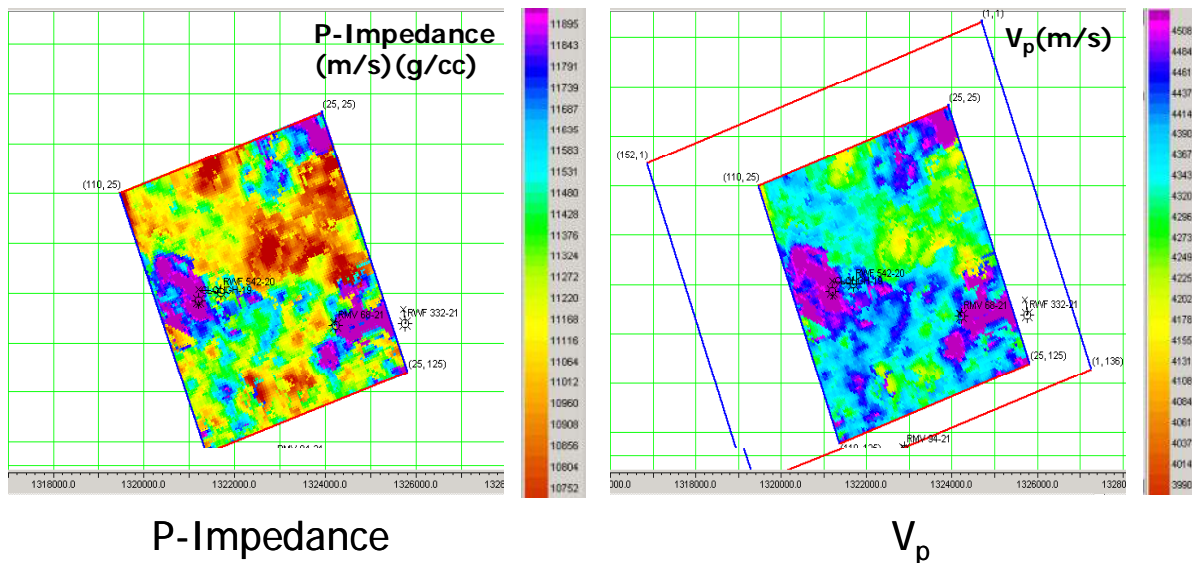


Figure 5-10 P-impedance extracted at 1000 ms in P-time and the corresponding P-wave velocity calculated using Equation 5-3. The figure on the right shows the RCP survey area and the sub-area used for the inversion.

From Figure 5-10 it is possible to observe that P-impedance range from 10700 to 11895 (m/s)(g/cc) at 1000 ms in P-time domain, and P-wave velocities range from 3990 to 4500 (m/s). Results from acoustic impedance inversion and P-wave velocity reveal possible geological features including sand bodies, sand channels and shaley sandstone areas. To reduce ambiguity when interpreting lithology and fluid properties from elastic information, S-wave information is necessary. Acoustic impedance inversion alone will not be enough to discriminate fluids and lithology.

A similar procedure was followed to invert S-wave data from RCP 2003 survey at Rulison Field. The inversion results can be interpreted using the rock physics

transforms created previously using core and log data. Future work includes combining P- and S-impedance to obtain a V_p/V_s ratio inverted volume to predict overpressure areas with gas and delineate sand bodies in the reservoir.

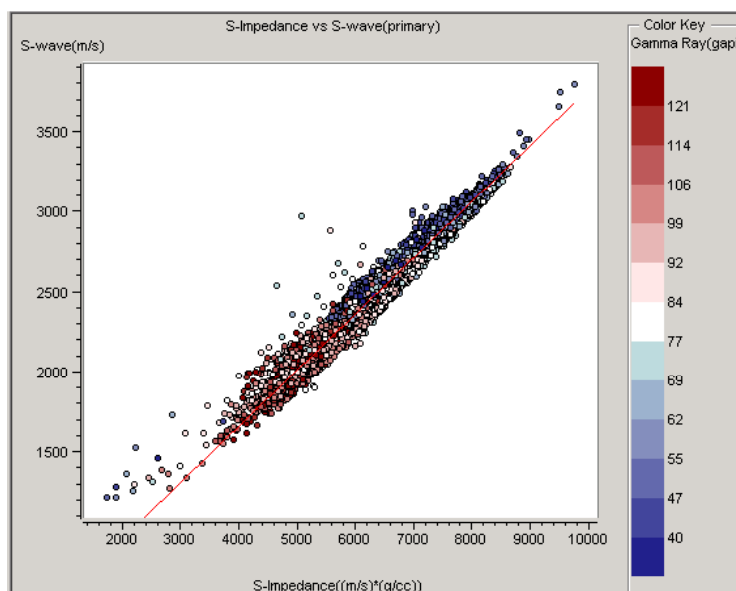


Figure 5-11 Crossplot of S-wave velocity versus S-impedance from log data colored by gamma ray measurements. The red line shows the least square best fit to the data (Equation 5-4).

Figure 5-11 shows a crossplot between S-wave velocity log and calculated S-impedance log in the area of interest (approximately between 4500 to 6500 ft of depth). from the crossplot a linear relation was obtained between V_s and I_s for this field (Equation 5-4).

$$V_s = 0.350I_s + 253.321 \quad (5-4)$$

where, V_s is S-wave velocity (m/s), and

I_s is S-impedance (m/s)(g/cc).

Inversion results can be interpreted using the relations between elastic rock properties and petrophysical and reservoir conditions studied in Chapter 3 and 4. Future work includes combining P- and S-impedance to obtain a V_p/V_s inverted volume that will help to reduce uncertainty and ambiguity in the interpretation of the results on terms of pore fluids, pressure and lithology.

5.4 Discussion of results

From laboratory and log analysis, I have shown that, combining P- and S-wave information on tight gas sandstone reservoirs, it is possible to reduce ambiguity of lithology, fluid and pore pressure effects analysis (Chapter 3 and 4). Lithology has a significant influence on V_p/V_s . Fluid effects on V_p/V_s are significant but less than lithology effects. V_p/V_s changes due to primary depletion (pore pressure decreases) are difficult to observe on unfractured tight sandstones, but with the presence of fractures changes are enhanced. V_p/V_s is also sensitive to pore pressure increases and could be used as an overpressure indicator.

Discrimination between the different effects from seismic is difficult. However, at Rulison Field, low V_p/V_s anomalies can be interpreted as a prospect indicator, since we are looking for gas-saturated sandstones preferably at overpressure conditions (undrained

areas) and we have shown that in this case, fluid, lithology and pressure conditions, all contribute to lower V_p/V_s .

From travel time analysis of multicomponent data a V_p/V_s map of the reservoir was obtained and low V_p/V_s anomalies were identified. However, there is high uncertainty in this kind of maps due to the high heterogeneity (discontinuous thin sand channels and shales) of the thick fluvial interval. Due to the lack of strong reflectors inside the interval of interest (UMV shale to the Cameo coal), there are limitations to measure V_p/V_s using travel time analysis in thin intervals inside the thick reservoir.

In this Chapter, I showed how using model based inversion on P-wave, it is possible to distinguish possible geological features including sand bodies, sand channels, shaley sandstone areas. To reduce ambiguity when interpreting lithology and fluid properties from seismic information, S-wave data are necessary. Acoustic impedance inversion alone will not be enough to discriminate fluids and lithology.

Future work includes combining P- and S-impedance to obtain a V_p/V_s inverted volume that will help to reduce uncertainty and ambiguity in the interpretation of the results on terms of pore fluids, pressure and lithology.

Chapter 6

CONCLUSIONS AND RECOMMENDATIONS FOR FUTURE RESEARCH

6.1 Conclusions

The main contribution of this research is the understanding of the rock physics of tight gas sandstones and its use in high-resolution seismic reservoir characterization. Through rock physics experiments and numerical modeling, I show the relationships between elastic rock properties and petrophysical and reservoir properties on unfractured tight gas sandstones. I have shown a procedure for using rock physics to link P-wave and S-wave properties to pore pressure, pore fluid and lithology.

The results of this research show that lithology has a significant influence on V_p/V_s of tight gas sandstones. Fluid effects on V_p/V_s are significant but less than lithology effects. V_p/V_s changes due to primary depletion (pore pressure decreases) are difficult to observe in unfractured tight gas sandstones. However, V_p/V_s is more sensitive to pore pressure increases, and therefore could be used as an overpressure indicator. This assumes an unfractured state to the rock mass.

The following results from the analysis of core and log data from Rulison Field, Colorado, can be used to interpret seismic data in tight gas sandstones:

1. V_p/V_s variation due to pore fluid changes (100% gas to 100% brine) is approximately 8%. This change is less at partially saturated conditions and is enhanced by overpressure conditions.
2. V_p/V_s variation due to lithology changes (clean sandstone to shaley sandstone) is approximately 12%.
3. V_p/V_s variation for Rulison Field tight sandstone due to pore pressure increases (hydrostatic to overpressure) is approximately 6%. V_p/V_s variation due to pore pressure decreases (primary depletion) is less than 0.5% in unfractured tight sandstone cores. However, under the presence of fractures, there is evidence that velocity changes could be enhanced (Xu et al., 2005).

The possibility of detecting pressure, lithology and fluid effects by analyzing V_p/V_s extracted from AVO analysis or multicomponent reflection data, will depend on the accuracy of the velocities obtained from seismic. I applied two methods for extracting V_p/V_s from multicomponent seismic. First, travel time seismic interpretation. There is high uncertainty when using this method in thick intervals (2000 ft) due to the high geological heterogeneity in the area and the limitations to measure V_p/V_s in thinner intervals inside the reservoir (higher resolution measurements). The second method is inversion. This method allows us to estimate elastic properties from seismic amplitudes. Interpretation of P- and S-impedances on tight gas sandstones is more definitive than interpretation of P- and S-wave amplitude alone.

Discrimination between pressure, lithology, and fluid effects from seismic is difficult. However, at Rulison Field, low V_p/V_s anomalies can be interpreted as a prospect indicator, since we are looking for gas-saturated sandstones preferably at overpressure conditions (undrained areas) and I have shown that in this case, fluid, lithology, and pressure conditions, all contribute to lower V_p/V_s .

In general, low $V_p/V_s (< 1.5)$ is related to good quality rocks (sandstones with low clay content) and gas overpressure conditions in tight gas sandstones. V_p/V_s changes due to lithology, pressure, and fluid effects are quantified using core and log data. The results could be used to identify prospect areas at Rulison Field and could be applied as well in other tight gas sandstone reservoirs.

6.2 Recommendations for future research

As mentioned before, the main contribution of this research is the understanding of the rock physics basis of tight gas sandstones, and the identification of a potential to use this for high-resolution seismic reservoir characterization. Through rock physics experiments and numerical modeling, I show the relations between elastic rock properties and petrophysical and reservoir conditions on unfractured tight gas sandstones. Through additional research, the effects of fractures on elastic properties of tight gas sandstones should be incorporated in the rock physics model (Figure 6-1). Initial understanding of the matrix properties of Rulison Field is provided in this thesis. However, different authors have shown evidence that support the presence of natural fractures in the

reservoir and the influence of them on the reservoir productivity (Jansen, 2005; Cumella and Ostby, 2003). Future research should be focus on the understanding of the effects of fractures on elastic properties of tight gas sandstones and their relation to petrophysical and reservoir properties.

The isotropic rock physics model from the ultrasonic experimental data of tight gas sandstone samples should give a reasonable estimate of the elastic properties of the reservoir matrix material. A detailed numerical modeling, using Gassmann's theory, was used to understand the effect of fluid saturation on elastic properties of the reservoir. To more accurately simulate the seismic properties of the reservoir, the effects of fractures should be included in an anisotropic rock physics model. I recommend using crack models to calculate the elastic stiffness tensor of dry fractured rock, for example, Hudson's crack model (Hudson, 1980). Brown and Korringa's equation (Brown and Korringa, 1975) can be applied to calculate the elastic stiffness tensor of the saturated fractured rock. Finally, the goal should be to develop an anisotropic, pressure-dependent model for the elastic properties of Rulison Field reservoir rock using the isotropic model developed in this thesis as the basis.

For some reservoir processes, as primary depletion, velocity sensitivity to pore pressure changes may be influenced by the presence of fractures (MacBeth et al., 2004). To quantify the effect of pore pressure on rock elastic properties, the effective stress coefficient, n , that relates effective pressure to pore pressure ($P_e = P_c - nP_p$), is necessary. In most of the cases, for simplicity, $n=1$; which means that the elastic properties are only

dependent of the differential pressure (difference between confining and pore pressure, $P_d = P_c - P_p$). In unfractured tight gas sandstones at the core scale, the effective stress coefficient for bulk modulus is between 0.3 and 0.4 (Xu et al., 2005). For shear modulus this coefficient is close to 1. Under the presence of fractures and cracks the stress coefficient for bulk modulus will be higher than for unfractured rocks, between 0.5 and 0.8; therefore, there is an increase of P-wave sensitivity to pore pressure due to fractures.

For pore pressure monitoring purposes, it is very important to understand and quantify the effective stress coefficient. Future work should be done in this area, especially for fractured tight gas sandstones. For reservoir monitoring purposes, the confining pressure is almost constant and the effective pressure will depend directly on pore pressure and on the effective stress coefficient. The larger the effective stress coefficient n , the more sensitive P- and S-wave velocities will be to pore pressure changes. For shear modulus the effective stress coefficient is close to 1, and for bulk modulus is between 0.5 and 0.8 in fractured tight gas sandstones at 20 MPa of differential pressure (Xu et al., 2005). These results suggest the potential to use shear wave data for pore pressure monitoring in tight gas sandstones. From laboratory observations there is evidence that S-waves are more sensitive to pore pressure changes than P-waves in very consolidated material as tight gas sandstones.

Other studies suggest the use of S-wave data as a direct hydrocarbon indicator in fractured media (Guest et al., 1998). Cardona (2001) shows that, under conditions of equilibrated pore pressure, fractured rocks present vertically propagating shear-waves

that may be sensitive to fluid saturation depending on the symmetry of the medium. More research should be done in this area, to exploit the potential of using shear wave data as a direct hydrocarbon indicator in fractured gas reservoirs.

In this thesis research, V_p/V_s sensitivity to fluid saturation, pore pressure, and lithology was studied and the results can be used for reservoir characterization of tight gas sandstone reservoirs. Future research should incorporate the sensitivity of V_p/V_s to fractures. For this purpose, anisotropy rock physics models have to be developed. Recent studies (Guest et al., 1998) suggest that an increase of V_p/V_s could be expected due to the effect of fracture filling fluids on shear-wave propagation, this research suggest that gas filled fractures can decrease the shear velocity while leaving the P-wave velocity largely unaffected, hence the V_p/V_s must increase. The 9C-4D seismic acquired by RCP in the Rulison Field provides an unique opportunity to test these ideas and exploit the potential of shear-wave data as a Direct Hydrocarbon Indicator.

In order to better characterize complex reservoirs, such as Rulison Field, with the use of elastic properties obtained from multicomponent seismic data, it is necessary to estimate accurate velocities from seismic data. For this purpose, it will be important to compare different inversion methods and quantify uncertainty in the estimations. Also AVO studies will provide another mechanism of estimating V_p/V_s .

Finally, V_p/V_s and S-wave time-lapse analysis combined with previous production data and a good understanding of a pressure dependent anisotropic rock physics model for tight gas sandstones, will make it possible to develop a framework for dynamically

characterizing the fractured tight gas sandstone reservoir. The understanding of elastic rock properties under effective stress, taking into account the effective stress coefficient, and the incorporation of fractures in the rock physics model is an important area of future research (Figure 6-1).

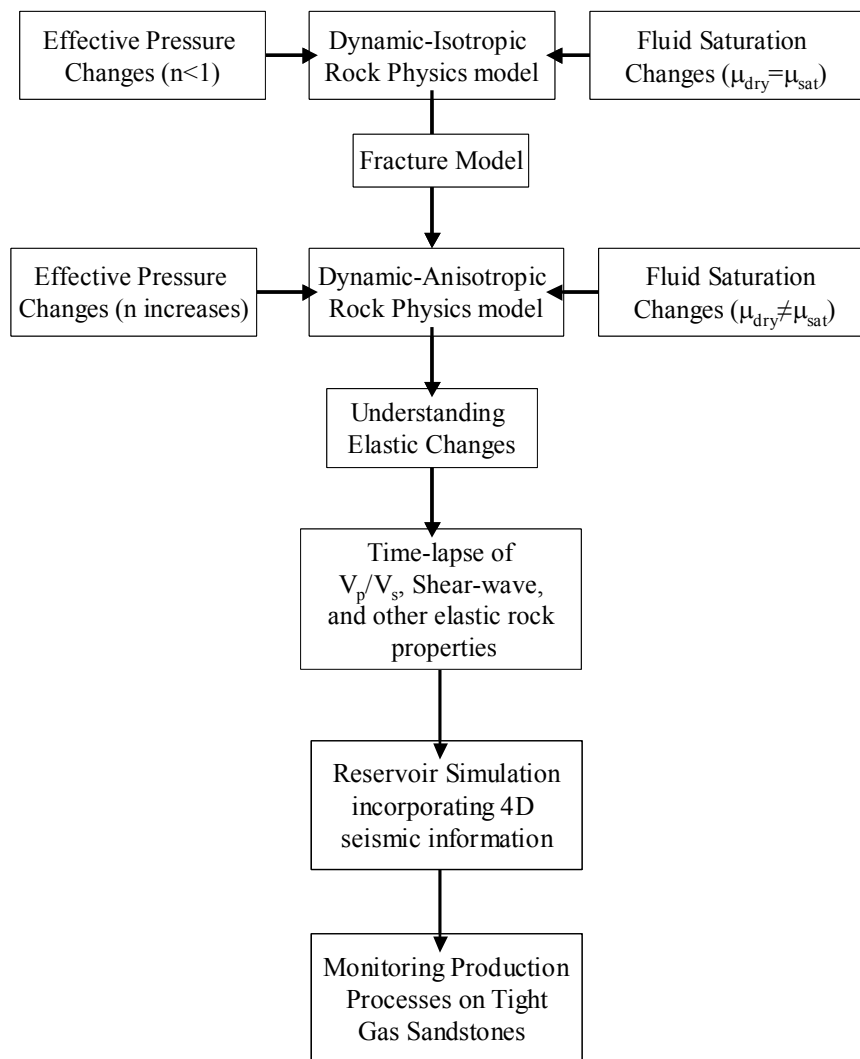


Figure 6-1 Possible future integrated workflow for dynamic-anisotropic reservoir characterization of fractured tight gas sandstones at Rulison Field.

REFERENCES

- Batzle, M., and Wang, Z., 1992, Seismic properties of pore fluids: *Geophysics*, 57, 1396-1408.
- Batzle, M., and Prasad, M., 2004, personal communication, Center for Rock Abuse, Colorado School of Mines, Golden.
- Briceño, G., 2003, Invasion profiles derived from shallow wireline logs: Colorado School of Mines, Master Thesis T-5717.
- Briceño, G., 2004, Rock & Fluid Properties II: Reservoir Characterization Project Report, Spring 2004 Sponsor Meeting, Colorado School of Mines, Golden.
- Brown, R., and Korringa, J., 1975, On the independence of the elastic properties of a porous rock on the compressibility of the pore fluid: *Geophysics* 40, 608-616.
- Camp, W., Brown, A., and Poth, L., 2003, Basin Center Gas or Subtle Conventional Traps?: RMAG/PTTC Fall Symposium-Petroleum Systems and Reservoirs of Southwest Wyoming.
- Castagna, J.P., Batzle, M.L. and Eastwood, R.L., 1985, Relationships between compressional-wave and shear-wave velocities in clastic silicate rocks: *Geophysics*, 50, 571-581.
- Cardona, R., 2001, Shear wave velocity dependence on fluid saturation: SEG Expanded Abstracts 20, p. 1712.
- Cluff R., and Cluff, S., 2004, The origin of Jonah Field: Northern Green River Basin, Wyoming: AAPG Studies in Geology, 52, 127-145.
- Connolly, P., 1998, Calibration and inversion of non-zero offset seismic: SEG 68th Annual Meeting, Expanded Abstracts, AVO 1.5, 182-184.
- Cumella, S., and Ostby, D., 2003, Geology of the Basin-Centered Gas Accumulation, Piceance Basin, Colorado: Rocky Mountain Association of Geologists, Chapter 10, 171-193.

- Eastwood, R.L., and Castagna, J.P., 1983, Basis for interpretation of V_p/V_s ratios in complex lithologies: Soc. Prof. Well Log Analysts 24th Annual Logging Symp.
- Eberhart-Phillips, D., Han, D. H, and Zoback, M.D., 1989, Empirical relationships among seismic velocity, effective pressure, porosity, and clay content in sandstone: *Geophysics*, 40, 949-954.
- Ensley, R.A., 1984, Comparison of *P*- and *S*-wave seismic data: a new method for detecting gas reservoirs: *Geophysics* 49, 1420-1431.
- Evans, L., 2005, personal communication, Williams Oil Company, Denver.
- FLAG 4. Fluid Acoustic for Geophysics, HARC and CSM.
- Gassmann, F., 1951, Elastic waves through a packing of spheres: *Geophysics*, 16, 673-685.
- Gregory, A.R., 1977, Aspects of rock physics from laboratory and log data that are important to seismic interpretation in Seismic Stratigraphy—applications to hydrocarbon exploration: *Am. Assn. Petr. Geol., Mem.* 26, 15-45.
- Guest, S., van der Kolk, C., Potters, H., 1998, The effect of fracture filling fluids on shear-wave propagation: 68th Ann. Internat. Mtg., SEG Expanded Abstracts, 948-951.
- Han, D., and Batzle, M., 2004, Gassmann's equation and fluid-saturation effects on seismic velocities: *Geophysics* 69, p.398.
- Hill, R., 1952, The elastic behavior of crystalline aggregate: *Proc. Phys. Soc. London*, 65, 349-354.
- Hofmann, R., Xu, X., Batzle, M., and Tshering T., 2005, Which stress coefficient do you mean?: SEG Expanded Abstracts, 23, p.1766.
- Hudson, J.A., 1980, Overall properties of a cracked solid: *Math. Proc. Cambridge Philos. Soc.*, 88, 371-384.
- Jansen, K., 2005, personal communication, Reservoir Characterization Project, Colorado School of Mines, Golden.

- Johnson, R.C., and Rice, D.D., 1990, Occurrence and Geochemistry of Natural Gases, Piceance Basin, Northwest Colorado: AAPG Bulletin 74, 805-829.
- Jones, F.O., and Owens, W.W., 1979, A laboratory study of low permeability gas sands: SPE 7551.
- Kithas, B.A., 1976, Lithology, gas detection and rock properties from acoustic logging systems: Soc. Prof. Well log Analysts 17th Annual Logging Symposium, R1-R10.
- Klinkenberg, L. J., 1941, The permeability of porous media to Liquids and Gases: Drilling and Production Practice, 200-213.
- Landro, M., Veire, H.H., Duffaut, K., and Najjar, N., 2003, Discrimination between pressure and fluid saturation changes from marine multicomponent time-lapse seismic data: Geophysics 68, p. 1592.
- Lorenz, J.C., Sattler, A.R., and Stein, C.L., 1989, The effects of depositional environment on petrophysical properties of the Mesaverde reservoirs, northwestern Colorado: SPE, paper 19583, Transactions 64th Annual Technical Conference, p. 119-132.
- MacBeth, C., Stammeijer J., and Omerod, M., 2004, A petroelastic-based feasibility study of monitoring pressure depletion in UKCS gas reservoir: SEG Expanded Abstracts 22, p.1426.
- Mavko, G., Mukerji, T., and Dvorkin, J. The rock physics handbook: tools for seismic analysis in porous media: Cambridge University Press, 1998.
- McCormack, M.D., Dunbar, J.A. and Sharp, W.W., 1985, A stratigraphic interpretation of shear and compressional wave seismic data for the Pennsylvanian Morrow formation of southeastern New Mexico, *in* Seismic Stratigraphy II: AAPG Memoir 39, 225-239.
- Miller, S. and Stewart, R., 1990, Effects of lithology, porosity and shaliness on P and S wave velocities from sonic logs: Canadian Journal of Exploration Geophysics, 26, 94-103.
- Minear, J.W., 1982, Clay models and acoustic velocities: 57th Ann. Tech. Conf. And Exhib., Soc. Pet. Eng. of AIME, New Orleans.
- Nelson, P., 2002, A review of the Multiwell Experiment in Tight Gas Sandstones of the Mesaverde Group, Piceance Basin, Colorado.

- Northrop, D.A., and Frohne, K.H., 1990, The Multiwell Experiment- A field laboratory in tight gas sandstone reservoirs: *J. Pet. Tech.*, 772-779.
- Pickett, G.R., 1963, Acoustic character logs and their application in formation evaluation: *J. Pet. Tech.*, 659-667.
- Prasad, M, 2003, Velocity-permeability relations within hydraulic units: *Geophysics*, 68, 108-117.
- Rafavich, F., Kendall, C.H.St.C., and Todd, T.P., 1984, The relationship between acoustic properties and the petrographic character of carbonate rocks: *Geophysics*, 49,1622-1636.
- Reinecke, K.M, Rice, D.D., and Johnson, 1991, Characteristics and development of fluvial sandstone and coalbed reservoirs of Upper Cretaceous Mesaverde Group, Grand Valley field: *RMAG Guidebook*, 209-225.
- Russell, B., 2005, Introduction to seismic inversion, oral presentation, Colorado School of Mines, Golden.
- Shanley, K.W., Cluff, R.M., and Robinson, J.W., Factors controlling prolific gas production from low-permeability sandstone reservoirs: Implications for resource assessment, prospect development, and risk analysis: *AAPG Bulletin*, 88, 1083-1121.
- Spencer, C.W., 1989, Comparison of overpressuring at the Pinedale anticline area, Wyoming, and the Multiwell experiment site, Colorado: *U.S.G.S. Bulletin* 1886, p. 16.
- Sattler, A., 1989, Core Analysis in Low Permeability Sandstone Reservoir: Results from Multiwell Experiment: Sandia National Laboratories Report SAND89-0710, UC-92a, p.58.
- Sondergeld, C., and Rai, C.S., 1986, Laboratory observations of shear-wave propagation in anisotropic media: *The Leading Edge*, 11, no. 2, 38-48.
- Tatham, R., 1982, V_p/V_s and lithology: *Geophysics*, 41, 336-344.
- Thomsen, L., 1986, Weak elastic anisotropy: *Geophysics*, 51, 1954-1966.

- Tutuncu, A., Podio, A., and Sharma, M., 1994, An experimental investigation of factors influencing compressional- and shear- wave velocities and attenuations in tight gas sandstones: *Geophysics*, 59, 77-86.
- Wang, Z., 2000, The Gassmann equation revised: comparing laboratory data with Gassmann's predictions: *Geophysics reprint series, Seismic and Acoustic Velocities of Reservoir Rocks*, vol.3.
- Wei, K.K., 1986, Effect of fluid, confining pressure, and temperature on absolute permeabilities of low permeability sandstones: *SPE formation evaluation*.
- Xu, X., Batzle, M, and Hofmann, R., 2005, Influence of pore pressure on velocity in low-porosity sandstone: implications for time-lapse feasibility and pore pressure study: to be submitted to *Geophysics*.